Measurement of the direct CP asymmetry in $B^0 \to K^{*0}\gamma$ decays with the LHCb detector

Ricardo Vázquez Gómez
Departament d'Estructura i Constituents de la Matèria
Facultat de Física, Universitat de Barcelona

Memòria presentada per optar al grau de
Doctor per la Universitat de Barcelona
12 de desembre de 2012

Directors: Dr. Ricardo Graciani Díaz i Dr. Hugo Ruiz Pérez

Programa de Doctorat de Física

A Esther y José

"El que no sabe donde va, jamás encuentra viento favorable"
Séneca

Acknowledgements

Soy plenamente consciente de que los agradecimientos es la única parte de la tesis que se va a leer íntegramente el 99 % de la gente a quien le caiga en sus manos este documento. No puedo expresar todo el agradecimiento que debo a la gente que me ha ayudado en estas cuatro líneas, pero lo voy a intentar, espero no defraudar a nadie y antes que nada, gracias por todo.

Primeramente a las personas que me han guiado más directamente en el camino de la investigación, Ricardo Graciani Díaz y Hugo Ruiz Pérez por su paciencia infinita en el momento de resolverme dudas cuando no entendía nada, por hacerme siempre nuevas preguntas y por hacer que buscara las respuestas dentro de mi cabeza. Muchas gracias también a Lluis Garrido Beltrán que fue quien me dió la oportunidad de entrar en el grupo y hacer el doctorado y a Eugeni Graugés Pous porque fue en sus clases de Física Nuclear y de Partículas donde descubrí que me quería dedicar al mundo de la *farándula particulera*. Sin ninguno de ellos cuatro nada de esto hubiese sido posible.

Quiero agradecer también a mis compañeros de grupo por todos los momentos que hemos vivido juntos y por compartir la frustración de cuando las cosas no salen, que acostumbra a ser casi siempre. A Míriam, que fue la primera que me enseñó que Gaudi y DaVinci eran algo más que un par de señores. A Carlos, porque mi mano sigue sonando como un sonajero. A Antonio, por tantas horas en Ginebra conscientes de que "*todo es un mamoneo*". A Elías, por dejarme conducir su bicicleta. A Jordi, que siempre tiene la respuesta correcta. A Albert, que ve matrix, y buena parte de este trabajo ha sido posible también gracias a él. A Marc, por hacerme ver lo importante que son las llaves. A Alessandro, por ser siempre generoso mostrándome las cosas buenas de su tierra. A Cédric, por tantas discusiones esclarecedoras. A Vicente, que siempre tiene una pregunta que hacer. No me olvido de Edu, Xavi y Daniel que me ayudaron a pasar mucho mejor las noches de *commissioning* y de Meyrinoise. De Adrià, cuyo post-it me

llevaré donde quiera que vaya. De David, Albert C., Carlos A. y Álvaro que siempre me imagino con un casco blanco.

No me puedo olvidar de mis compañeros del "despacho con vistas al mar", Marta, David, Ana y Carla, que también han sufrido los veranos cálidos y los inviernos helados del despacho de la planta 5, afortunadamente ya todos (o casi) están en un lugar mejor, o sea, un despacho con ventana. Tampoco me olvido de todos mis amigos y compañeros de la carrera, doctorado y BIT, Lluc, David, Carla, Guillem, Joan(s), Octavi, Jordi, Jaume(s), Fran, Miquel, Joana, Jose Maria, Diego, Roger, Eloi, Carlos, Miguel, Carles y muchos más que no están en esta lista porque sinó sería demasiado larga.

Como no podría ser de otra manera, también quiero agradecer a Nathalie y Francesco, que me soportan todos los días y me han hecho apreciar mucho más la pasta. Son los mejores compañeros de piso que uno pueda desear.

During all these years, I have spent a large amount of time at CERN, where I have had the opportunity to work with astonishing people and excellent professionals. I would like to particularly mention Gaia Lanfranchi, José Ángel Hernando and Frederic Teubert who were the first people I collaborate with at CERN, and showed me all I know about muons; Pascal Perret, Marie-Noëlle Minard and Stéphane Monteil for guiding me in the world of calorimetry; and last but not least Olivier Deschamps, who has had the patience of letting me collaborate with him and has played a fundamental role in the work that I'm presenting here.

Además mientras estuve en Ginebra he tenido la suerte y el placer de conocer a gente que ha sido mi familia mientras pasábamos el típico frío suizo. Rebeca, que es una gran amiga y mejor persona; María C., que me hace sentir orgulloso de ser su amigo; Clara, que es la persona que más me ha dado la *turra*, pero estoy contento de que así sea; Alex, Lola, Pablo, Christian, Jorge, Paloma, Lara, Carmen, Marcos, Jordi, Javi y Luca que son los mejores copinos que conozco y me habéis hecho pasar muy buenos ratos dentro y fuera del R1. Quiero tener un recuerdo especial para María Moreno, con quien he compartido una parte de mi vida en Ginebra, el éxito de este trabajo es también gracias a ti.

He dejado a las personas más cercanas para el final pero no por ello son menos importantes. Quiero agradecer el apoyo de mi famil-

ia, abuelos, tios y primas, ed anche alla mia famiglia in Italia per tutto il suo sostegno. De una forma muy especial quiero agradecer a mis padres Esther y José, a quien esta tesis está dedicada, por su apoyo incondicional en todas las decisiones que he tomado en mi vida que me han llevado a ser como soy y, al cabo de los años, a realizar este trabajo y poder escribirlo en este documento. Finalmente, a Arianna, que es una peregrina como yo y que ha estado siempre a mi lado demostrándome su amor, ofreciéndome su sonrisa y dándome sus palabras siempre que las he necesitado. Senza di te non sarebbe stato possibile, grazie, ti amo.

Table of contents

Resum

El Model Estàndar (ME) és la teoria que descriu el comportament de les partícules fonamentals i les seves interaccions, fonamentada sobre el principi d'invariància *gauge* local dels grups

$$\mathrm{SU}(3)_C \times \mathrm{SU}(2)_L \times \mathrm{U}(1)_Y \,, \tag{1}$$

on C i Y representen les càrregues de color i la hipercàrrega, respectivament, mentre que L fa referència als fermions amb quiralitat esquerra. Els grups $\mathrm{SU}(3)_C \times \mathrm{SU}(2)_L \times \mathrm{U}(1)_Y$ estan trencats espontàniament a $\mathrm{SU}(3)_C \times \mathrm{U}(1)_Q$, on Q representa la càrrega elèctrica.

En aquest model, les partícules que formen la matèria estan representades per tres generacions de fermions, dividits en quarks i leptons (l'antimatèria està formada pels corresponents antiquarks i antileptons), mentre que les forces estan representades per bosons. Tots els fermions poden interaccionar feblement i electromagnètica, però només els quarks ho fan fortament.

La física que descriu els mesons B, formats per una parella quark-antiquark amb un d'ells essent un quark de tipus b, s'analitza fent servir *l'Hamiltonià efectiu de baixes energies*. Aquest Hamiltonià està basat en el concepte d'*Operator Product Expansion* (OPE), que permet separar les contribucions de *grans distàncies* de les de *petites distàncies*. Així l'element de transició $\mathcal{H}_{\mathrm{eff}}$ que connecta els estats inicials $|i\rangle$ amb l'estat final $|f\rangle$, es pot escriure com

$$\langle f|\mathcal{H}_{\mathrm{eff}}|i\rangle \propto \sum_k C_k(\mu)\langle f|Q_k(\mu)|i\rangle \,, \tag{2}$$

on μ és l'escala de renormalització de la teoria, $Q_k(\mu)$ els operadors locals que formen una base complerta (grans distàncies), i $C_k(\mu)$ els coeficients de Wilson (petites distàncies).

Oscil·lacions de mesons neutres

Si considerem una parella de mesons B que siguin estats propis de sabor $|B^0\rangle$ i $|\overline{B}^0\rangle$, sempre podem construir una combinació linial arbitrària com

$a|B^0\rangle + b|\overline{B}^0\rangle$ que evoluciona amb el temps seguint l'equació de Schrödinger

$$i\frac{d}{dt}\begin{pmatrix}a\\b\end{pmatrix} = \mathcal{H}\begin{pmatrix}a\\b\end{pmatrix} \equiv \left(M - \frac{i}{2}\Gamma\right)\begin{pmatrix}a\\b\end{pmatrix}, \tag{3}$$

on M i Γ són matrius hermítiques 2×2. Els estats propis de la matriu $\mathcal{H}$ són $|B_L\rangle$ i $|B_H\rangle$, amb valors propis $M_1 - \frac{i}{2}\Gamma_1$ i $M_2 - \frac{i}{2}\Gamma_2$, respectivament. L'evolució temporal dels estats propis de l'hamiltonià es pot escriure com

$$\begin{aligned}|B_L(t)\rangle &= e^{-i(M_1 - \frac{i}{2}\Gamma_1)t}|B_L\rangle \\ |B_H(t)\rangle &= e^{-i(M_2 - \frac{i}{2}\Gamma_2)t}|B_H\rangle\,.\end{aligned} \tag{4}$$

Els estats propis de l'hamiltonià es poden escriure en termes dels estats propis de sabor com

$$\begin{aligned}|B_L\rangle &= p|B^0\rangle + q|\overline{B}^0\rangle \\ |B_H\rangle &= p|B^0\rangle - q|\overline{B}^0\rangle\,,\end{aligned} \tag{5}$$

on p i q es poden escollir de tal manera que satisfacin la relació $|p^2| + |q^2| = 1$. Així, l'evolució temporal dels estats de sabor es pot escriure com

$$\begin{aligned}|B^0(t)\rangle &= f_+(t)|B^0\rangle + \frac{q}{p}f_-(t)|\overline{B}^0\rangle \\ |\overline{B}^0(t)\rangle &= \frac{p}{q}f_-(t)|B^0\rangle + f_+(t)|\overline{B}^0\rangle\,,\end{aligned} \tag{6}$$

on $f_\pm(t) = \left(e^{-i(M_1 - i\frac{\Gamma_1}{2})t} \pm e^{-i(M_2 - i\frac{\Gamma_2}{2})t}\right)$, i per tant, l'amplitud de desintegració depenent del temps dels estats $|B^0\rangle$ i $|\overline{B}^0\rangle$ al mateix estat final $\langle f|$, ve donada per

$$\begin{aligned}\Gamma_f(t) = |\langle f|\mathcal{H}|B^0(t)\rangle|^2 = |A_f|^2 \Bigg[|f_+(t)|^2 + \left(\frac{q\overline{A_f}}{pA_f}\right)^2 |f_-(t)|^2 + \\ +2\mathcal{R}e\left(f_+^*(t)f_-(t)\frac{q}{p}\frac{\overline{A_f}}{A_f}\right)\Bigg]\end{aligned} \tag{7}$$

$$\begin{aligned}\overline{\Gamma}_f(t) = |\langle f|\mathcal{H}|\overline{B}^0(t)\rangle|^2 = |A_f|^2 \Bigg[\left|\frac{\overline{A_f}}{A_f}\right|^2 |f_+(t)|^2 + \left(\frac{p}{q}\right)^2 |f_-(t)|^2 + \\ +2\left(\frac{p}{q}\right)^2 \mathcal{R}e\left(f_+^*(t)f_-(t)\frac{q}{p}\frac{\overline{A_f^*}}{A_f}\right)\Bigg]\,,\end{aligned} \tag{8}$$

on $A_f = \langle f|\mathcal{H}|B^0(t)\rangle$ i $\overline{A_f} = \langle f|\mathcal{H}|\overline{B}^0(t)\rangle$ són les amplituds de desintegració instantànies.

Violació de *CP*

Segons el que s'ha vist, qualsevol diferència entre $\Gamma_f(t)$ i $\overline{\Gamma}_f(t)$, dóna lloc a violació de *CP*. Hi ha tres mecanismes possibles de violació de *CP*

En la desintegració Apareix en el moment en que el ritme de desintegració d'una partícula (B) a un estat final és diferent del de la seva antipartícula *CP* conjugada. És l'única font de violació de *CP* possible pels mesons carregats i es pot mesurar com

$$\frac{\Gamma(B \to f) - \Gamma(\overline{B} \to \overline{f})}{\Gamma(B \to f) + \Gamma(\overline{B} \to \overline{f})} = \frac{1 - \left|\frac{\overline{A_{\overline{f}}}}{A_f}\right|^2}{1 + \left|\frac{\overline{A_{\overline{f}}}}{A_f}\right|^2}. \tag{9}$$

En l'oscil·lació Es dóna quan els estats propis de l'hamiltonià no són estats propis de *CP*. Es pot mesurar en desintegracions semileptòniques com

$$A_{sl} = \frac{\Gamma\left(\overline{B} \to l^- \nu X\right) - \Gamma\left(B \to l^+ \nu X\right)}{\Gamma\left(\overline{B} \to l^- \nu X\right) + \Gamma\left(B \to l^+ \nu X\right)} = \frac{1 - \left|\frac{q}{p}\right|^4}{1 + \left|\frac{q}{p}\right|^4}. \tag{10}$$

En la interferència entre la desintegració i l'oscil·lació Té lloc en desintegracions a estats finals propis de *CP* i que són accessibles pels dos estats B i $\overline{B}$. Es pot mesurar amb l'asimetria depenent del temps

$$A(t) = \frac{\Gamma_f - \overline{\Gamma}_f}{\Gamma_f + \overline{\Gamma}_f} \tag{11}$$

Violació de *CP* al ME

Al ME, la violació de *CP* està descrita per la matriu unitària 3×3 de Cabibbo-Kobayashi-Maskawa, que descriu la rotació entre els estats de massa i els estats de sabor. La unitarietat de la matriu implica que només fan falta quatre paràmetres independents per descriure-la, tres angles i una fase complexa, que és l'únic paràmetre del ME que introdueix violació de *CP*. Les condicions d'unitarietat imposen sis condicions d'ortogonalitat entre qualsevol parella de files o columnes, que es poden representar al pla complex com un triangle. Un d'ells és conegut com a triangle unitari i les mesures actuals dels costats i angles es mostren a la Fig. 1.

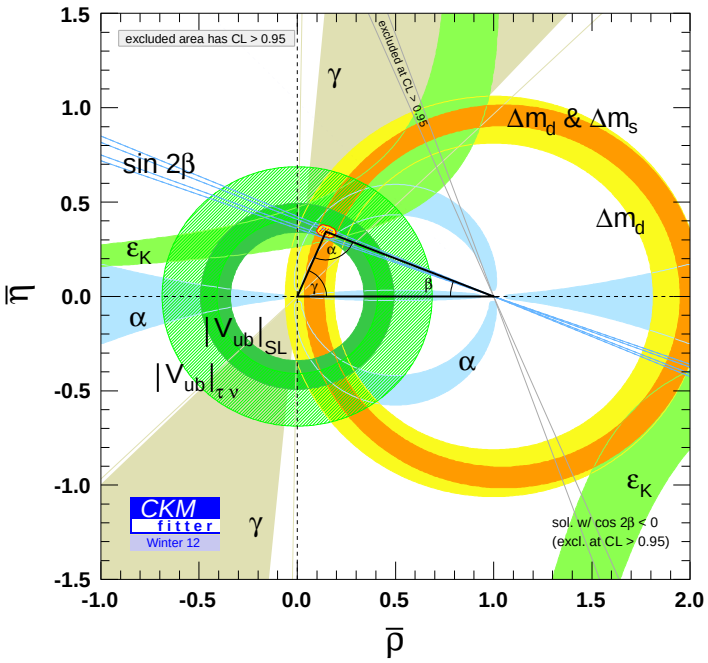

Figura 1 – Representació de les mesures actuals del triangle unitari (db).

El ME prediu violacions de *CP* inexistents o molt petites en moltes transicions, però algún tipus específic de transicions, per exemple $b \to s\gamma$ poden presentar una asimetria de *CP* de $\mathcal{O}(1\%)$.

L'experiment LHCb

L'experiment LHCb és un espectròmetre de braç únic especialment disenyat per l'estudi de la violació de *CP* i per estudiar desintegracions poc freqüents de partícules que contenen un quark b o c. Està situat al punt 8 del col·lidor LHC a Ginebra, on es produeixen col·lisions de protons a energies al centre de masses que poden arribar fins a $\sqrt{s} = 14\,\text{TeV}$.

Com mostra la Fig. 2, el detector cobreix la zona d'alta pseudorapiditat $2.0 < \eta < 5.0$, ja que la majoria de les parelles de quarks $b\bar{b}$ que es produeixen en cada col·lisió surten en direccions molt properes als feixos de protons inicials.

El detector està format per un conjunt de subdetectors que es descriuen a continuació.

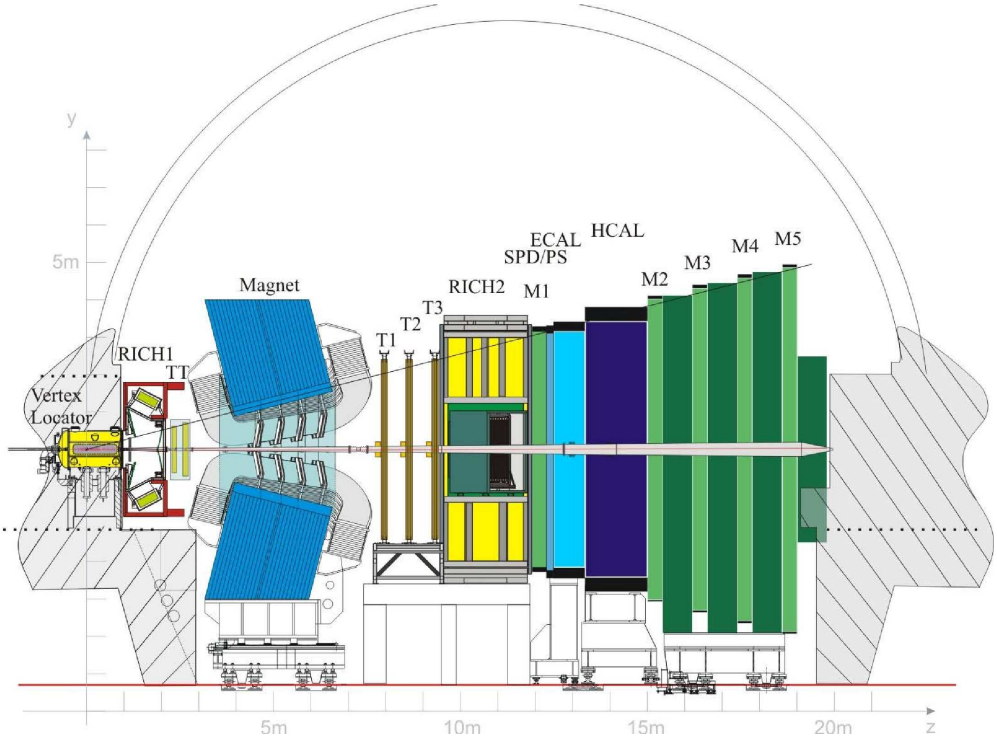

Figura 2 – Vista lateral del detector LHCb.

Vertex Locator (VELO) És el detector més proper al punt on s'origina les col·lisió i té com a objectiu distingir entre els vèrtexs formats per les col·lisions primàries (PV), producte del xoc de dos protons, dels vèrtex formats per la desintegració dels mesons B (SV).

Cambres de traces Estan formades per tres subdetectors: Tracker Turicensis (TT), Inner Tracker (IT) i Outer Tracker (OT). El primer està situat abans de l'imant dipolar de 4 Tm, mentre que les darreres estan situades després. El seu objectiu és el de mesurar el moment de les partícules que es produeixen a les col·lisions.

Detector d'imatge d'anells Cherenkov (RICH) Són dos detectors, RICH1 i RICH2, que s'encarreguen d'indentificar el tipus de partícula gràcies a la combinació de la mesura de la velocitat de les partícules, mitjançant la llum Cherenkov que emeten en atravessar els RICH, amb la mesura del moment realitzada per les cambres de traces.

Calorímetre Està compost per quatre subdetectors. El Scintillator Pad Detector (SPD), el Pre-Shower (PS), el calorímetre electromagnètic (ECAL) i el calorímetre hadrònic (HCAL). Fent servir la seva informació es poden indentificar els objectes electromagnètics (γ, π^0, electrons). També es fa servir al sistema de *trigger*, per a sel·leccionar esdeveniments on hi han partícules de gran moment tranvers (p_T) o per vetar esdeveniments massa complicats gràcies a la multiplicitat de l'SPD.

Cambres de muons És el subdetector més allunyat del punt d'interacció i identifica els muons. Està format per cinc cambres, la primera abans del calorímetre (M1) i les altres quatre després (M2-M5). La cambra M1 ajuda a millorar la mesura de p_T dels candidats de muons al trigger.

El sistema de trigger d'LHCb és l'encarregat de reduïr el nombre de dades que s'enregistraran pel seu posterior anàlisi. Està dividit en dues etapes, la primera (L0) està basada en l'electrònica del detector i analitza la informació de cada esdeveniment de manera parcial. Aquesta etapa redueix el ritme de les col·lisions que s'analitzaran de $\sim$10 MHz fins a $\sim$1.1 MHz. La segona (HLT) està basada en algorismes que reconstrueixen completament els esdeveniments i proporciona una sortida final de dades per analitzar d'uns 3 kHz.

Altres dos sistemes fonamentals per al bon funcionament del detector i per a garantir la qualitat de les dades són el sistema online i sistema offline. El primer s'encarrega de la transferència de les dades entre el detector fins al seu emmagatzematge permanent, mentre que el segon s'encarrega de la replicació de les dades que surten del detector i de la seva reconstrucció.

Durant l'any 2011 s'ha mesurat la resolució en la mesura del moment de les partícules i s'ha trobat que es situa en el rang $\delta p/p = 0.4 - 0.6\%$ per a traces amb p_T al rang $p_T \sim 5 - 100$ GeV. Això es tradueix en una resolució de la massa dels mesons B d'uns ~ 22 MeV, fonamental per a la bona separació entre B^0 i B_s^0.

La qualitat dels vèrtexs reconstruits al VELO es pot veure en la Fig. 3, on es representa la resolució en el paràmetre d'impacte (IP) de les dades reals, comparada amb dades simulades.

La correcta identificació de les partícules és també essencial per a l'estudi de desintegracions de mesons B o D. L'eficiència promig en la identificació de kaons és $\epsilon(K \to K) = 95\%$ amb només $\epsilon(\pi \to K) = 5\%$ de mala identificació amb pions. Pels electrons, l'eficiència d'identificació és del 93% amb una mala identificació de pions de l'1%. Pel que fa als fotons i π^0, quan aquests últims tenen una energia transversa (E_T) superior a ~ 2 GeV, els dos fotons

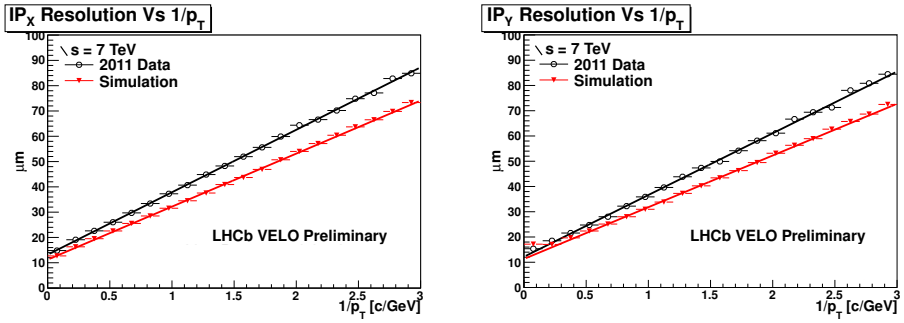

Figura 3 – Resolució en el paràmetre d'impacte (IP) en la coordenada x (esquerra) i en la coordenada y (dreta) en funció de $1/p_T$. La línia negra representa les dades de 2011 i la vermella són dades simulades. Només es consideren esdeveniments amb una sola interacció primària.

de la desintegració aparèixen com a un únic dipòsit d'energia al calorímetre. Fent servir la forma d'aquest dipòsit d'energia, es pot distingir entre γ/π^0 mantenint una eficiència del 90% en la sel·lecció dels fotons i eliminant el 60% d'aquests tipus de π^0. Pels muons, la seva eficiència d'identificació és del 98% quan tenen $p_T > 10\,\text{GeV}$, amb una contaminació de pions de $\epsilon(\pi \to \mu) < 0.6\%$.

Calibració del subdetector SPD

L'SPD, és un detector format per cel·les de plàstic escintil·lant de 1.5 cm de gruix. En total hi han 6016 cel·les dividides en tres regions amb relacions d'àrea inner:middle:outer, 1:2.25:9, per acomodar la major densitat de partícules a prop del feix. Quan una partícula carregada travessa una d'aquestes cel·les, diposita una energia segons la distribució de Landau

$$\psi(\lambda) = \frac{1}{2i\pi}\int_{c-i\infty}^{c+i\infty} e^{(s\log s+\lambda s)}ds\,, \tag{12}$$

on c és qualsevol nombre positiu i $\lambda = (E - E_{\text{MIP}})/\Delta$, essent E_{MIP} el valor més probable d'energia dipositada i Δ un paràmetre que depèn del tipus de material atravessat. Pel cas de l'SPD, $\Delta = 0.13\,\text{MeV}$.

Els fotons emessos pel procés d'escintil·lació són transportats fins a un fotomultiplicador per una combinació de fibres òptiques i fibres clares. Una vegada al fotomultiplicador, per l'efecte fotoelèctric s'allibera una quantitat

d'electrons (k) del fotocàtode que segueix una distribució de Poisson

$$f(k, N_{\text{phe}}) = \frac{N_{\text{phe}}^k e^{-N_{\text{phe}}}}{k!}\,, \tag{13}$$

on N_{phe} representa el nombre promig de fotoelectrons al fotocàtode per cada cel·la. Així, la probabilitat de que una partícula dipositi una certa energia vindrà donada per la convolució de les dues distribucions anteriors. Pel cas de l'SPD, s'ha obtingut de les simulacions, que aquesta energia promig és de 2.85 MeV.

A l'electrònica de l'SPD s'integra el senyal provinent de cada fotomultiplicador durant la finestra de 25 ns definida pel ritme de les col·lisions de l'LHC i es realitza una discriminació binària amb una tensió llindar col·locada a $0.5\,E_{\text{MIP}}$. Aquesta tensió llindar vindrà corretgida per una constant de calibració extreta de les dades.

L'eficiència de detecció de partícules és la integral de la convolució de la distribució de Landau amb la distribució de Poisson, entre una certa energia i infinit. Aquesta eficiència és funció del valor de la tensió llindar. Degut a que el detector té una resposta binària, per calibrar-lo es necessita fer un escombrat pels diferents valors de la tensió llindar. El procés de calibració consisteix en mesurar l'eficiència de cada cel·la del detector per a diferents valors de la tensió llindar, i ajustar aquests valors a la distribució d'eficiència teòrica.

Tots els components del detector es van precalibrar en bancs de proves, abans de la seva col·locació definitiva a la caverna d'LHCb. Els valors de la tensió llindar sempre es donen respecte a l'energia de la precalibració $E_{\text{MIP}}^{\text{pre}}$.

La primera calibració amb dades, es va realitzar amb rajos còsmics, abans de la posada en marxa de l'LHC. Degut a la manca de dades, no es va poder realitzar una calibració cel·la a cel·la sinó que es va fer pels grups de 64 o 32 cel·les que comparteixen el mateix tub fotomultiplicador.

Calibració amb rajos còsmics

Fent servir rajos còsmics, es van prendre dades a quatre valors diferents de la tensió llindar, però degut a les poques dades preses en cada punt, es va optar per realitzar una calibració amb un únic punt, corresponent a una tensió llindar de $1E_{\text{MIP}}$. El valor de l'eficiència presa es va comparar amb el valor de l'eficiència teòrica.

Una part fonamental del procés de calibració és la selecció correcta de les dades emprades per a poder calcular l'eficiència. Per això, una sèrie de requeriments s'han fet servir. Primerament, s'han reconstruït les traces dels

rajos còsmics fent servir només informació dels calorímetres, ja que l'excesiu angle necessari per a que poguèssin atravesar les cambres de traces i els calorímetres, redueix significativament l'estadística disponible. Els requeriments fets a les traces són

- Material atravessat per les partícules a l'SPD $< 18\,\mathrm{mm}$.
- Temps d'arribada dels muons còsmics a prop del començament de la finestra d'integració del senyal.
- Presència de només una única cel·la amb senyal a l'SPD.
- Incertesa en l'extrapolació de la traça al pla de l'SPD i al del PS $< 150\,\mathrm{mm}$.
- Confirmació del senyal al detector PS.
- Extrapolació dintre de la cel·la de l'SPD i del PS amb més de $3\,\sigma$, on σ és la incertesa en l'extrapolació.

Tots aquests criteris fan que el tamany de la mostra s'hagi reduït en un 97% respecte al tamany inicial. La constant de calibració obtinguda difereix, en promig, en un 15% respecte de la precalibració feta als bancs de proves. La constant de calibració extreta amb rajos còsmics es representa a la Fig. 4.

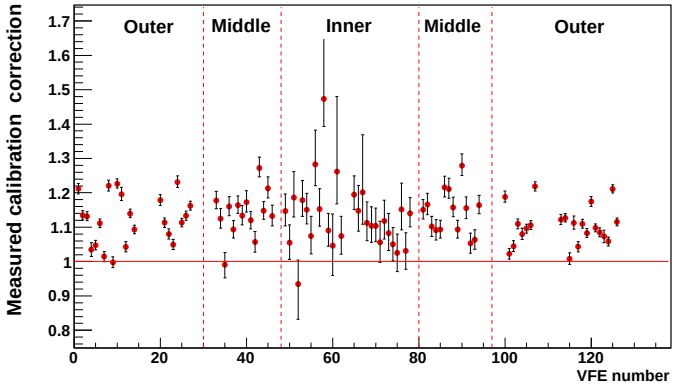

Figura 4 – Constant de calibració pels VFE de les diferents zones del detector obtinguda amb dades de rajos còsmics. La línia horitzontal es correspon amb una precalibració perfecta.

Calibració amb col·lisions *pp* a $\sqrt{s} = 7\,\text{TeV}$

Al mes de març de 2010, es van produïr les primeres col·lisions *pp* a una energia de $\sqrt{s} = 7\,\text{TeV}$. Per a la calibració de l'SPD es van agafar dades a sis valors diferents de la tensió llindar: 0.3, 0.5, 0.8, 1.0, 1.4 i $1.8\,E^{\text{pre}}_{\text{MIP}}$. Per un 3% de les cel·les, es van prendre dades a un seté punt a $2.1\,E^{\text{pre}}_{\text{MIP}}$, per a completar la seva corba de calibració. En aquest cas, la reconstrucció estàndar de traces d'LHCb es va fer servir, considerant només traces del tipus *T-tracks*, que contenen únicament segments de l'OT o l'IT, depenent de la regió on es trobin.

La sel·lecció de traces té en compte la qualitat de la traça a través del χ^2 de l'ajust, la incertesa en l'error de l'extrapolació, el nombre de punts que s'han fet servir per a reconstruïr la traça, el material atravessat per les partícules a l'SPD i la confirmació de la senyal al PS. A més, les extrapolacions de les traces al pla de l'SPD i del PS han d'estar dintre de la cel·la amb més de $3\,\sigma$, amb σ definida com a l'error en l'extrapolació. L'àrea efectiva de la cel·la, també es redueix en 8 mm per cada vora, per evitar problemes de mala alineació entre les cambres de traces i l'SPD. Un altre requeriment és que l'energia dipositada per les partícules al PS estigui dintre el rang $[1.5 - 4.0]\,\text{MeV}$.

Amb aquests criteris de selecció de les traces, s'obtè un valor de l'eficiència per a cada cel·la i per a cada valor de la tensió llindar. La Fig. 5 mostra la corba de calibració per a tres tipus de cel·les diferents, la de menor constant de calibració, la de major constant de calibració i una cel·la tipus.

La distribució de tots els factors correctius i la seva incertesa es poden veure a la figura Fig. 6, on s'aprecia que els valors promitjos de les correccions són 0.87, 0.77 i 0.81 per l'inner, middle i outer, respectivament.

La distribució de l'eficiència de cada cel·la es presenta a la Fig. 7, on es veu que en promig l'eficiència és superior al 95% una vegada que les constants de calibració s'han aplicat. La variació de l'eficiència de les cel·les de l'SPD durant l'any 2011 s'ha monitoritzat i s'ha trobat un descens promig en l'eficiència de $\sim 0.3\%$.

Alineament de l'SPD

L'alineament de l'SPD respecte de les cambres de traces, s'ha estudiat per primera vegada amb dades de col·lisions *pp*, mitjançant el perfil de l'eficiència de la cel·la, en funció de la posició on es troba l'extrapolació de la traça al pla de l'SPD. Exemples d'aquest perfil es poden veure a la Fig. 8.

La posició real, s'extreu com el promig de la posició pesada per l'eficiència. Les diferències de les posicions nominals amb les posicions extretes

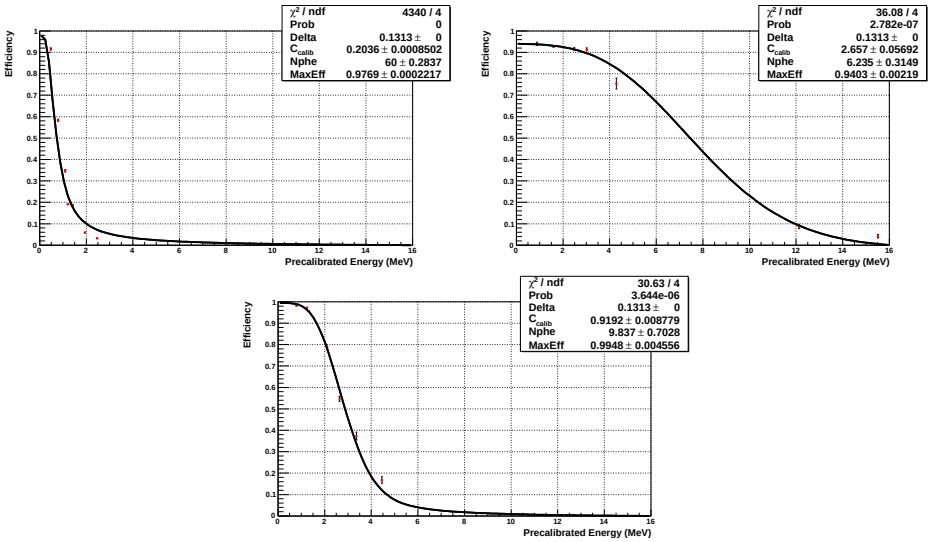

Figura 5 – Ajust per a la cel·la amb la constant de calibració més petita (adalt a l'esquerra), per a la cel·la amb la constant de calibració més gran (adalt a la dreta) i per a una cel·la tipus (a sota).

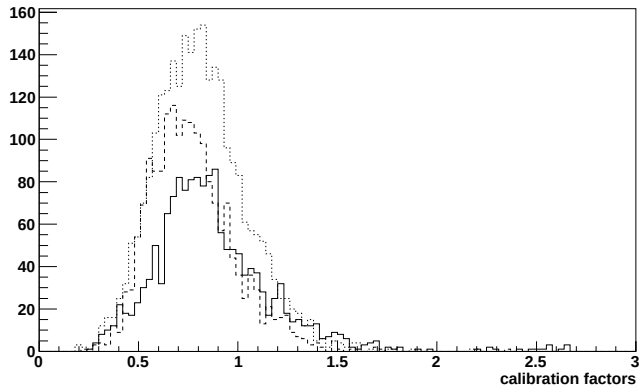

Figura 6 – Distribució de les costants de calibració que s'han d'aplicar a cada cel·la, obtingudes de la calibració amb dades de col·lisions *pp* al 2010, per la regió inner (sòlid), middle (guions) i outer (puntejat). Els valors promitjos són 0.87, 0.77 i 0.81 respectivament.

mitjançant aquest procediment es poden veure a la Fig. 9.

Dels dos gràfics es pot concloure que el detector està desplaçat verticalment, en promig, uns 10 mm, mentre que horitzontalment s'aprecia una

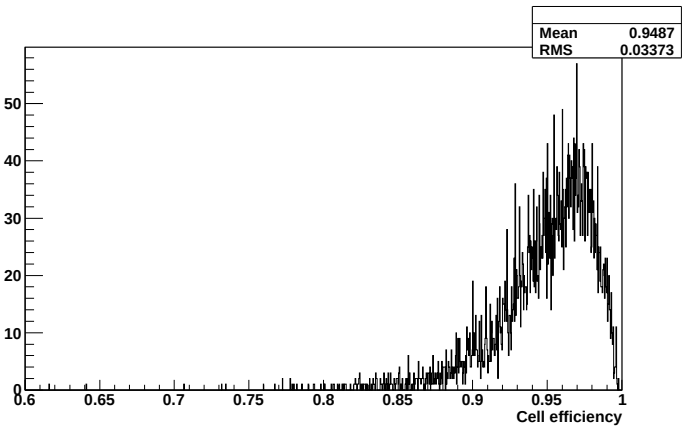

Figura 7 – Distribució de les eficiències per a cada cel·la amb dades de 2011.

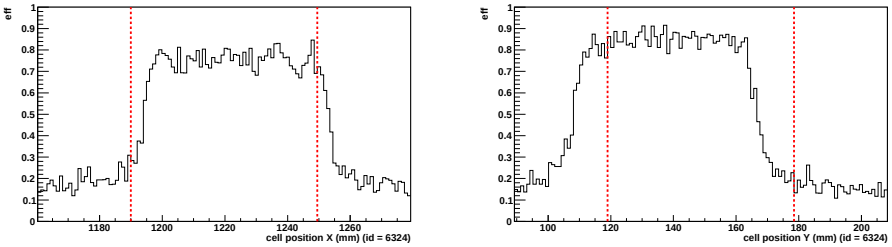

Figura 8 – Eficiència en funció de la posició de l'extrapolació de la traça al pla de l'SPD, per a una cel·la tipus per a la coordenada x (esquerra) i y (dreta). Les línies verticals indiquen la posició nominal de la cel·la.

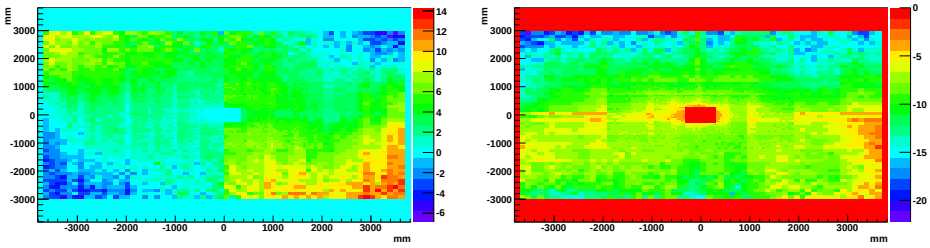

Figura 9 – Desplaçament per cada cel·la respecte a la posició nominal per les coordenades x (esquerra) i y (dreta).

rotació horària al costat C (esquerra) i antihorària al costat A (dret).

Mesura de l'asimetria directa de *CP* al canal $B^0 \to K^{*0}\gamma$

L'asimetria directa de *CP* està definida en funció dels ritmes de desintegració dels mesons B^0 i $\overline{B}^0$ com

$$A_{CP} = \frac{\Gamma(\overline{B}^0 \to \overline{f}) - \Gamma(B^0 \to f)}{\Gamma(\overline{B}^0 \to \overline{f}) + \Gamma(B^0 \to f)} \,. \tag{14}$$

Des del punt de vista teòric, aquests càlculs presenten menys incertesa provinent dels factors de forma hadrònics, ja que cancel·len al quocient. La predicció del ME és $A_{CP}^{\mathrm{ME}}(B^0 \to K^{*0}\gamma) = (-0.61 \pm 0.43)\%$, però models més enllà del ME prediuen increments significatius d'aquest valor. Experimentalment, la millor mesura d'aquesta quantitat prové de l'experiment BaBar, amb un resultat de $A_{CP}^{\mathrm{BaBar}}(B^0 \to K^{*0}\gamma) = (-1.6 \pm 2.2 \pm 0.7)\%$.

La selecció de candidats de desintegració $B^0 \to K^{*0}\gamma$ s'ha fet optimitzant la significància estadística $S/\sqrt{S+B}$ de cada requeriment, on S i B són el nombre de candidats de senyal i de soroll respectivament. Els requeriments i el seu valor es troben resumits a la Taula 1.

Una vegada seleccionats els candidats, es reconstrueix la seva massa invariant. Els mesons K^{*0} es reconstrueixen fent servir una distribució de Breit-Wigner relativista en ona P. Els paràmetres obtinguts de les dades, coincideixen amb els paràmetres que s'obtenen de l'ajust de dades simulades. La massa invariant dels mesons B^0 reconstruïts s'ha parametritzat amb dues distribucions Crystal Ball, una amb la cua radiativa cap a masses baixes i l'altre cap a masses altes. L'origen de la cua de masses baixes és la pèrdua d'energia en la reconstrucció del fotó deguda a l'acceptància del calorímetre. Per altre banda, la cua de masses altes és deguda a la dispersió no gaussiana de l'error en el càlcul de la massa del mesó B^0 i també a un alt pile-up en el calorímetre provinent d'altres partícules a l'esdeveniment.

Composició del soroll

A l'hora d'extreure el nombre de candidats de senyal, és fonamental conèixer acuradament la composició del soroll i les seves proporcions. Aplicant la selecció del senyal a diferents mostres de dades simulades que es podrien confondre amb la senyal que busquem, s'ha estimat quin és el nivell de contaminació esperat respecte a la quantitat total d'esdeveniments de senyal i la seva forma funcional. La quantitat d'esdeveniments de background que

s'esperen respecte als de senyal ve donada per l'expressió

$$C_{H_b\to X} = \frac{N^{\rm sel}(H_b\to X)}{N^{\rm sel}(B^0\to K^{*0}\gamma)} = \frac{\epsilon_{\rm MC}(H_b\to X)}{\epsilon_{\rm MC}(B^0\to K^{*0}\gamma)} \times \frac{f_{H_b}}{f_d} \times \frac{\mathcal{B}(H_b\to X)}{\mathcal{B}(B^0\to K^{*0}\gamma)}\,, \tag{15}$$

on $\epsilon_{\rm MC}$ és l'eficiència total de la selecció extreta de la simulació, $\frac{f_{H_b}}{f_d}$ és el quocient entre fraccions d'hadronització del quark b, i $\mathcal{B}(H_b\to X)/\mathcal{B}(B^0\to K^{*0}\gamma)$ és la raó d'embrancament del canal de soroll estudiat respecte a la senyal $B^0\to K^{*0}\gamma$.

La Taula 2 resumeix tots els canals de soroll que s'han estudiat amb les seves contribucions relatives estimades.

Per extreure l'asimetria de les dades s'ha fet un ajust simultani sense *bins* de la massa invariant de $B^0\to K^{*0}\gamma$ i $\overline{B}^0\to \overline{K}^{*0}\gamma$ que maximitza la versemblança. El resultat de l'ajust és troba a la Fig. 10.

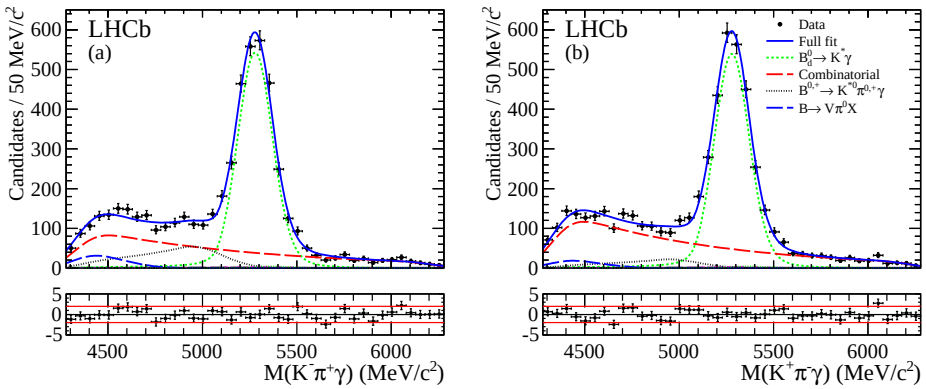

Figura 10 – Distribució de la massa invariant dels candidats $\overline{B}^0\to\overline{K}^{*0}\gamma$ (esquerra) i $B^0\to K^{*0}\gamma$ (dreta). Els punts negres són les dades i el resultat de l'ajust és la línia blava sòlida. Les diferents components del soroll també hi són presents. Els residus del χ^2 apareixen a sota dels ajustos amb les linies de ± 2 vegades l'interval de confiança en vermell.

El valor de l'asimetria de les dades és

$$A_{\rm RAW} = \frac{N(\overline{B}^0) - N(B^0)}{N(\overline{B}^0) + N(B^0)} = (0.3 \pm 1.7\,({\rm stat.}))\%\,, \tag{16}$$

on només es considera l'incertesa estadística. Aquesta asimetria s'ha de corretgir per possibles efectes de la reconstrucció de kaons i pions i per la

diferència en la producció de B^0 i $\overline{B}^0$. La relació entre l'asimetria física i la mesurada a les dades ve donada per

$$A_{CP}(B^0 \to K^{*0}\gamma) = A_{\mathrm{RAW}}(B^0 \to K^{*0}\gamma) - A_{\mathrm{D}}(K\pi) - \kappa A_{\mathrm{P}}(B^0)\,, \qquad (17)$$

L'asimetria de producció queda diluïda per l'oscil·lació dels mesons B^0. Aquest factor de dilució s'ha calculat fent servir la distribució del temps propi de desintegració dels mesons B^0, donant com a resultat $\kappa = 0.41 \pm 0.04$. Els valors de $A_{\mathrm{D}}(K\pi)$ i $A_{\mathrm{P}}(B^0)$ s'han pres d'un altre anàlisi d'LHCb. A més, una possible font de biaix al valor de l'asimetria de *CP* pot venir per possibles diferències entre les dades preses amb les dues polaritats de l'imant. Totes les correccions són presents a la Taula 3.

Fent servir l'Eq. 17 i les correccions de la Taula 3, el valor mesurat de l'asimetria directa de *CP* en desintegracions $B^0 \to K^{*0}\gamma$ és

$$A_{CP}(B^0 \to K^{*0}\gamma) = (0.8 \pm 1.7\,(\mathrm{stat.}) \pm 0.9\,(\mathrm{syst.}))\%\,. \qquad (18)$$

Conclusions

En aquest document s'ha presentat el treball realitzat per a calibrar el subdetector SPD d'LHCb amb rajos còsmics i amb les primeres dades de col·lisions *pp*. Gràcies a aquesta calibració, l'eficiència per a la detecció de les partícules a l'SPD és de més del 95% en promig. També s'ha estudiat l'alineament del detector respecte a les cambres de traces, on s'ha vist que hi ha un desplaçament vertical d'uns 10 mm cap abaix i una rotació al voltant de l'eix z horària a la part esquerra i antihorària a la dreta.

A més, fent servir totes les dades disponibles de 2011 corresponents a $1\,\mathrm{fb}^{-1}$ de col·lisions *pp* a una energia al centre de masses de $\sqrt{s} = 7\,\mathrm{TeV}$, s'ha mesurat l'asimetria directa de *CP* a la desintegració $B^0 \to K^{*0}\gamma$ com

$$A_{CP}(B^0 \to K^{*0}\gamma) = (0.8 \pm 1.7\,(\mathrm{stat.}) \pm 0.9\,(\mathrm{syst.}))\%\,. \qquad (19)$$

Aquest resultat és compatible amb la predicció del ME i és el més precís fet fins ara que millora en un 20% l'anterior millor mesura realitzada per l'experiment BaBar.

		$B^0 \to K^{*0}\gamma$
Track χ^2		< 5
Track IP χ^2		> 25
$p_{T,\text{track}}$	(MeV/c)	> 500
$\max(p_{T,\text{tracks}})$	(MeV/c)	> 1200
K $\text{DLL}_{\text{K}\pi}$		> 5
K DLL_{Kp}		> 2
π $\text{DLL}_{\text{K}\pi}$		< 0
K^{*0} ΔM_{PDG}	(MeV/c^2)	< 50
K^{*0} vertex χ^2		< 9
γ E_T	(MeV/c)	> 2600
γ CL_γ		> 0.25
π^0/γ separation		> 0.5
B^0 p_T	(MeV/c)	> 3000
B^0 IP χ^2		< 9
B^0 helicity		< 0.8
B^0 isolation $\Delta\chi^2$		> 2.0
B^0 flying distance χ^2		> 100
B^0 DIRA	(rad)	< 0.02
$\Delta M_{\text{PDG}}\, B$	(MeV/c^2)	< 1000

Taula 1 – Requeriments de la selecció de candidats de $B^0 \to K^{*0}\gamma$. Els requeriments estan dividits en cinc seccions: traces, identificació de partícules, K^{*0}, fotó i B^0.

	Raó d'embrancament $\times 10^6$	Contaminació relativa a $B^0 \to K^{*0}\gamma$
$\Lambda_b \to \Lambda^*\gamma$	estimat de les dades	$(1.0 \pm 0.3)\%$
$B_s^0 \to K^{*0}\gamma$	1.26 ± 0.31 (teo.)	$(0.8 \pm 0.2)\%$
$B^0 \to K^+\pi^-\pi^0$	$35.9^{+2.8}_{-2.4}$ (exp.)	$(0.5 \pm 0.1)\%$
$B_s^0 \to K^+\pi^-\pi^0$	estimat de la simetria SU(3)	$(0.2 \pm 0.2)\%$
$B_s^0 \to K^+K^-\pi^0$	estimat de la simetria SU(3)	$\mathcal{O}(10^{-4})$
$B^+ \to K^{*0}\pi^+\gamma$	20^{+7}_{-6} (exp.)	$(3.3 \pm 1.1)\%$
$B^+ \to K^+\pi^-\pi^0\gamma$	41 ± 4 (exp.)	$\mathcal{O}(5\%)$
$B^+ \to \phi K^+\gamma$	3.5 ± 0.6 (exp.)	3×10^{-4}
$B \to K^{*0}\pi^0$X	$\mathcal{O}(10\%)$	$\mathcal{O}(1\%)$

Taula 2 – Contaminació relativa al nombre d'esdeveniments de $B^0 \to K^{*0}\gamma$ esperats dintre de la finestra de massa de $\pm 1\,\mathrm{GeV}/c^2$. Les contribucions considerades s'agrupen en: desintegracions radiatives $h^+h^-\gamma$ (a dalt), desintegracions de B amb π^0 energètics sense quark c, $h^+h^-\pi^0$ (al centre) i desintegracions parcialment reconstruides (a sota). Les raons d'embrancament mesurades (exp.) o teòriques (teo.) es donen quan són disponibles.

		correcció (%)
Model del soroll	: ΔA_{bkg}	-0.2 ± 0.7
Asimetria de detecció	: $-A_{\mathrm{D}}(K\pi)$	$+1.0 \pm 0.2$
Polaritat de l'imant	: ΔA_M	$+0.1 \pm 0.2$
Producció de B^0	: $-\kappa A_{\mathrm{P}}(B^0)$	-0.4 ± 0.5
Total		$+0.5 \pm 0.9$

Taula 3 – Correccions a l'asimetria mesurada a les dades amb les seves incerteses.

1 Introduction

Particle physics has experienced a major development in both experimental results and theoretical calculations in the last few decades. From the experimental side, colliders as LEP or TEVATRON have helped unravelling the nature of fundamental particles. Regarding the flavour sector of the Standard Model, experiments at flavour factories as CLEO, BaBar and Belle have studied deeply the properties of b-, c- and s-quarks, being CP violation in all these sectors one of the most remarkable discoveries.

Despite all the efforts, the Standard Model is known to be an incomplete theory as it is not able to accommodate or explain accurately well-known phenomena. Some of the open issues are:

1. The inclusion of gravity.
2. The hierarchy problem.
3. The number of families of particles.
4. The matter-antimatter abundances in the Universe.

CP violation enters in the last problem [1], as it is a necessary condition —together with baryon number violation, C violation and interactions out of thermal equilibrium— for the matter-antimatter asymmetry to appear from symmetrical initial conditions. However, the amount of CP violation explained by the Standard Model [2] is not enough to explain the large asymmetry observed [3].

From the experimental side, CP violation was first discovered in neutral-kaon decays [4] in 1964 and in the b sector by the Belle [5] and the BaBar [6] collaborations in 2001. There are many observables in the b sector that lead to CP violation, and the Standard Model predicts them with great

precision. Moreover, large deviations from these predictions are expected in some beyond-the-Standard-Model scenarios. Thus, the B-meson system becomes an ideal place to test the Standard Model predictions and to search for new physics.

The main goal of this thesis is to measure the direct CP asymmetry of the $B^0 \to K^{*0}\gamma$ decay, using data from pp collisions at a centre-of-mass energy of $\sqrt{s} = 7\,\text{TeV}$ collected with the LHCb detector during the 2011 data-taking period.

Prior to the measurement of physical quantities, the detector needs to be calibrated to guarantee the maximum quality of the data. Another key point in this document is the calibration of the SPD detector, which is part of the calorimeter. The *in situ* calibration with data was performed before the LHC start-up using cosmic rays, and afterwards using pp collisions.

This document is organised as follows. Chapter 2 introduces the Standard Model of fundamental particles and interactions, as well as the oscillation of neutral mesons. The three types of CP-violation mechanisms are also described. A final word about the current searches of physics beyond the Standard Model in CP-related observables is given.

The LHC accelerator and the LHCb detector are introduced in Chapter 3, with an explanation of all of its components, paying special attention to the calorimeter. The performance of the detector with 2011 data is then reviewed including tracking, vertexing and particle identification.

The calibration process of the SPD sub-detector with cosmic data and with the first collision data at $\sqrt{s} = 0.9\,\text{TeV}$ and $\sqrt{s} = 7\,\text{TeV}$ is reported in Chapter 4. The alignment of the SPD with respect to the tracking system is also discussed.

Finally, the measurement of the direct CP violation in $B^0 \to K^{*0}\gamma$ decays with the full 2011 data sample is presented in Chapter 5. The procedure to select the signal, characterise the background, extract the asymmetry and the computation of systematic uncertainties are also given.

The conclusions of this work are given in Chapter 6.

2 Theoretical framework

This chapter sets the theoretical basis to study B-meson decays and, in particular, radiative decays. A brief introduction of the general framework, the Standard Model, is given, and also how it explains the neutral-meson oscillation phenomena. For neutral mesons, this natural oscillation can lead to CP violation, which is the main scope of this work. The sources of CP violation in the Standard Model and their size in B decays are finally presented.

2.1 The Standard Model

The Standard Model (SM) is the theory that describes the fundamental particles and their interactions. The interactions considered are the strong nuclear force, the weak nuclear force and the electromagnetic force. It is based on the local gauge invariance principle of the groups [7–10]

$$\mathrm{SU}(3)_C \times \mathrm{SU}(2)_L \times \mathrm{U}(1)_Y \,. \tag{2.1}$$

Here, Y and C represent the *weak hyper-charge* and the *colour charge* generators, respectively, and L refers to the left-handed leptons. The $\mathrm{SU}(3)_C \times \mathrm{SU}(2)_L \times \mathrm{U}(1)_Y$ gauge group is spontaneously broken to $\mathrm{SU}(3)_C \times \mathrm{U}(1)_Q$, where Q represents the electric charge generator defined as

$$Q = \frac{Y}{2} - T_3 \,, \tag{2.2}$$

with T_3 —a component of the weak isospin— being one of the three generators of SU(2).

In the SM, there are three fermion generations which can be represented as Dirac spinors. Fermions can be split into quarks and leptons depending

on whether they interact strongly or not. Both type of fermions can interact weakly and electromagnetically. There are six types of quarks, where each type is called *flavour*: the *up* (u); *down* (d); *strange* (s); *charm* (c); *beauty* (b) and *top* (t). The left-handed leptons and quarks are represented as $\mathrm{SU}(2)_L$ doublets, and the corresponding right-handed fields are represented as $\mathrm{SU}(2)_R$ singlets, which means that the right-handed particles in the SM do not interact weakly. Table 2.1 gathers all the SM fermions into doublets and singlets, while Table 2.2 summarises some of their properties.

$\begin{pmatrix}\nu_e\\ e^-\end{pmatrix}_L \quad \begin{pmatrix}u\\ d\end{pmatrix}_L$	e^-_R, u_R, d_R
$\begin{pmatrix}\nu_\mu\\ \mu^-\end{pmatrix}_L \quad \begin{pmatrix}c\\ s\end{pmatrix}_L$	μ^-_R, c_R, s_R
$\begin{pmatrix}\nu_\tau\\ \tau^-\end{pmatrix}_L \quad \begin{pmatrix}t\\ b\end{pmatrix}_L$	τ^-_R, t_R, b_R

Table 2.1 – Left-handed doublets and right-handed singlets in the SM for the first (top), second (middle) and third (bottom) generations. The corresponding antiparticles are omitted for simplicity. Note the absence of right-handed neutrinos in the SM.

The only difference among the three generations of fermions are their masses, heavier in the second and third families. Thus, quarks are often referred to as *up*- or *down*-type regarding its electrical charge. Each of these particles has its corresponding anti-particle with opposite charges.

In the SM, forces are mediated through the exchange of another type of particles, the gauge bosons. There are eight *gluons* (g) carrying the strong interaction, and three *weak bosons* ($W^\pm, Z^0$) that together with the *photon* (γ) carry the electroweak interaction. Table 2.3 summarises the SM boson properties.

2.1.1 The Standard Model Lagrangian

The SM Lagrangian can be separated into the quantum chromodynamics sector (QCD) [7] and the electroweak sector (EW) [8–10]. The Lagrangian for the QCD sector is given by

$$\mathcal{L}_{\mathrm{QCD}} = \imath\overline{U}\left(\partial_\mu - \imath g_s G^a_\mu T^a\right)\gamma^\mu U + \imath\overline{D}\left(\partial_\mu - \imath g_s G^a_\mu T^a\right)\gamma^\mu D \tag{2.3}$$

Particle	Q	Y	T_3	Mass (MeV/c^2)
ν_e	0	-1	1/2	$< 2.2 \times 10^{-6}$
e^-	-1	-1	-1/2	$0.510998910 \pm 0.000000013$
ν_τ	0	-1	1/2	< 0.19
μ^-	-1	-1	-1/2	105.6583668±0.0000038
ν_τ	0	-1	1/2	< 18.2
τ^-	-1	-1	-1/2	1776.82±0.16
u	+2/3	1/3	1/2	2.34 ± 0.19
d	-1/3	1/3	-1/2	4.78 ± 0.11
c	+2/3	1/3	1/2	1294 ± 4
s	-1/3	1/3	-1/2	100.2 ± 2.4
t	+2/3	1/3	1/2	$(172.9 \pm 0.6 \pm 0.9) \times 10^3$
b	-1/3	1/3	-1/2	$(4.670^{+0.018}_{-0.060}) \times 10^3$

Table 2.2 – Electric charge (Q), hyper-charge (Y), third component of isospin (T_3) and mass for the Standard Model fermions. The corresponding antiparticles are omitted for simplicity.

Particle	Force carrier	Electric charge	Mass (GeV/c^2)
γ	electromagnetic	0	0
W^+/W^-	weak	$+1/-1$	80.385±0.015
Z^0	weak	0	91.1876±0.0021
g	strong	0	0

Table 2.3 – Boson properties in the Standard Model.

where G^a_μ is the SU(3) gauge field containing the gluons, γ_μ are the Dirac matrices, D and U are the spinors related to the up- and down-type quarks and g_s is the strong coupling constant.

The EW sector Lagrangian is a Yang-Mills gauge theory [11] with the symmetry group $SU(2)_L \times U(1)_Y$, and it can be written as

$$\mathcal{L}_{\text{EW}} = \sum_\psi \overline{\psi}\gamma^\mu \left(\imath\partial_\mu - g'\frac{1}{2}Y B_\mu - g\frac{1}{2}\overrightarrow{\tau_L}\overrightarrow{W_\mu} \right) \psi \,, \tag{2.4}$$

where B_μ is the U(1) gauge field, Y is the weak hyper-charge, $\overrightarrow{W_\mu}$ is the three-component $SU(2)_L$ gauge field, $\overrightarrow{\tau_L}$ are the Pauli matrices, and g and g' are the coupling constants. The sub-index L indicates that the weak interaction only acts on left-handed fermions.

On Eqs. 2.3-2.4, it does not appear a mass term for the particles. However, the mass of all these particles has been measured experimentally to a great accuracy as shown in Tables 2.2-2.3. Therefore, a mechanism to give mass to the particles is needed. A possible way to generate masses based on the spontaneous symmetry breaking principle is known as *the Higgs mechanism* [12–17]. If a scalar potential of the form

$$V(\Phi) = \frac{1}{2}\mu^2\Phi^2 + \frac{1}{4}\lambda\Phi^4\,, \tag{2.5}$$

is introduced, with $\mu^2 < 0$, λ a positive parameter and Φ an external field, there are more than one possible minimum for the potential with a non-zero vacuum expectation value (*vev*), v=$\sqrt{-\mu^2/\lambda}$. The field Φ, or Higgs field, is a scalar doublet field of the $SU(2)_L$ group, that can be written as

$$\Phi = \frac{1}{\sqrt{2}}\begin{pmatrix}\phi^+\\ \phi^0\end{pmatrix} \tag{2.6}$$

The super-indices + and 0 indicates the electric charge of the field. With this term, the electroweak gauge fields acquire a mass without breaking the gauge symmetry, and it also provides a mass term for the fermions. The Higgs field itself also acquires a mass that is given by the relation

$$M_H = \sqrt{-2\mu^2}\,. \tag{2.7}$$

The ATLAS [18] and CMS [19] collaborations have reported the observation of a new boson that is consistent with the SM Higgs boson [20, 21]. Figure 2.1 shows the invariant-mass distribution of the $\gamma\gamma$ candidates in the CMS detector, where a clear peak with a statistical significance of 4.1 σ is seen.

Combining different decay channels the existence of a boson compatible with the SM Higgs boson with a mass of 125-126 MeV is established. Figure 2.2 shows the combined statistical significance of the measurements in terms of the observed local p-value for the ATLAS and CMS collaborations.

2.1.2 B physics in the Standard Model

The most useful tool to describe B-meson decays in the SM is the so-called *low-energy effective Hamiltonian* [22]. This Hamiltonian is an effective field

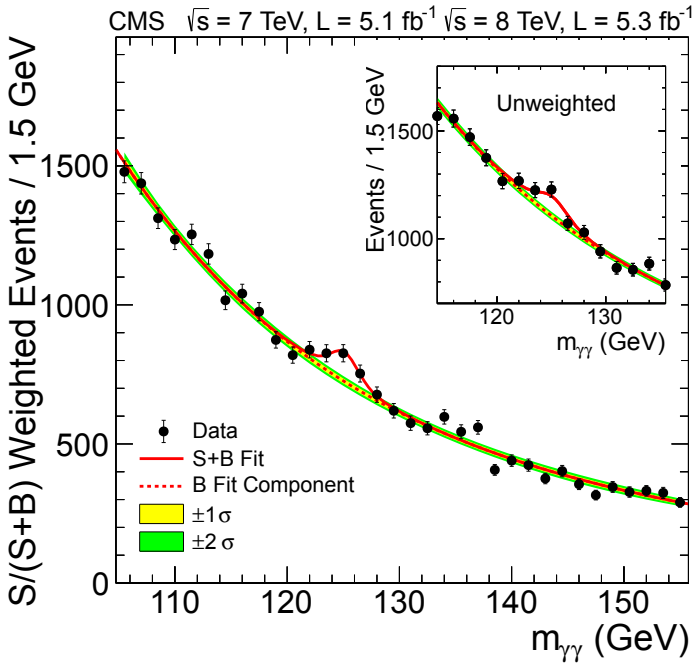

Figure 2.1 – Invariant-mass distribution of the di-photon candidates in the CMS experiment. Data are represented by black dots. The solid red line represents the fitted background and signal, the dashed red line is the background component, and the coloured bands represent the ± 1 and ± 2 standard deviation uncertainties on the background estimate. The inset shows the central part of the unweighed invariant-mass distribution.

theory [23, 24] built using the operator product expansion (OPE) formalism [25], where the element of the transition matrix $\mathcal{H}_{\text{eff}}$ —that connects the initial $|i\rangle$ with the final $|f\rangle$ state— can be expressed as

$$\langle f|\mathcal{H}_{\text{eff}}|i\rangle \propto \sum_k C_k(\mu)\langle f|Q_k(\mu)|i\rangle\,, \tag{2.8}$$

being μ the appropriate renormalisation scale that for B decays is typically chosen as m_b, $Q_k(\mu)$ the local operators that form a complete set for a given transition, and $C_k(\mu)$ the Wilson coefficients. The OPE formalism allows to separate the contribution of "long-distance" from "short-distance" effects in the decay amplitude. Long-distance effects are encoded in the hadronic matrix elements $\langle f|Q_k(\mu)|i\rangle$ and are due to non-perturbative strong interactions. The short-distance contributions can be computed perturbatively and

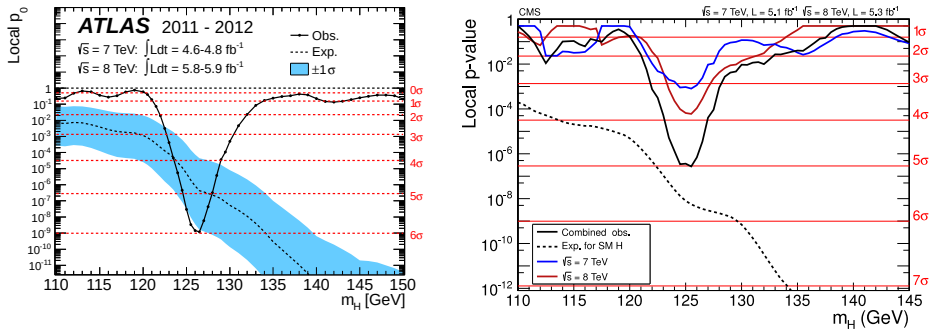

Figure 2.2 – Observed local p-value for ATLAS (left) and CMS (right) for 7 TeV and 8 TeV, and their combination as a function of the SM Higgs boson mass. The dashed lines show the expected local p-values for a SM Higgs boson with a mass m_{H}. The horizontal red lines indicates the statistical significances from 1 to 6 σ.

are described by the Wilson coefficient functions $C_k(\mu)$. As the perturbative part encodes physics at larger scales than μ, it carries information of particles heavier than the scale, which can come either from the SM or from physics beyond the SM.

The complete basis of operators that describe the effective Hamiltonian of weak decays of the b quark to the $q \in \{s, d\}$ quark, with $\Delta B = 1$ can be divided into the following five categories (a more detailed review can be found on [26]).

a) current-current operators

$$\begin{aligned} Q_1^{qq'} &= (\overline{q}_\alpha q'_\beta)_{V-A}(\overline{q'}_\beta b_\alpha)_{V-A} \\ Q_2^{qq'} &= (\overline{q}_\alpha q'_\alpha)_{V-A}(\overline{q'}_\beta b_\beta)_{V-A} \end{aligned} \tag{2.9}$$

b) QCD-penguin operators

$$\begin{aligned} Q_3^q &= (\overline{q}_\alpha b_\alpha)_{V-A} \sum_{q'} (\overline{q'}_\beta q'_\beta)_{V-A} \\ Q_4^q &= (\overline{q}_\alpha b_\beta)_{V-A} \sum_{q'} (\overline{q'}_\beta q'_\alpha)_{V-A} \\ Q_5^q &= (\overline{q}_\alpha b_\alpha)_{V-A} \sum_{q'} (\overline{q'}_\beta q'_\beta)_{V+A} \\ Q_6^q &= (\overline{q}_\alpha b_\beta)_{V-A} \sum_{q'} (\overline{q'}_\beta q'_\alpha)_{V+A} \end{aligned} \tag{2.10}$$

c) Electroweak-penguin operators

$$\begin{aligned} Q_7^q &= \frac{3}{2}(\overline{q}_\alpha b_\alpha)_{V-A} \sum_{q'} e_{q'}(\overline{q'}_\beta q'_\beta)_{V+A} \\ Q_8^q &= \frac{3}{2}(\overline{q}_\alpha b_\beta)_{V-A} \sum_{q'} e_{q'}(\overline{q'}_\beta q'_\alpha)_{V+A} \\ Q_9^q &= \frac{3}{2}(\overline{q}_\alpha b_\alpha)_{V-A} \sum_{q'} e_{q'}(\overline{q'}_\beta q'_\beta)_{V-A} \\ Q_{10}^q &= \frac{3}{2}(\overline{q}_\alpha b_\beta)_{V-A} \sum_{q'} e_{q'}(\overline{q'}_\beta q'_\alpha)_{V-A} \end{aligned} \tag{2.11}$$

d) Magnetic-penguin operators

$$\begin{aligned} Q_{7\gamma}^q &= \frac{e}{8\pi^2} m_{\rm b} \overline{q_\alpha} \sigma^{\mu\nu}(1+\gamma_5) b_\alpha F_{\mu\nu} \\ Q_{8G}^q &= \frac{g}{8\pi^2} m_{\rm b} \overline{q_\alpha} \sigma^{\mu\nu}(1+\gamma_5) T^a_{\alpha\beta} b_\beta G^a_{\mu\nu} \end{aligned} \tag{2.12}$$

e) Semi-leptonic operators

$$\begin{aligned} Q_{9V}^q &= \frac{3}{2}(\overline{q}_\alpha b_\alpha)_{V-A}(\bar{l}l)_V \\ Q_{10A}^q &= \frac{3}{2}(\overline{q}_\alpha b_\alpha)_{V-A}(\bar{l}l)_A \\ Q_{\nu\bar{\nu}}^q &= \frac{3}{2}(\overline{q}_\alpha b_\alpha)_{V-A}(\overline{\nu}\nu)_{V-A} \\ Q_{\mu\bar{\mu}}^q &= \frac{3}{2}(\overline{q}_\alpha b_\alpha)_{V-A}(\overline{\mu}\mu)_{V-A}\,, \end{aligned} \tag{2.13}$$

where α and β represent $\mathrm{SU}(3)_C$ colour indices, $V \pm A$ represent the Lorentz structures $\gamma_\mu(1 \pm \gamma_5)$, q' runs over the quark flavours being active at the scale $\mu = \mathcal{O}(m_{\rm b})$, i.e, $q' \in \{u, d, s, c\}$, and $e_{q'}$ is the corresponding electrical charge of the quark. These operators can be represented through Feynman diagrams as depicted in Fig. 2.3.

For the particular case of $B \to X_s\gamma$ radiative decays, represented by the quark transition $b \to s\gamma$, the effective Hamiltonian is described by only eight operators

$$\mathcal{H}_{\rm eff}(b \to s\gamma) = \frac{G_F}{\sqrt{2}} V_{ts}^* V_{tb} \left(\sum_{i=1}^{6} C_i(\mu) Q_i^q(\mu) + C_{7\gamma}(\mu) Q_{7\gamma}(\mu) + C_{8G}(\mu) Q_{8G}(\mu) \right), \tag{2.14}$$

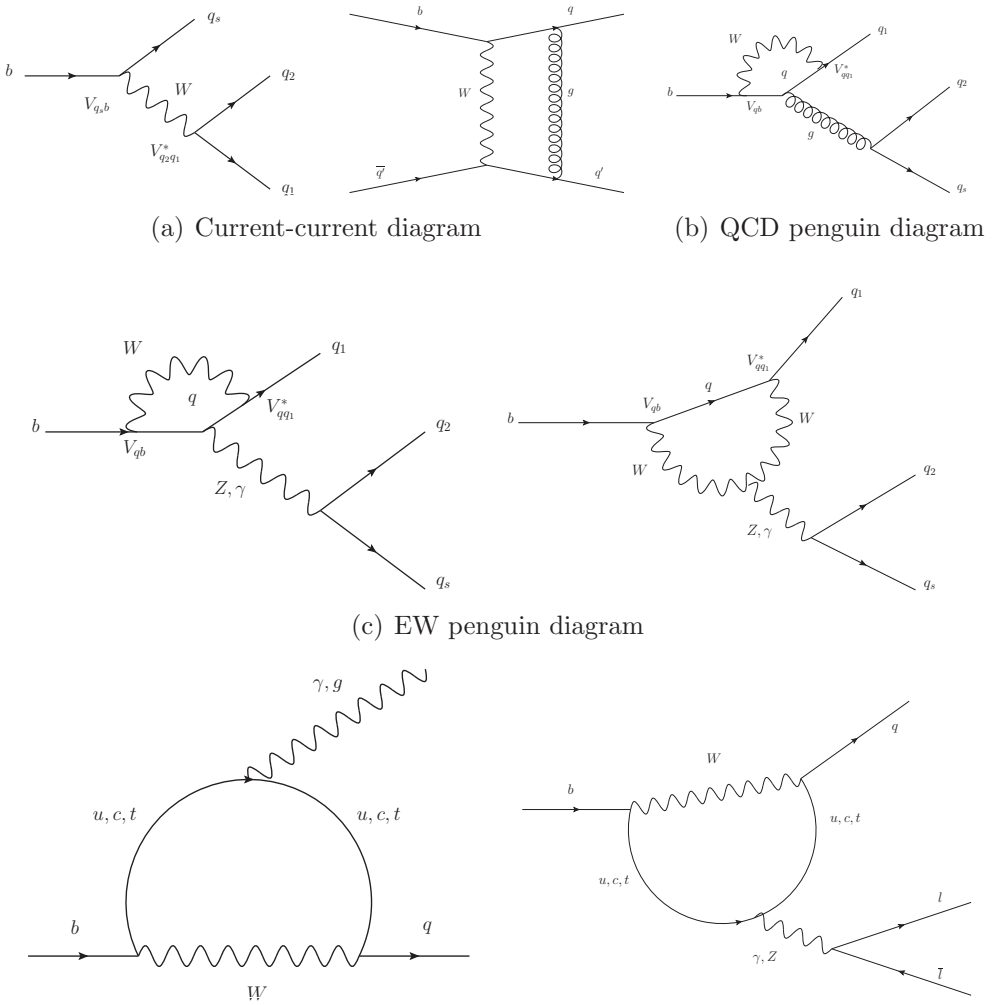

(a) Current-current diagram

(b) QCD penguin diagram

(c) EW penguin diagram

(d) Magnetic penguin diagram

(e) Semi-leptonic penguin diagram

Figure 2.3 – Feynman diagrams for the current-current (Fig. 2.3(a)), QCD-penguin (Fig. 2.3(b)), EW-penguin (Fig. 2.3(c)), magnetic-penguin (Fig. 2.3(d)) and semi-leptonic penguin (Fig. 2.3(e)) processes.

where G_F denotes the Fermi constant, V_{ij} are elements of the Cabibbo-Kobayashi-Maskawa matrix —detailed in Sec. 2.4—, and the renormalisation scale μ is of $\mathcal{O}(m_{\mathrm{b}})$. In the expression above, the term proportional to $V^*_{us}V_{ub}$ has been neglected in view of $|V^*_{us}V_{ub}/V^*_{ts}V_{tb}| < 0.02$.

2.2 Neutral meson oscillation

Considering any neutral self-conjugate pair of flavour meson eigenstates $|B^0\rangle$ and $|\overline{B}^0\rangle$, an arbitrary linear combination of the flavour eigenstates can be written as

$$a|B^0\rangle + b|\overline{B}^0\rangle\,, \tag{2.15}$$

with a and b being two complex parameters. The time evolution of the new state will follow the time dependent Schrödinger equation

$$i\frac{d}{dt}\begin{pmatrix} a \\ b \end{pmatrix} = \mathcal{H}\begin{pmatrix} a \\ b \end{pmatrix} \equiv \left(M - \frac{i}{2}\Gamma\right)\begin{pmatrix} a \\ b \end{pmatrix}, \tag{2.16}$$

where M and Γ are two 2×2 hermitian matrices representing the masses and lifetimes of the states. CPT invariance ensures that the diagonal elements of the matrix are equal, hence $\mathcal{H}_{11} = \mathcal{H}_{22}$ [27]. This implies that the particle and anti-particle masses and lifetimes are equal

$$\begin{aligned} M_{11} &= M_{22} \equiv M \\ \Gamma_{11} &= \Gamma_{22} \equiv \Gamma \end{aligned} \tag{2.17}$$

The light $|B_L\rangle$ and heavy $|B_H\rangle$ mass eigenstates of the matrix $\mathcal{H}$ can be written as a linear combination of the particle and anti-particle states $|B^0\rangle$, $|\overline{B}^0\rangle$

$$\begin{aligned} |B_L\rangle &= p|B^0\rangle + q|\overline{B}^0\rangle \\ |B_H\rangle &= p|B^0\rangle - q|\overline{B}^0\rangle\,, \end{aligned} \tag{2.18}$$

with p and q normalised to unity

$$|p^2| + |q^2| = 1. \tag{2.19}$$

Solving the characteristic equation

$$|\mathcal{H} - EI| = 0\,, \tag{2.20}$$

where I is the 2×2 unit matrix, one can find the two eigenvalues $E_{1,2}$ as

$$\begin{aligned} E_1 &= M - \frac{i}{2}\Gamma + \sqrt{(M_{12} - \frac{i}{2}\Gamma_{12})(M_{12}^* - \frac{i}{2}\Gamma_{12}^*)} \equiv M_1 - \frac{i}{2}\Gamma_1 \\ E_2 &= M - \frac{i}{2}\Gamma - \sqrt{(M_{12} - \frac{i}{2}\Gamma_{12})(M_{12}^* - \frac{i}{2}\Gamma_{12}^*)} \equiv M_2 - \frac{i}{2}\Gamma_2\,, \end{aligned} \tag{2.21}$$

and then, the relation between p and q can be obtained through the eigenvector equations

$$(\mathcal{H} - EI)\begin{pmatrix} p \\ \pm q \end{pmatrix} = 0\,, \tag{2.22}$$

leading to the relation

$$\frac{q}{p} = \sqrt{\frac{M_{12}^* - \frac{i}{2}\Gamma_{12}^*}{M_{12} - \frac{i}{2}\Gamma_{12}}}\,. \tag{2.23}$$

The time evolution of the initial states $|B_L\rangle$ and $|B_H\rangle$ is obtained by means of the Schrödinger equation, yielding to

$$\begin{aligned} |B_L(t)\rangle &= e^{-i(M_1 - \frac{i}{2}\Gamma_1)t}|B_L\rangle \\ |B_H(t)\rangle &= e^{-i(M_2 - \frac{i}{2}\Gamma_2)t}|B_H\rangle\,, \end{aligned} \tag{2.24}$$

using Eq. 2.18 and Eq. 2.24, the time evolution of the states $|B^0\rangle$ and $|\overline{B}^0\rangle$ can be found as

$$\begin{aligned} |B^0(t)\rangle = \frac{1}{2}\Bigg[&\left(e^{-i(M_1 - i\frac{\Gamma_1}{2})t} + e^{-i(M_2 - i\frac{\Gamma_2}{2})t}\right)|B^0\rangle + \\ &+ \frac{q}{p}\left(e^{-i(M_1 - i\frac{\Gamma_1}{2})t} - e^{-i(M_2 - i\frac{\Gamma_2}{2})t}\right)|\overline{B}^0\rangle\Bigg] \equiv \\ &\equiv f_+(t)|B^0\rangle + \frac{q}{p}f_-(t)|\overline{B}^0\rangle \end{aligned} \tag{2.25}$$

$$\begin{aligned} |\overline{B}^0(t)\rangle = \frac{1}{2}\Bigg[&\frac{p}{q}\left(e^{-i(M_1 - i\frac{\Gamma_1}{2})t} - e^{-i(M_2 - i\frac{\Gamma_2}{2})t}\right)|B^0\rangle + \\ &+ \left(e^{-i(M_1 - i\frac{\Gamma_1}{2})t} + e^{-i(M_2 - i\frac{\Gamma_2}{2})t}\right)|\overline{B}^0\rangle\Bigg] \equiv \\ &\equiv \frac{p}{q}f_-(t)|B^0\rangle + f_+(t)|\overline{B}^0\rangle\,, \end{aligned} \tag{2.26}$$

where the $f_\pm(t)$ notation has been introduced for further simplicity. Thus, the probability of finding a state $|B^0\rangle$ or $|\overline{B}^0\rangle$ at a time t is given by

$$\begin{aligned} \mathcal{P}(B^0 \to B^0 : t) &= |\langle B^0|B^0(t)\rangle|^2 = \frac{1}{4}\left(e^{-\Gamma_1 t} + e^{-\Gamma_2 t} + 2e^{-\overline{\Gamma}t}\cos(\Delta M t)\right) \\ \mathcal{P}(\overline{B}^0 \to \overline{B}^0 : t) &= |\langle \overline{B}^0|\overline{B}^0(t)\rangle|^2 = \frac{1}{4}\left(e^{-\Gamma_1 t} + e^{-\Gamma_2 t} - 2e^{-\overline{\Gamma}t}\cos(\Delta M t)\right)\,, \end{aligned} \tag{2.27}$$

being $\overline{\Gamma}$ the average decay width defined as $\overline{\Gamma} = (\Gamma_1 + \Gamma_2)/2$ and ΔM is difference in mass of the two eigenstates $\Delta M = M_2 - M_1$. This implies that the states $|B^0\rangle$ and $|\overline{B}^0\rangle$ oscillates naturally from an initial pure state $|B^0\rangle$ or $|\overline{B}^0\rangle$. The oscillatory character is governed by the parameter $\Delta M/\overline{\Gamma}$.

2.3 *CP* violation in *B*-meson decays

Using Eqs. 2.25-2.26, the time dependent decay amplitudes of the states $|B^0\rangle$ and $|\overline{B}^0\rangle$ to the same final state f can be written as

$$\Gamma_f(t) = |\langle f|\mathcal{H}|B^0(t)\rangle|^2 = |A_f|^2 \left[|f_+(t)|^2 + \left(\frac{q\overline{A_f}}{pA_f}\right)^2 |f_-(t)|^2 + \right. \\ \left. +2\mathcal{R}e\left(f_+^*(t) f_-(t) \frac{q}{p}\frac{\overline{A_f}}{A_f}\right)\right] \tag{2.28}$$

$$\overline{\Gamma}_f(t) = |\langle f|\mathcal{H}|\overline{B}^0(t)\rangle|^2 = |A_f|^2 \left[\left|\frac{\overline{A_f}}{A_f}\right|^2 |f_+(t)|^2 + \left(\frac{p}{q}\right)^2 |f_-(t)|^2 + \right. \\ \left. +2\left(\frac{p}{q}\right)^2 \mathcal{R}e\left(f_+^*(t) f_-(t) \frac{q}{p}\frac{\overline{A_f^*}}{A_f}\right)\right] , \tag{2.29}$$

where $A_f = \langle f|\mathcal{H}|B^0(t)\rangle$ and $\overline{A_f} = \langle f|\mathcal{H}|\overline{B}^0(t)\rangle$ are the instantaneous decay amplitudes. Therefore, any difference between the rates $\Gamma_f(t)$ and $\overline{\Gamma}_f(t)$ will be a proof of *CP* violation. Analysing Eqs. 2.28-2.29 one can identify three different possibilities for *CP* violation to arise.

1. *CP* violation in the decay if $\left|\frac{\overline{A_f}}{A_f}\right|^2 \neq 1$
2. *CP* violation in the mixing if $\left|\frac{p}{q}\right|^2 \neq 1$
3. *CP* violation in the interference if $\mathcal{I}m\left\{\frac{q\overline{A_f}}{pA_f}\right\} \neq 0$

As in the *B*-meson system $\Delta\Gamma$ is small, it is convenient to re-write the above expressions factorising the dependence on ΔM and $\Delta\Gamma$. This process

yields to

$$\Gamma_f(t) = \frac{|A_f|^2}{2} e^{-\overline{\Gamma}t} \left\{ (1+|\lambda|^2)\cosh\left(\frac{\Delta\Gamma t}{2}\right) + 2\mathcal{R}e\{\lambda\}\sinh\left(\frac{\Delta\Gamma t}{2}\right) + \right. \\ \left. + (1-|\lambda|^2)\cos(\Delta M t) + 2\mathcal{I}m\{\lambda\}\sin(\Delta M t) \right\} \tag{2.30}$$

$$\overline{\Gamma_f}(t) = \frac{\left|\overline{A}_f\right|^2}{2|\lambda|^2} e^{-\overline{\Gamma}t} \left\{ (1+|\lambda|^2)\cosh\left(\frac{\Delta\Gamma t}{2}\right) + 2\mathcal{R}e\{\lambda\}\sinh\left(\frac{\Delta\Gamma t}{2}\right) - \right. \\ \left. - (1-|\lambda|^2)\cos(\Delta M t) - 2\mathcal{I}m\{\lambda\}\sin(\Delta M t) \right\} , \tag{2.31}$$

being $\lambda = \frac{p\overline{A_f}}{qA_f}$ a factor —with real and imaginary part— that quantifies the amount of *CP* violation. If we now consider the final self-conjugated state $\overline{f}$, the time dependent decay rates can be written similarly as

$$\Gamma_{\overline{f}}(t) = \frac{\left|A_{\overline{f}}\right|^2}{2|\overline{\lambda}|^2} e^{-\overline{\Gamma}t} \left\{ (1+|\overline{\lambda}|^2)\cosh\left(\frac{\Delta\Gamma t}{2}\right) + 2\mathcal{R}e\{\overline{\lambda}\}\sinh\left(\frac{\Delta\Gamma t}{2}\right) - \right. \\ \left. - (1-|\overline{\lambda}|^2)\cos(\Delta M t) - 2\mathcal{I}m\{\overline{\lambda}\}\sin(\Delta M t) \right\} \tag{2.32}$$

$$\overline{\Gamma_{\overline{f}}}(t) = \frac{\left|\overline{A}_{\overline{f}}\right|^2}{2} e^{-\overline{\Gamma}t} \left\{ (1+|\overline{\lambda}|^2)\cosh\left(\frac{\Delta\Gamma t}{2}\right) + 2\mathcal{R}e\{\overline{\lambda}\}\sinh\left(\frac{\Delta\Gamma t}{2}\right) + \right. \\ \left. + (1-|\overline{\lambda}|^2)\cos(\Delta M t) + 2\mathcal{I}m\{\overline{\lambda}\}\sin(\Delta M t) \right\} , \tag{2.33}$$

with $\overline{\lambda} = \frac{pA_{\overline{f}}}{q\overline{A_{\overline{f}}}}$.

2.3.1 *CP* violation in the decay

CP violation in the decay occurs when the decay rates of a meson B to a final state f is different from the decay rate of its anti-particle $\overline{B}$ to the anti-particle of the final state $\overline{f}$. This implies

$$\frac{\Gamma(B \to f)}{\Gamma(\overline{B} \to \overline{f})} \neq 1 . \tag{2.34}$$

The amount of *CP* violation can be measured from the asymmetry

$$\frac{\Gamma_f - \overline{\Gamma_{\overline{f}}}}{\Gamma_f + \overline{\Gamma_{\overline{f}}}} = \frac{1 - \left|\frac{\overline{A_{\overline{f}}}}{A_f}\right|^2}{1 + \left|\frac{\overline{A_{\overline{f}}}}{A_f}\right|^2} . \tag{2.35}$$

The origin of this type of *CP* violation is due to the different amplitude in the decay process and it is the only possible source of *CP* violation in charged B mesons.

2.3.2 *CP* violation in the mixing

From Eqs. 2.28-2.29 if $\left|\frac{q}{p}\right| \neq 1$, there would be *CP* violation due to the fact that the magnitudes of the off-diagonal elements in the mass and decay matrices in Eq. 2.23 are not equal. This means that the mixing rate between $|B^0\rangle \to |\overline{B}^0\rangle$ and $|\overline{B}^0\rangle \to |B^0\rangle$ is different and it is a result of the mass eigenstates not being *CP* eigenstates. In the B system, *CP* violation in the mixing can be seen in semileptonic B decays though the semi-leptonic asymmetry

$$A_{sl} = \frac{\Gamma\left(\overline{B} \to l^- \nu X\right) - \Gamma\left(B \to l^+ \nu X\right)}{\Gamma\left(\overline{B} \to l^- \nu X\right) + \Gamma\left(B \to l^+ \nu X\right)} = \frac{1 - \left|\frac{q}{p}\right|^4}{1 + \left|\frac{q}{p}\right|^4} . \tag{2.36}$$

2.3.3 *CP* violation in the interference

Considering a neutral B meson decaying into a final *CP* eigenstate, this state can be accessible through B^0 and $\overline{B}^0$ decays. The amount of *CP* violation can be measured using the time-dependent *CP* asymmetry

$$A(t) = \frac{\Gamma_f - \overline{\Gamma}_f}{\Gamma_f + \overline{\Gamma}_f} = \frac{(1 - |\lambda|^2)\cos(\Delta M t) + 2\mathcal{I}m\{\lambda\}\sin(\Delta M t)}{(1 + |\lambda|^2)\cosh\left(\frac{\Delta\Gamma t}{2}\right) + 2\mathcal{R}e\{\lambda\}\sinh\left(\frac{\Delta\Gamma t}{2}\right)} . \tag{2.37}$$

In the B system, where $\Delta\Gamma$ is small, the asymmetry can be written as

$$A(t) = \frac{1 - |\lambda|^2}{1 + |\lambda|^2}\cos(\Delta M t) + \frac{2\mathcal{I}m\{\lambda\}}{1 + |\lambda|^2}\sin(\Delta M t) . \tag{2.38}$$

The coefficient accompanying the cosine term is due to the direct *CP* violation when $q/p = 1$, and the one accompanying the sine term is due to

the *CP* violation in the interference between the decay and the mixing. Thus, *CP* violation in the interference is present when $\mathcal{I}m\{\lambda\} \neq 0$.

2.4 *CP* violation in the Standard Model

In the SM with three fermion families, the charged weak current can be written as

$$J_\mu = (\bar{u}, \bar{c}, \bar{t})_L \, \gamma_\mu V_{\text{CKM}} \begin{pmatrix} d \\ s \\ b \end{pmatrix}_L , \tag{2.39}$$

where V_{CKM} is a unitary 3×3 matrix, known as the Cabibbo-Kobayashi-Maskawa matrix [2, 28], that describes the rotation of the weak eigenstates to mass eigenstates, and is defined as

$$V_{\text{CKM}} = \begin{pmatrix} V_{ud} & V_{us} & V_{ub} \\ V_{cd} & V_{cs} & V_{cb} \\ V_{td} & V_{ts} & V_{tb} \end{pmatrix} \tag{2.40}$$

The unitary condition, imposes that the matrix can be described by only four independent parameters. Introducing the terms $c_{ij} = \cos\theta_{ij}$ and $s_{ij} = \sin\theta_{ij}$, with i and j being generation labels $(i, j = 1, 2, 3)$, the standard parametrisation of the matrix [29] can be written as

$$V_{\text{CKM}} = \begin{pmatrix} c_{12}c_{13} & s_{12}c_{13} & s_{13}e^{-i\delta} \\ -s_{12}c_{23} - c_{12}s_{23}s_{13}e^{i\delta} & c_{12}c_{23} - s_{12}s_{23}s_{13}e^{i\delta} & s_{23}c_{13} \\ s_{12}s_{23} - c_{12}c_{23}s_{13}e^{i\delta} & -s_{23}c_{12} - s_{12}c_{23}s_{13}e^{i\delta} & c_{23}c_{13} \end{pmatrix} , \tag{2.41}$$

where δ is the necessary *CP* violating phase, and the only source of *CP* violation in the SM. A more useful parametrisation —from the experimental point of view— was introduced by Wolfenstein [30], and consists on an expansion as a power series of the small parameter $\lambda = s_{12}$, known as the Cabibbo angle [28]. It has the benefits of taking into account the strength of the quark transition through the charged weak current. The chosen parameters are λ, A, ρ and η, with the first three representing angles and the last being a complex phase. The expansion of the matrix in terms of λ up to the fifth order is

$$V_{\text{CKM}} = \begin{pmatrix} 1 - \frac{1}{2}\lambda^2 + \frac{1}{4}\lambda^4 & \lambda & A\lambda^3(\rho - \imath\eta) \\ -\lambda + \frac{1}{2}A^4\lambda^4 - A^2\lambda^5(\rho - \imath\eta) & 1 - \frac{1}{2}\lambda^2 + \frac{1}{4}\lambda^4(1 - 2A^2) & A\lambda^2 \\ A\lambda^3(1 - \overline{\rho} - \imath\overline{\eta}) & -A\lambda^2 + A\lambda^4\left(\frac{1}{2} - \rho - \imath\eta\right) & 1 - \frac{1}{2}A^2\lambda^4 \end{pmatrix} , \tag{2.42}$$

where $\overline{\rho}$ and $\overline{\eta}$ are defined as $\overline{\rho} = \rho(1 - \lambda^2/2)$ and $\overline{\eta} = \eta(1 - \lambda^2/2)$. The relations between the standard and the Wolfenstein parametrisations are given by

$$s_{12} = \lambda\,, \qquad s_{23} = A\lambda^2\,, \qquad s_{13}e^{i\delta} = A\lambda^3(\rho - i\eta)\,. \tag{2.43}$$

The unitarity of the CKM matrix, implies the existence of six orthogonality conditions between any pairs of rows or columns in the matrix [31]. These conditions can be written as:

$$\begin{aligned}
V_{ud}V_{ub}^* + V_{cd}V_{cb}^* + V_{td}V_{tb}^* &= 0 \quad (db)\\
V_{us}V_{ub}^* + V_{cs}V_{cb}^* + V_{ts}V_{tb}^* &= 0 \quad (sb)\\
V_{ud}V_{us}^* + V_{cd}V_{cs}^* + V_{td}V_{ts}^* &= 0 \quad (ds)\\
V_{ud}V_{td}^* + V_{us}V_{ts}^* + V_{ub}V_{tb}^* &= 0 \quad (ut)\\
V_{cd}V_{td}^* + V_{cs}V_{ts}^* + V_{cb}V_{tb}^* &= 0 \quad (ct)\\
V_{ud}V_{cd}^* + V_{us}V_{cs}^* + V_{ub}V_{cb}^* &= 0 \quad (uc)
\end{aligned} \tag{2.44}$$

As the CKM matrix has a real and an imaginary part, the relations in Eq. 2.44 require the sum of three complex numbers to vanish. This can be represented geometrically in the complex plane $(\overline{\rho}, \overline{\eta})$ as a triangle. All six triangles have the same area, equal to $J_{CP}/2$, which is a measure of the *CP* violation in the SM. It is common to refer to the triangle (db) as *the unitary triangle*, with its angles denoted as α, β and γ [32], and defined as

$$\alpha \equiv \arg\left(-\frac{V_{td}V_{tb}^*}{V_{ud}V_{ub}^*}\right)\,, \quad \beta \equiv \arg\left(-\frac{V_{cd}V_{cb}^*}{V_{td}V_{tb}^*}\right)\,, \quad \gamma \equiv \arg\left(-\frac{V_{ud}V_{ub}^*}{V_{cd}V_{cb}^*}\right)\,, \tag{2.45}$$

with $\alpha + \beta + \gamma = \pi$. Figure 2.4 represents the current knowledge of the parameters of the unitary triangle (db) [33].

2.5 *CP* violation in *B* decays

As explained in the previous section, the condition for *CP* violation to appear is the existence of two contributions to the decay process with different weak and strong phases so that $\left|\overline{A}/A\right| \neq 1$. Purely leptonic and semi-leptonic decays are dominated by a single diagram and then are unlikely to exhibit significant direct *CP* violation. On the other hand, non-leptonic decays often have two comparable terms, and thus can have significant direct *CP* violation.

Regarding the processes involved in the decay, *B* decays can be grouped into five categories. In the first two, it is expected to find zero or very small

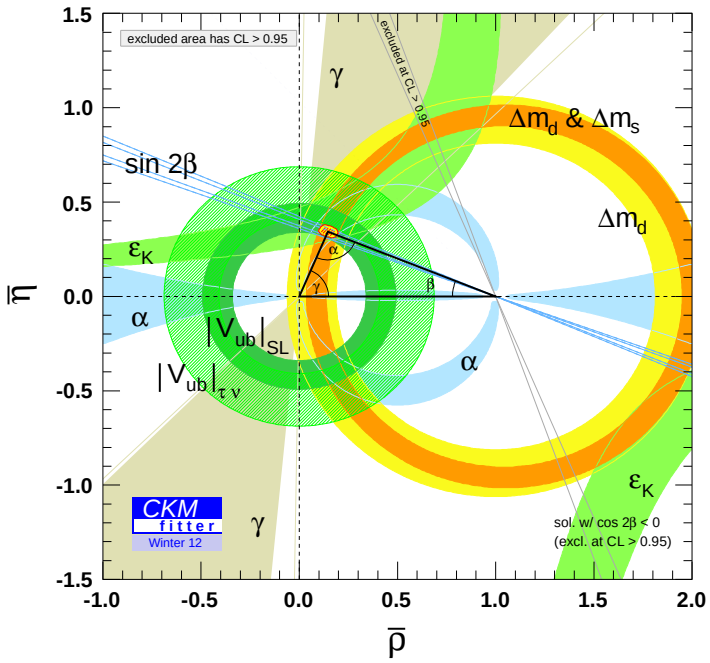

Figure 2.4 – Current constrains on the unitary triangle (db).

CP asymmetries whereas in the other three, direct CP violation could be significant. The five categories are as follow:

- Decays dominated by a single term: $b \to c\bar{c}s$ and $b \to s\bar{s}s$. Here, the SM predicts zero or very small direct CP violation due to the Cabibbo suppression of the second term. Examples are $B^+ \to J/\psi K^+$ and $B^+ \to \phi K^+$.

- Decays with a small second term: $b \to c\bar{c}d$ and $b \to u\bar{u}d$. It is expected that penguin-only contributions are suppressed compared to tree contributions. Then, these modes will have small direct CP violation effects. Examples are $B^0 \to D^+D^-$ and $B^0 \to \pi^+\pi^-$.

- Decays with a suppressed tree contribution: $b \to u\bar{u}s$. The tree amplitude is suppressed by small mixing angles, $V_{ub}V_{us}^*$. The no-tree term may be comparable or even dominate, and provide large interference effects. An example is $B^0 \to \rho K$.

- Decays with no tree contribution: $b \to s\bar{s}d$. The interference comes

from penguin contributions with different down-type quarks in the loop. An example is $B^0 \to K^+K^-$.

- Radiative decays: $b \to s\gamma$. Penguin contribution with different down-type quarks in the loop interfere with the leading contributions coming from electromagnetic penguins. An example is $B^0 \to K^{*0}\gamma$.

3 The LHCb detector at the Large Hadron Collider

This chapter describes the LHC accelerator complex and its running conditions. As the analysis presented in Chapter 5 is done with 2011 data, special emphasis on the 2011 running conditions will be make. The LHCb experiment with all its sub-detectors plus the trigger, online and offline systems are also detailed. The analysis of the data presented in the forthcoming chapter relies on the tracking, vertexing and particle identification capabilities of the LHCb detector. Hence, the detector performance focusing on these issues with 2010 and 2011 data is presented.

3.1 The Large Hadron Collider

The Large Hadron Collider (LHC) [34] is a two-ring superconducting hadron accelerator and collider installed in the 26.7 km tunnel constructed for the LEP machine, between 45 and 170 m underneath the surface of the Geneva region. The aim of the LHC and the experiments working at it, is to reveal physics beyond the SM, either through direct searches of new processes or through indirect ways, as the precise measurement of SM parameters. The search for the Higgs boson is also a fundamental objective of the experiments, in particular of ATLAS and CMS. In order to accomplish the experimental goals, the collisions at the LHC will take place at a design centre-of-mass energy of $\sqrt{s} = 14\,\text{TeV}$.

The number of events of a particular process generated at a collider is given by

$$N_{\text{event}} = \mathcal{L}\sigma_{\text{event}}\,, \tag{3.1}$$

where σ_{event} is the cross-section for the event under study and $\mathcal{L}$ is the machine luminosity. The machine luminosity depends only on machine parameters, and for a Gaussian beam distribution it is given by

$$\mathcal{L} = \frac{N_b^2 n_b f_{\text{rev}} \gamma_r}{4\pi\epsilon_n \beta^*} F \,, \tag{3.2}$$

where N_b is the number of particles per bunch, n_b is the number of bunches per beam, f_{rev} is the revolution frequency, γ_r is the relativistic gamma factor, ϵ_n is the normalised transverse beam emittance, β^* is the beta function at the collision point and F is the geometrical luminosity reduction factor due to the crossing angle at the interaction point. Assuming round beams with equal beam parameters, the last can be expressed as

$$F = \left(1 + \left(\frac{\theta_c \sigma_z}{2\sigma^*}\right)^2\right)^{-1/2} \,, \tag{3.3}$$

where θ_c is the full crossing angle at the interaction point, σ_z is the RMS bunch length and σ^* the transverse RMS beam size at the interaction point.

The LHC peak luminosity is $\mathcal{L} = 10^{34}\,\text{cm}^2\,\text{s}$ for proton-proton operation and it is the nominal working point for the ATLAS [18] and CMS [19] detectors. The peak luminosity at the LHCb experiment is $\mathcal{L} = 2 \times 10^{32}\,\text{cm}^2\,\text{s}$. In addition to the proton beams, LHC also operates with lead-ion beams at a peak luminosity of $\mathcal{L} = 2 \times 10^{27}\,\text{cm}^2\,\text{s}$, with ALICE [35] as a dedicated experiment to study these collisions. Then, three types of operations are expected: *pp*, *p*-lead and lead-lead.

The LHC has eight arcs and eight straight sections. Each straight section is approximately 528 m long and can serve as an experimental or utility insertion. The two high luminosity experimental insertions are located at diametrically opposite straight sections: the ATLAS experiment is located at Point 1 and the CMS experiment at Point 5. Two more experimental insertions are located at Point 2 (ALICE) and Point 8 (LHCb), which also include the injection systems for Beam 1 and Beam 2, respectively. The remaining four straight sections do not have beam crossings.

The LHC has independent magnetic fields and vacuum chambers, and only common sectors at the interaction region where the experiments are located. The nominal number of bunches of the LHC is 2808 with a bunch spacing of 25 ns, this translates into a nominal collision frequency of 40 MHz.

The LHC relies on superconducting magnets cooled to a temperature of 1.9 K, using super-fluid helium, and operate at magnetic fields above 8 T. The LHC ring accommodates 1232 cryodipoles —as the one depicted in Fig. 3.1— mainly in the arc sections. The core of the cryodipole is the *dipole cold mas*,

which contains all the components cooled by super-fluid helium. The dipole cold mass provides two apertures for the cold bore tubes, i.e. the tubes where the proton beams will circulate. It has an overall length of about 16.5 m, a diameter of 570 mm at room temperature, and a mass of about 27.5 tons. The Short Straight Section (SSS) of the arc contains the main quadrupoles.

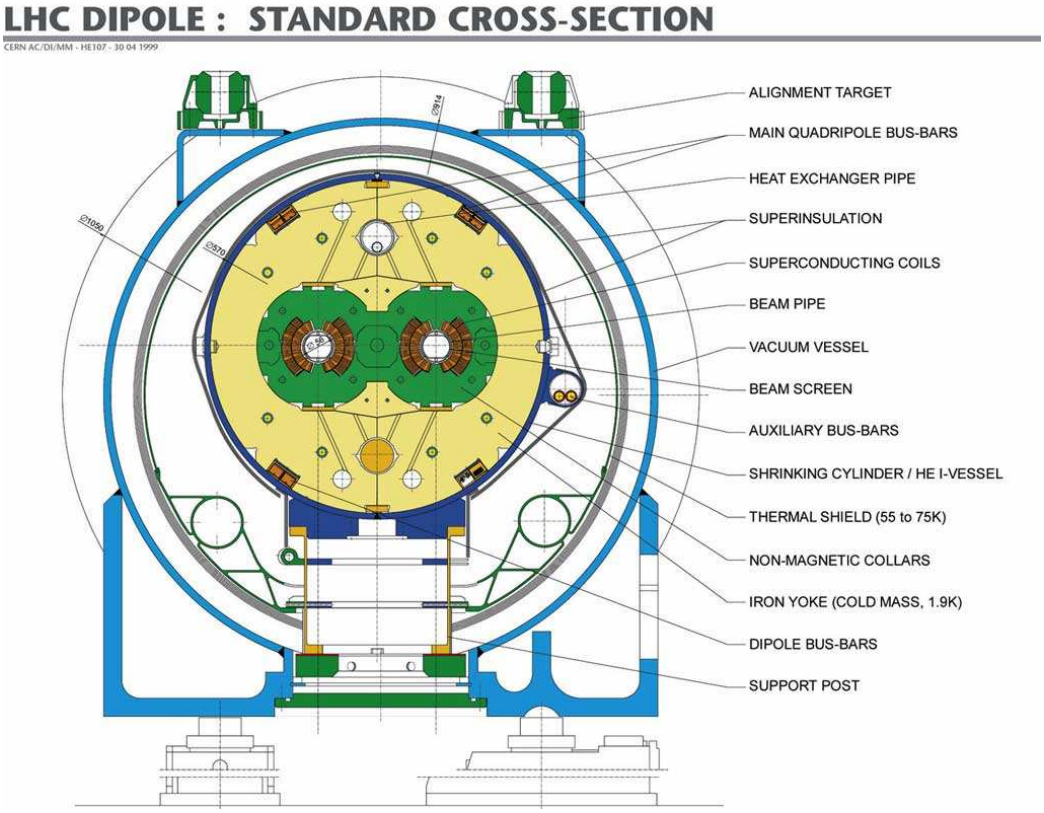

Figure 3.1 – Cross-section of a LHC cryodipole.

3.1.1 Accelerator chain

Proton beams come from the injector chain: Linac2 — Proton Synchrotron Booster (PSB) — Proton Synchrotron (PS) — Super Proton Synchrotron (SPS). Hydrogen gas is used as the proton source, its molecules are ionised and injected into the Linac2 where they are accelerated to 50 MeV. Then, they enter into the Proton Synchrotron Booster system where they are accumulated into the Booster and accelerated to 1.4 GeV in the first step, and then injected into the Proton Synchrotron where they reach an energy of

25 GeV. Afterwards, they leave the PSB-PS system to be injected into the Super Proton Synchrotron where they are accelerated to 450 GeV. Finally, they are extracted from the SPS and injected into the LHC where they reach the final energy of 7 TeV. The final extraction is accomplished through two transfer tunnels each of 2.5 km length that links the LHC accelerator with the CERN accelerator complex. The complete accelerator chain with the LHC at its end can be seen in Fig. 3.2.

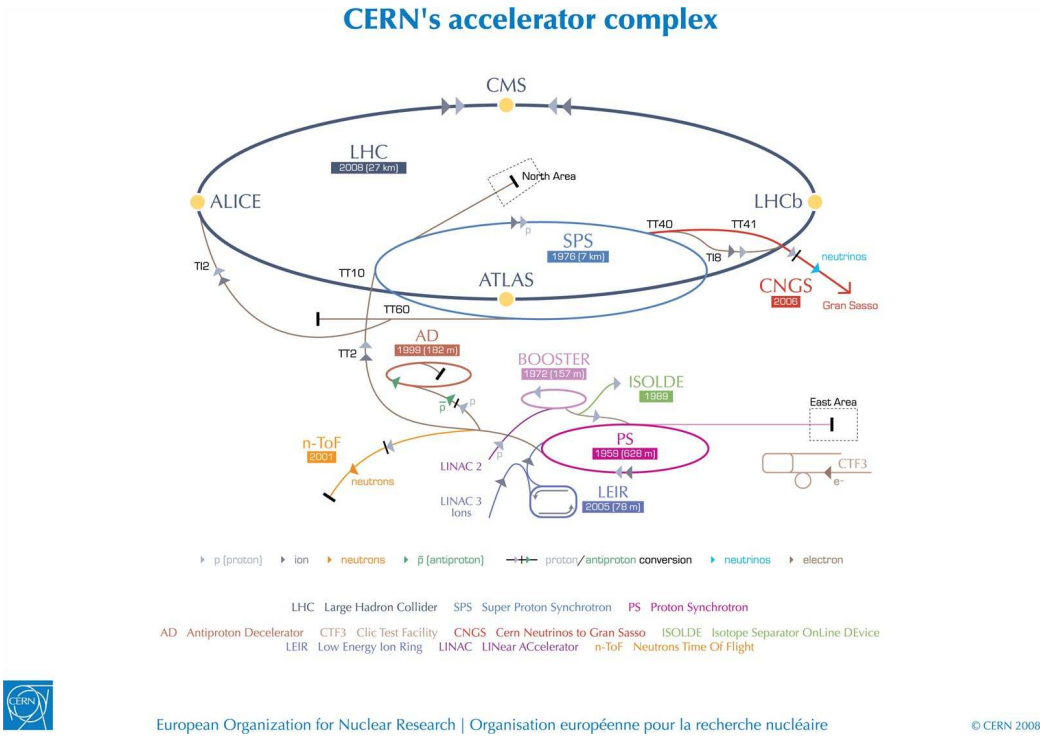

Figure 3.2 – CERN accelerator chain with the LHC at its end.

The intensity of the beam varies from a single pilot bunch with 5×10^9 protons in it, to four batches of 72 bunches with up to 1.7×10^{11} protons per bunch.

3.1.2 LHCb running conditions

Nominal running conditions of the LHC have not been reached yet. Instead, during the 2010 data-taking period, the number of bunches was far from the nominal value, with a maximum of 368 bunches inside the LHC with 344 colliding at LHCb, and with a minimum bunch spacing of 150 ns. The energy of the collisions in 2010 varied between $\sqrt{s} = 0.9$ TeV at the beginning of the

run to $\sqrt{s} = 7\,\text{TeV}$ at the end. In the 2011 data-taking period, the number of bunches was increased to 1380 with 1296 colliding at LHCb, and with a bunch spacing of 50 ns. These conditions allowed to collect at the LHCb experiment $37\,\text{pb}^{-1}$ of data in 2010 and $1.0\,\text{fb}^{-1}$ in 2011 at $\sqrt{s} = 7\,\text{TeV}$, as represented in Fig. 3.3.

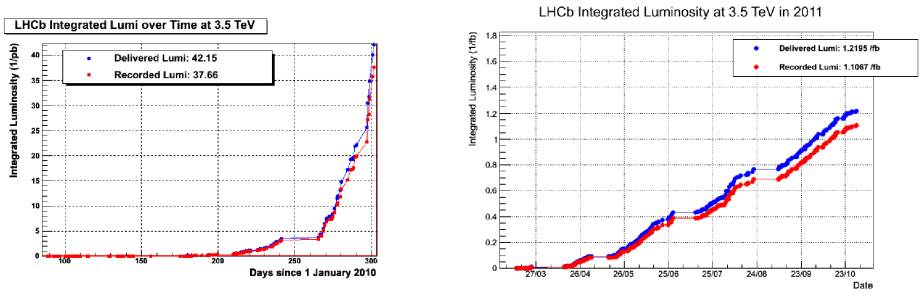

Figure 3.3 – Integrated luminosities delivered (blue) by the LHC and recorded (red) by the LHCb experiment at $\sqrt{s} = 7\,\text{TeV}$ in 2010 (left) and 2011 (right) as a function of time.

In order to give the maximum integrated luminosity to the experiments with approximately half of the nominal bunches, the machine parameters present in Eq. 3.2 were modified from their nominal values. For LHCb, the β^* was decreased from the nominal value $\beta^* = 10\,\text{m}$ to $\beta^* = 3.5\,\text{m}$. This led to an increase of three fundamental parameters related with the number of collisions produced.

- ν: the average number of interactions per bunch crossing. This includes elastic and diffractive, and at $\sqrt{s}$ =7 TeV is about 91 mb.
- μ: the average number of visible pp interactions per bunch crossing. An interaction is visible when at least two of its produced tracks are inside the detector acceptance.
- *pile-up*: the average number of pp interactions in visible events.

The design average number of visible pp interactions per bunch crossing at LHCb is $\mu \sim 0.4$, which implies that the collected data contains mainly single pp interactions. However, during the 2010 and 2011 data taking, the majority of data has been taken with $\mu \sim 1.5$, as seen in Fig. 3.4. This affects the number of pp interactions in visible events that has raised up to pile-up ~ 1.7.

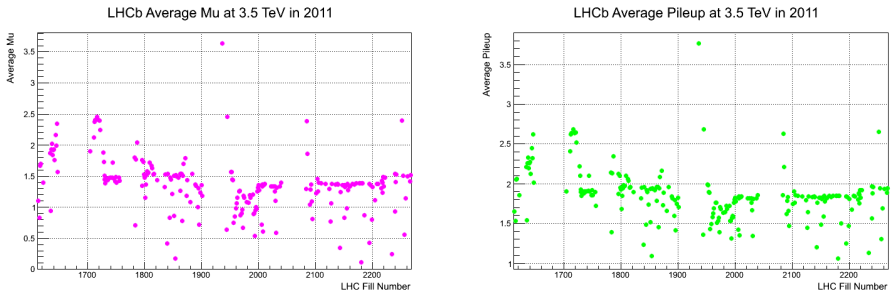

Figure 3.4 – Average number of visible interactions per bunch crossing, μ (left) and average number of pp interactions in visible events, pile-up (right) in 2011 as a function of time.

The aforementioned change of β^* also induced an increase in the instantaneous luminosity during the 2011 data taking period, which raised from the design value of $2 \times 10^{32}\,\mathrm{cm}^2 s$ to a maximum of $3.5 \times 10^{32}\,\mathrm{cm}^2 s$. This can be seen in Fig. 3.5

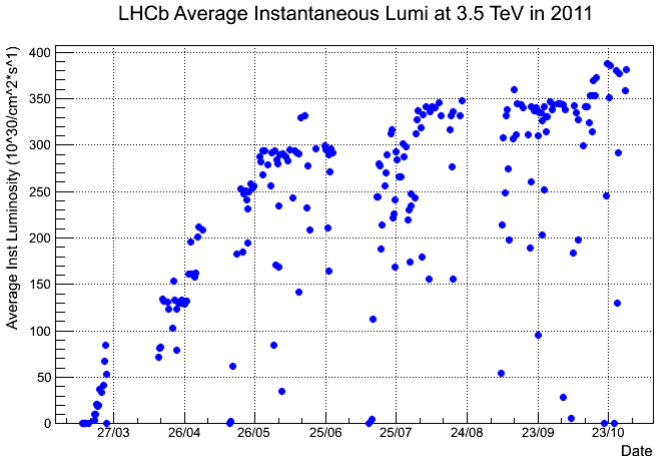

Figure 3.5 – Average instantaneous luminosity at LHCb in 2011 as a function of time.

3.2 The LHCb experiment

The LHCb experiment [36] is designed to look for indirect evidence of physics beyond the SM in CP violation and rare decays of B- and D-hadrons in pp

collisions at the LHC with a maximum centre-of-mass energy of $\sqrt{s} = 14\,\text{TeV}$. With a measured $b\bar{b}$ total cross-section of $\sim 0.5\,\text{mb}$, and a nominal luminosity of $\mathcal{L} = 2 \times 10^{32}\,\text{cm}^2/\text{s}$ [37], a total amount of the order of 10^{12} $b\bar{b}$ pairs will be produced within the LHCb acceptance per nominal year. As state in Sec. 3.1.2, during the 2011 data taking period, the running conditions were different with respect to the nominal ones. The maximum centre-of-mass energy reached by the LHC machine was $\sqrt{s} = 7\,\text{TeV}$ and the luminosity was increased up to $\mathcal{L} = 3.5 \times 10^{32}\,\text{cm}^2/\text{s}$.

LHCb is a single-arm forward spectrometer covering from approximately 10 mrad to 300 (250) mrad in the horizontal (vertical) plane. The layout of the LHCb detector is depicted in Fig. 3.6.

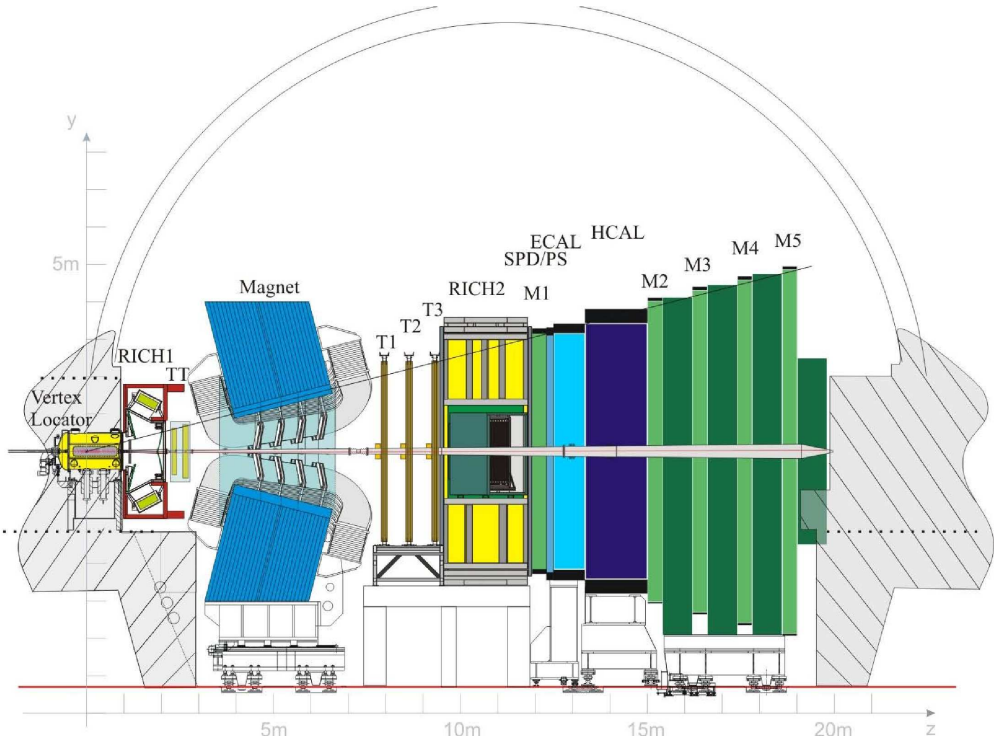

Figure 3.6 – Layout of the LHCb detector.

The choice of the shape is due to the fact that at high energies, the $b\bar{b}$ pair of quarks is produced in the same forward or backward cone, as can be seen in Fig. 3.7. The LHCb detector is composed by several sub-detectors as detailed in the following sections.

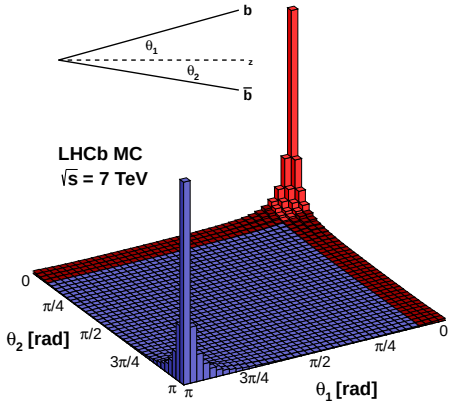

Figure 3.7 – $b\bar{b}$ pair production direction at $\sqrt{s} = 7\,\text{TeV}$.

3.2.1 Tracking system

The tracking system of the LHCb detector consists of the Vertex Locator (VELO) [38], the Tracking Turicensis (TT) [39, 40], the dipole magnet [41–43], and the T1-T3 tracking stations [44, 45]. The last ones are placed downstream the dipole magnet while the first two subsystems are upstream the dipole magnet. The main purpose of the tracking system, is the accurate measurement of the momentum and position of particles and the vertex identification.

Vertex Locator The VELO is used to identify and separate primary pp interactions from secondary vertices of $b-$ and c-hadron decays. It is made of a series of silicon modules that provide a measurement in the r and ϕ coordinates. The detector is located surrounding the interaction region, at a closest distance from the beam line of 8 mm, covering the pseudo-rapidity range of $1.6 < \eta < 4.9$. It is mounted on a movable structure that allows the opening and closure of the detector. During the injection of the beam —to avoid radiation damage on the detector— the VELO remains opened, and only when the beam conditions are stable it goes to its final position. Figure 3.8 shows the overview of the VELO detector. The VELO system contains four modules that are located upstream of the primary vertex. They are used for the *pile-up veto system* [46]. The pile-up measurement is used to veto events with a large number of primary vertices.

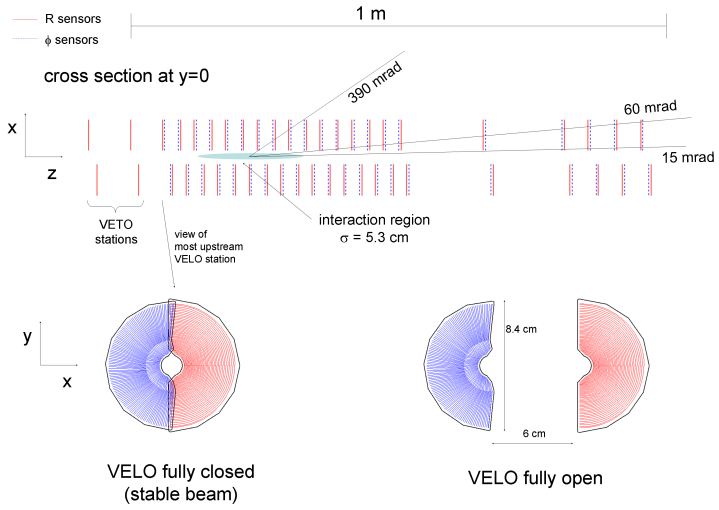

Figure 3.8 – VELO overview with the pile-up system. The appearance of the modules when opened and closed is also showed.

Tracking Turicensis The TT is located upstream of the dipole magnet, and it covers the full acceptance of the detector. The TT is made of silicon micro-strip sensors arranged into four stations. The four detector stations are grouped in two pairs (x, u) and (v, x), separated by approximately 30 cm along the beam axis. The first and last layers contain vertical strips and the second and third contain strips rotated by a stereo angle of $-5°$ and $+5°$, respectively. The layout of the full TT sub-detector is shown in Fig. 3.9.

Dipole magnet The LHCb experiment uses a dipole magnet to measure the momentum of charged particles. The saddle-shaped coils are warm to reduce costs and construction time. The vertical field induces a deflection of the particles in the horizontal plane. The magnet polarity is flipped regularly from the *up* to the *down* configuration to reduce any systematic effect produced by the magnetic field. The integrated magnetic field is of 4 Tm for tracks originating near the primary interaction point.

T1-T3 stations The T1-T3 stations (or T stations), located downstream the dipole magnet, are segmented into two regions, the Inner Tracker (IT) and the Outer Tracker (OT). While the IT uses the same silicon micro-strip sensors as the TT, the OT is made out of drift-tubes. The IT covers a 120 cm wide and 40 cm high cross-shaped region in the centre of the three tracking

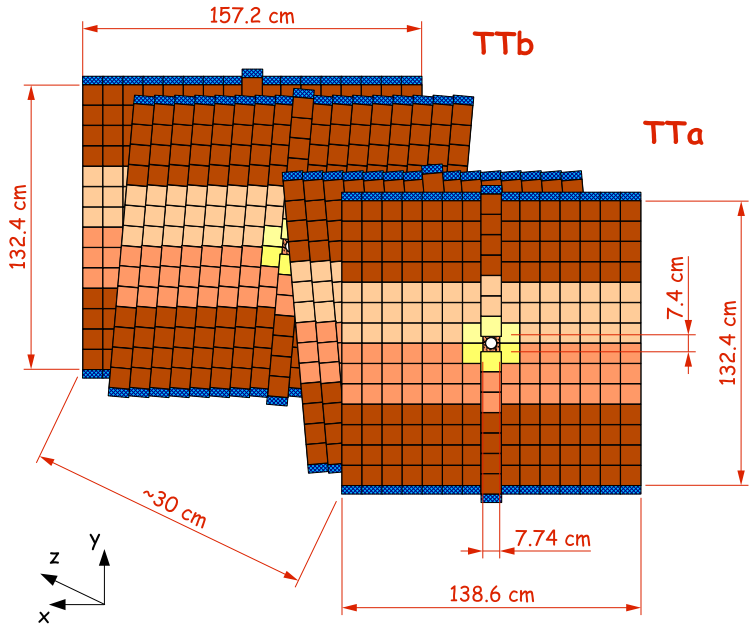

Figure 3.9 – Layout of the four stations of the TT sub-detector.

stations. Both systems consist of three detector stations made out of four layers in an $(x-u-v-x)$ arrangement following the same structure as the TT. The layout of one of the IT detection layers is illustrated in Fig. 3.10.

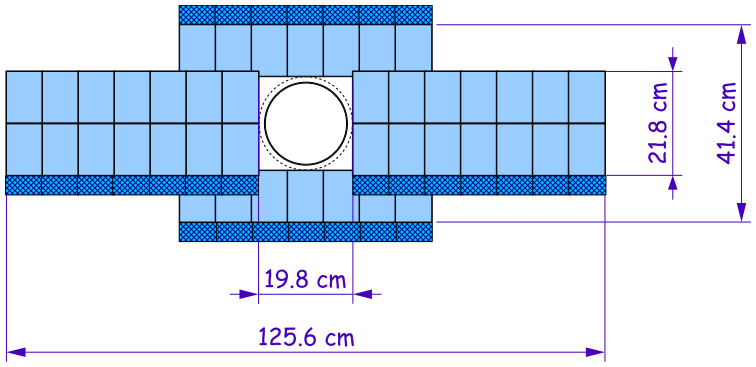

Figure 3.10 – Layout of a $x-$detection layer of the second station of the IT sub-detector.

The OT is a drift-time detector used for tracking of charged particles and for measuring their momentum over a large acceptance area. Each of

the twelve layers consist of two staggered monolayers of drift-tubes. The counting gas is a mixture of Argon (70%) and CO_2 (30%) which provides a fast drift-time below 50 ns and a drift-coordinate resolution of 200 µm. A layout of the OT, IT and TT system is shown in Fig. 3.11.

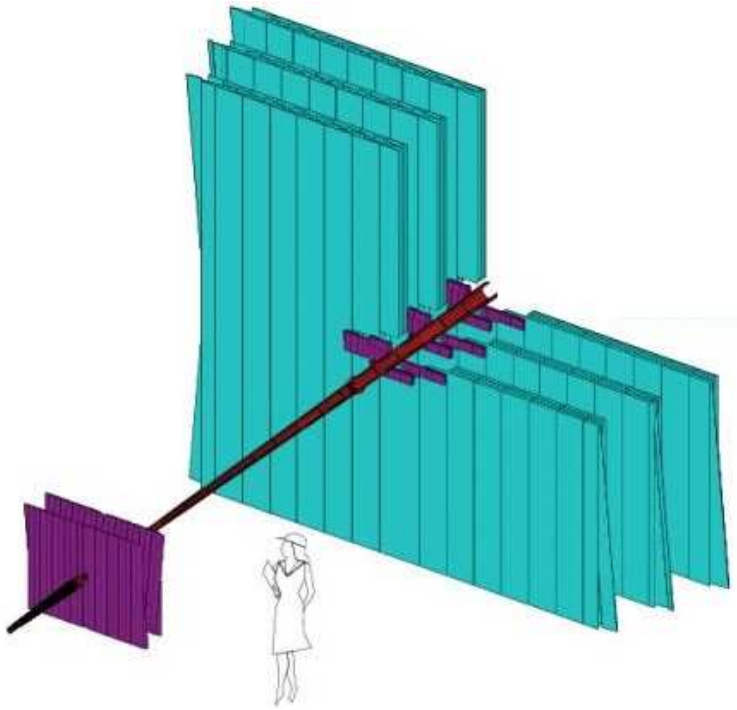

Figure 3.11 – Arrangement of the OT stations (blue). The IT and TT (purple) are also represented.

3.2.2 Ring Imaging Cherenkov detectors

The study of B- and D-hadron decays requires a precise identification of kaons and pions. Particle identification (PID) of hadrons at LHCb is performed through two Ring Imaging Cherenkov Detectors (RICH), known as RICH1 and RICH2, covering a wide momentum range.

RICH1 The RICH1 detector [39,47] is placed upstream the dipole magnet and covers the low momentum range of particles $[1-60]$ GeV/c, using aerogel and C_4F_{10} as radiators. It provides a measurement for particles in the full LHCb acceptance.

RICH2 The RICH2 detector [48,49] is placed downstream the dipole magnet covering the particle-momentum range from 15 GeV/c to 100 GeV/c, and it uses CF_4 as radiator. The RICH2 acceptance is ±120 mrad in the horizontal plane and ±100 mrad in the vertical plane.

The Cherenkov light produced by particles traversing RICH1 or RICH2 is deflected, through a system of spherical and flat mirrors, to Hybrid Photo Detector (HPD) photo-cathodes. Figure 3.12 shows the layout of the two RICH detectors.

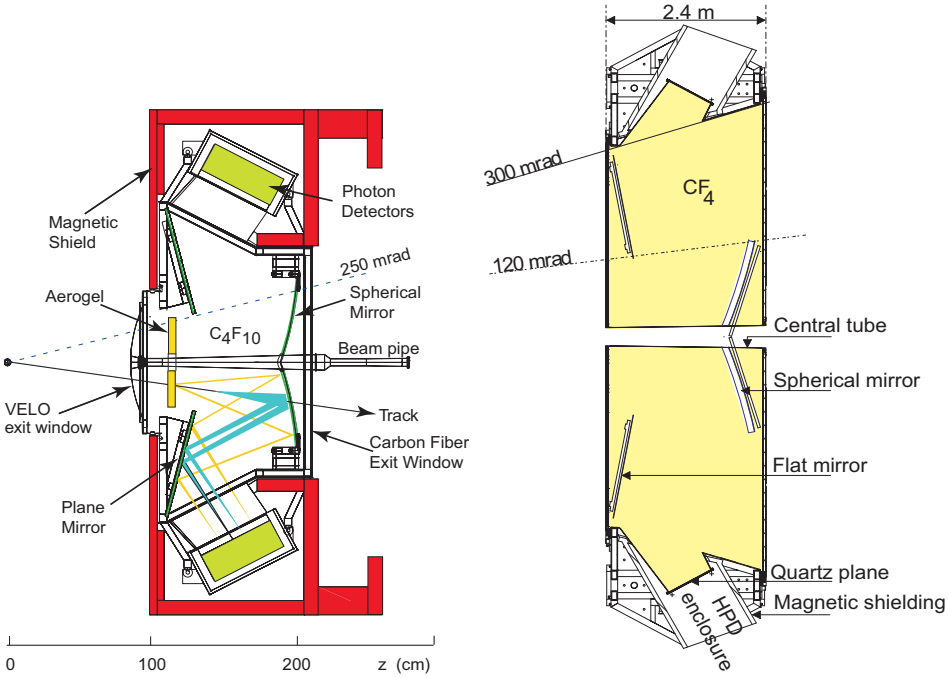

Figure 3.12 – Layout of the RICH1 (left) and RICH2 (right) detectors.

3.2.3 Calorimeter system

The LHCb calorimeter system [50] consists of four different sub-detectors. The Scintillator Pad Detector (SPD) and the Pre-Shower Detector (PS) — which are interleaved by a plane of lead— followed by the electromagnetic calorimeter (ECAL) and the hadronic calorimeter (HCAL). The role of the LHCb calorimeter is multiple, and it is used to

- select high transverse energy (E_T) hadron, electron and photon candidates for the first level of the trigger.

- provide the identification of electrons, photons and hadrons.
- measure the energy of electron and photon candidates and the position of photons.

The lateral segmentation of the four sub-detectors is variable, as the occupancy varies up to two orders of magnitude over the sub-detector surface. The SPD, PS and ECAL sub-detectors are segmented projectively into three different regions, while the HCAL is segmented into two regions. Figure 3.13 shows the lateral segmentation of the calorimeter.

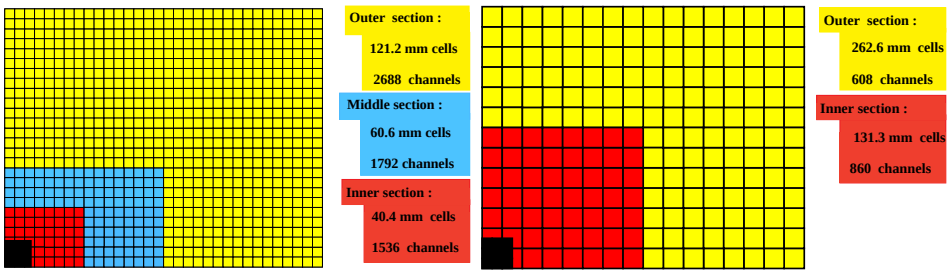

Figure 3.13 – Lateral segmentation of the SPD/PS and ECAL (left) and the HCAL (right). One quarter of the detector front face is shown.

Scintillator Pad Detector and Pre-Shower detector

The SPD and PS are composed by 6016 scintillating plastic cells with a depth of 1.5 cm. The two scintillating planes are interleaved by a lead plane with a thickness of $2.5X_0$. As the occupancy decreases away from the beam pipe, the detectors are divided into three regions: inner, middle and outer, with different cell sizes that are roughly 4×4, 6×6 and $12 \times 12\,\mathrm{cm}^2$, respectively. The projective geometry makes that the cell size of the SPD is smaller by 0.45% with respect to the PS. The light from the cells is transmitted by wave-length shifting (WLS) fibres, and then clear fibres take the light to 64-channel Multi-Anode Phototubes (MAPMT) [51]. Each of the hundred SPD or PS very-front-end (VFE) cards deals with the signal from the 64 channels of a single MAPMT.

In the case of the SPD, the VFE card integrates the signal in the $25\,ns$ window defined by the LHC bunch crossing rate. Afterwards, it performs a binary discrimination with a threshold placed at a certain fraction of the energy left by minimum ionizing particles (E_{MIP}) [52]. This threshold is set to $0.5\,E_{\mathrm{MIP}}$ for the 2010 and 2011 data taking. The resulting bit is used to tag the trigger candidates as electrons or photons, and the sum of bits

determines the charged-track multiplicity of the event. Due to the binary output of the detector, scanning the threshold value is required to calibrate the detector and the electronics response to particles traversing the cells. As the calibration procedure of the SPD detector is one of the goals of this thesis, it is described in detail in Chapter 4.

One of the SPD functions is the classification of electromagnetic objects as electrons or photons at the first level of trigger (L0) [53] where tracking information is not available. The SPD-hit multiplicity is also used by the L0 decision unit, both for vetoing events with high charged-particle multiplicity and for requiring some activity as a minimum bias trigger. The SPD is used in the offline reconstruction to identify photon and electron candidates, which are required by some key physics channels [54], [55]. Other functions of the SPD are the monitoring of instantaneous luminosity [56] and the separation of converted and non-converted photons for offline energy correction. To perform all of these tasks, the SPD cells need to be perfectly calibrated.

The PS provides an accurate separation between electrons and charged pions with rejection factors of 99.6%, 99.6% and 99.7% with electron retention of 91%, 92% and 97% for 10, 20 and 50 GeV/c of particle momentum, respectively [57].

Electromagnetic Calorimeter

The ECAL is placed at 12.5 m downstream of the interaction region with a segmentation that matches that of the SPD and PS. The outer acceptance arrives up to 300 mrad and 250 mrad in the bending and non-bending plane, respectively, while the inner acceptance is limited to $\theta_{x,y} > 25$ mrad due to high radiation dose levels. The total depth of the ECAL corresponds to $25X_0$. The ECAL is composed by a shashlik structure of 66 layers of 2 mm-lead/4 mm-scintillator which is readout by WLS fibres. The design energy resolution is given by

$$\frac{\sigma_E}{E} = \frac{10\%}{\sqrt{E}} \oplus 1\%\,, \tag{3.4}$$

with the energy in GeV, where the first term refers to the stochastic term, and the second to the constant term. This resolution was measured on a test beam [58] yielding as result that the stochastic term is $8.5\% < s < 9.5\%$ and the constant $c \sim 0.8\%$, depending on the region and the test beam conditions. The results of the test for an outer module is given in Fig. 3.14.

The ECAL plays an essential role in determining the energy of γ and π^0, and in the mass resolution of decays such as $B^0 \to K^{*0}\gamma$.

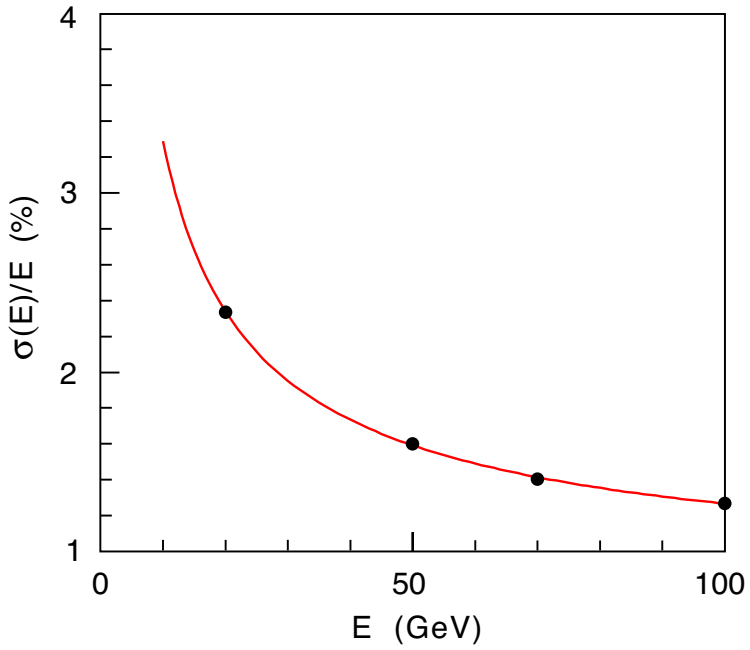

Figure 3.14 – ECAL energy resolution of the measured with electrons over a surface of ($\pm 15\,\text{mm}, \pm 30\,\text{mm}$) in an outer module.

Hadronic Calorimeter

The HCAL is a sampling calorimeter made from iron as absorber and scintillating tiles as active material, that run parallel to the beam axis. The light is collected by WLS running along the detector towards the back side where the photomultiplier tubes are placed. The transverse segmentation of the HCAL is different from the rest of the calorimeter [59]. It has an inner region with cells of $131.3 \times 131.3\,\text{mm}^2$ and an outer region with cells of $262.6 \times 262.6\,\text{mm}^2$. The depth of the HCAL is $5.6\lambda_{int}$ that are added to the $1.2\lambda_{int}$ from the upstream ECAL. Figure 3.16 shows the energy resolution of the HCAL extracted from the test bench [58], which has been found to be

$$\frac{\sigma_E}{E} = \frac{69 \pm 5\%}{\sqrt{E}} \oplus (9 \pm 2)\%\,, \tag{3.5}$$

where the energy is measured in GeV. The main use of the HCAL is to select high transverse energy hadron candidates for the first trigger level.

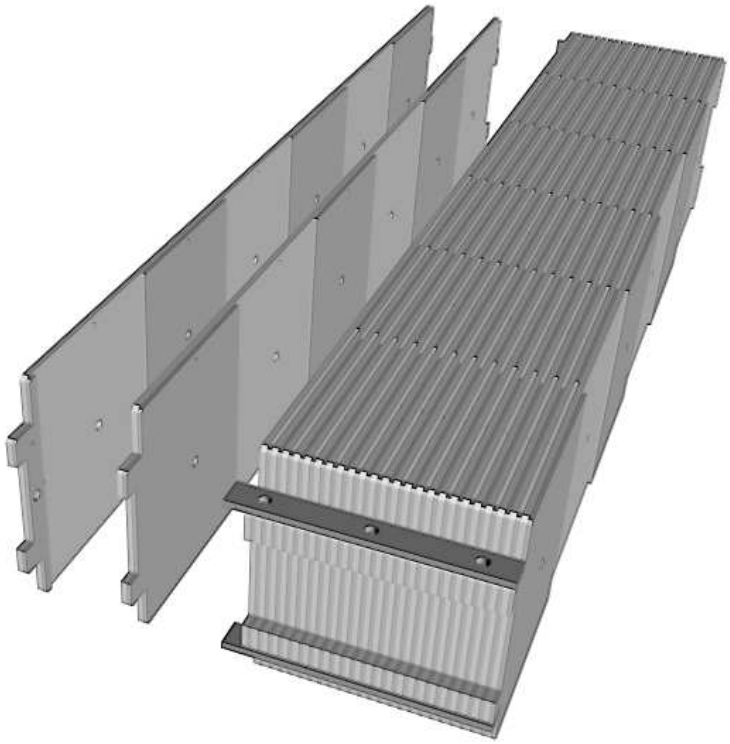

Figure 3.15 – View of an HCAL module.

3.2.4 Muon system

The LHCb physics program requires an excellent trigger and identification of muon candidates as they are present in many final states of B and D decays. The LHCb muon system [60–62] is composed by five stations (M1-M5) with an outer angular acceptance of ± 306 mrad and ± 258 mrad for the bending and non-bending plane, respectively. The inner angular acceptance is ± 20 mrad for the bending plane and ± 16 mrad for the non-bending plane. The stations M2-M5 are placed downstream the entire calorimeter system, while M1 is placed in front of the calorimeter and it is used to improve the measurement of the muon transverse momentum at the trigger level. The minimum momentum required for a muon to traverse the five stations is around 6 GeV/c. The geometry of the five stations is projective and they are segmented laterally into four regions (R1−R4) with increasing pad size that scale in the ratio 1:2:4:8 for R1:R2:R3:R4. The stations M2-M5 are interleaved with 80 cm of iron to select highly penetrating muons. The total absorber, including the calorimeters, is approximately $20\lambda_{int}$. A total of 1380

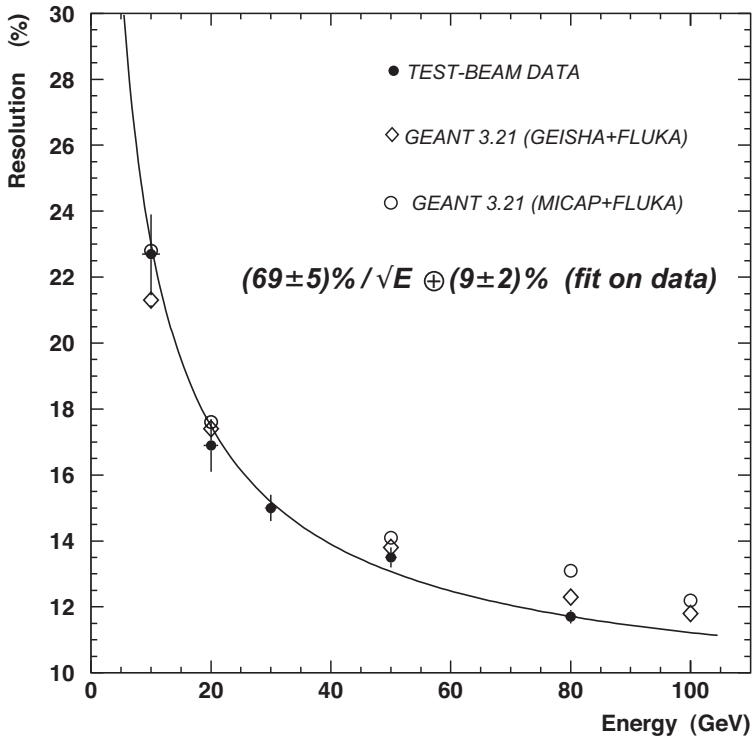

Figure 3.16 – HCAL energy resolution for data (full points) and simulation (open points) with three different hadronic simulation codes. The fit to the data is represented as a line.

Multi Wire Proportional Chambers (MWPC) are used for all the regions except the innermost region of M1, where triple-GEM detectors are used due to the high particle flux. Figure 3.17 shows the muon system overview and Fig. 3.18 shows the lateral segmentation of the muon chambers.

3.3 The Trigger system

The LHCb trigger system [39, 53] is composed by two different levels that reduces the initial 40 MHz interaction rate to a final 2 kHz rate, that has been increased to 3 kHz during the 2011 data taking period. These levels are the first trigger level (L0) and the high level trigger (HLT). The L0 is implemented in custom electronics and operates synchronously with the LHC bunch-crossing frequency of 40 MHz. Its purpose is to reduce the actual rate of visible pp collisions from $10-15$ MHz to 1.1 MHz, at which the entire detector can be readout. The HLT is executed asynchronously on a processor

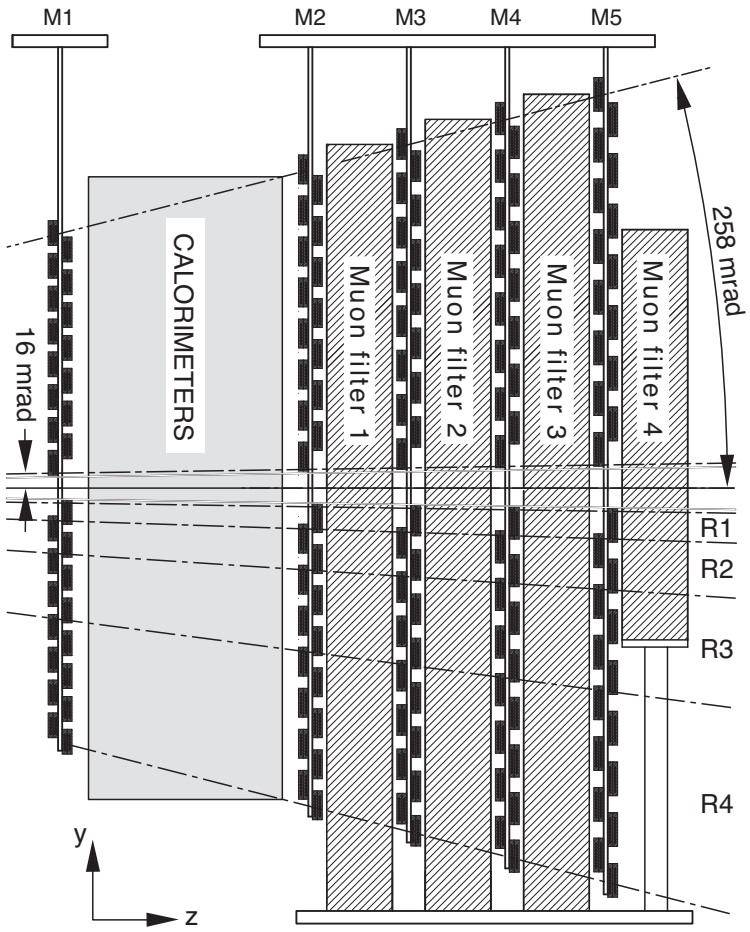

Figure 3.17 – Overview of the muon system.

farm. The HLT is divided into two consecutive stages, known as HLT1 and HLT2. In the HLT1 stage, a partial event reconstruction is executed where high transverse momentum (p_T) and high impact parameter (IP) candidates are selected, reducing the rate to 50 kHz. After this, the rate is low enough so the HLT2 can perform the full reconstruction of the event to further reduce the rate to the final 3 kHz that will be saved to disk for offline analysis. A schematic overview of the complete LHCb trigger chain is represented in Fig. 3.19. To ensure that during offline analysis the trigger conditions are known, the combination of trigger algorithms with their selection parameters will be assigned a unique key, the Trigger Configuration Key (TCK).

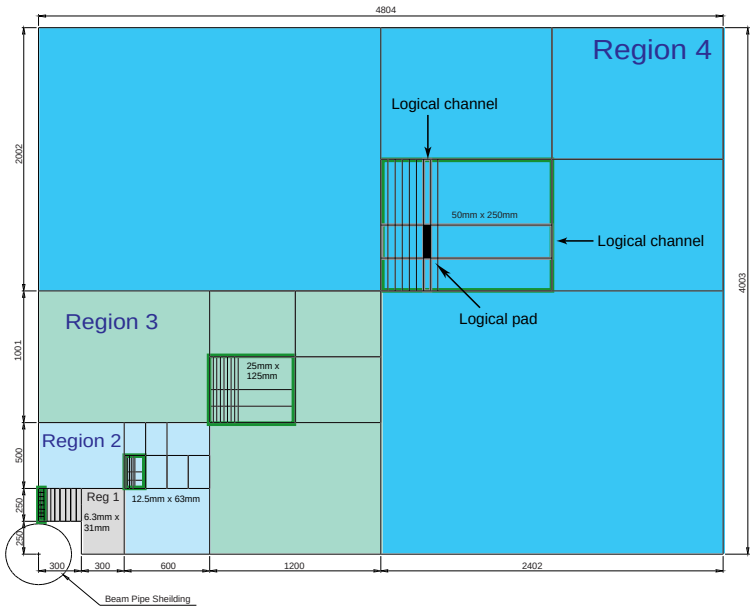

Figure 3.18 – Front view of one quadrant on a muon station showing the partitioning into sectors. Horizontal and vertical strips are represented in each sector, with their intersection representing a logical pad.

3.3.1 Level-0 trigger

The L0 is divided into three components, the pile-up system, the Level-0 calorimeter trigger and the Level-0 muon trigger. The pile-up system distinguishes between crossings with single and crossings with multiple visible interactions. It consists of two planes perpendicular to the beam line and located upstream of the VELO. Each plane is made out of two overlapping VELO R-sensors. It provides the position of the primary vertices along the beam axis and the total backward charged-track multiplicity. The calorimeter trigger looks for the highest-E_T hadron, electron, photon or neutral pion candidates. It reconstructs 2×2 clusters and selects the one with largest E_T. The total number of SPD hits is counted to provide a measurement of the total charged-track multiplicity of the event. A cut in the SPD charged-track multiplicity of 600 has been used to veto events with a large number of primary vertices. In Fig. 3.20, the multiplicity for events with 1, 2, 3, 4 or 5 primary interactions is shown, and one can see that by requiring less than 600 SPD hits, a large fraction of events with more than one primary collision are removed, while the efficiency of selecting events with a single primary interaction is $\sim 100\,\%$.

The muon trigger selects the two muons with highest p_T for each quad-

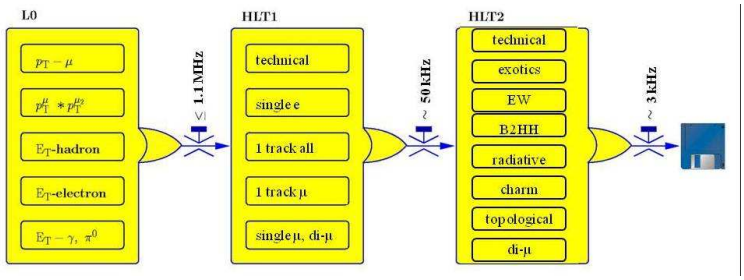

Figure 3.19 – Schematic overview of the complete LHCb trigger chain.

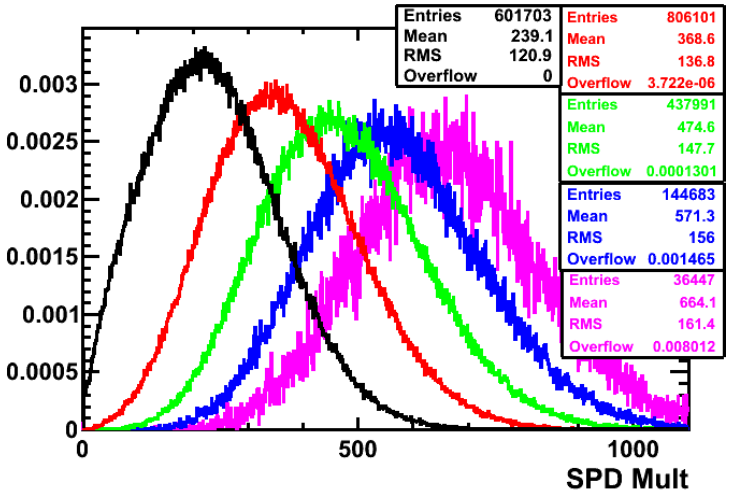

Figure 3.20 – SPD charged-track multiplicity for events with 1 (black), 2 (red), 3 (green), 4 (blue) or 5 (magenta) primary interactions. A requirement of SPD < 600, that removes a large fraction of events with several primary interactions, is implemented in the trigger.

rant of the muon detector. The standalone muon reconstruction allows a resolution of 20% on the p_T of muons.

3.3.2 High level trigger

The HLT is the second and last level of the LHCb trigger, and runs over events that have passed the L0 trigger. It is a software application running on the Event Filter Farm (EFF) composed by 1000 multi-core computing nodes. Each application has access to the complete event data and rejects the bulk of uninteresting events to a final rate of 3 kHz. As full event reconstruction is

not possible at the output rate of the L0, the HLT is divided into two stages, namely HLT1 and HLT2.

HLT1 It reduces the L0 output rate of 1.1 MHz to ∼50 kHz. Its main purpose is to have a performance independent of the varying running conditions during data taking. It is based on the selection of at least a single track with good quality, high momentum and large IP with respect to all primary vertices in the event. Besides, there are selections of lifetime unbiased muons or electrons based around the confirmation of L0 muon segments or L0 calorimeter clusters, respectively. The selection efficiency of signal events is more than 80% for most of the LHCb benchmark channels. The events selected by the HLT1 pass to the HLT2 stage.

HLT2 At the HLT2, the input rate is small enough to allow a full reconstruction of the events. A search for secondary vertices coming from B and D decays is done. Global Event Cuts (GEC), such as the charged-track multiplicity, can be used to reject complex events that require an excessive amount of time to be reconstructed. The HLT2 is composed by a mixture of inclusive and exclusive lines. The first ones search for generic features of B and D decays, while the second ones select specific characteristics of particular decays. Its output rate of $\sim$ 3 kHz is low enough so that offline event processing can be done.

3.4 The Online and Offline system

3.4.1 The online system

The LHCb online system [63,64] guarantees the correct transfer of data from the front-end electronics to the permanent storage. It is divided into three systems: The data acquisition (DAQ), the timing and fast control (TFC) and the experiment control (ECS).

DAQ Transports the data belonging to a given bunch crossing and identified by the trigger, from the front-end electronics to the permanent storage.

TFC Drives all the stages of the data readout of the LHCb detector between the front-end electronics and the EFF by distributing the beam-synchronous clock, the L0 trigger, synchronous resets and fast control commands.

ECS Ensures the control and monitoring of the operational state of the entire LHCb detector. It includes high and low voltages, temperatures, gas flows and pressures, and trigger, TFC and DAQ monitoring.

3.4.2 The offline system

The LHCb offline system [65] takes care of the replication of raw data, either coming from the detector or simulated, as well as the full event reconstruction. The LHCb computing model is based on a distributed multi-tier regional centre model with CERN as Tier-0, and six additional Tier-1 centres and a number of Tier-2 centres. The six Tier-1 centres are CNAF (Italy), GRIDKA (Germany), IN2P3 (France), NIKHEF/SARA (The Netherlands), PIC (Spain) and RAL (United Kingdom). CERN also takes the role of a Tier-1. The over one hundred Tier-2 centres are mainly devoted to the production of simulated events. The raw data coming from the detector are transferred to the CERN storage element and copies are distributed among the six Tier-1. Afterwards, the reconstruction of the entire event to form physical quantities is performed in the Tier-1s. The reconstructed events are saved in a Stripping Data Summary Tape (SDST) file and will be further filtered for physical analyses. This process, known as Stripping, produces as output a Data Summary Tape (DST) which will be available for physics analysis.

3.5 Detector performance

In the coming sections, a quantitative approach to the performance of the detector with 2011 data will be given, in three crucial aspects for performing B-physics studies: tracking, vertexing and particle identification.

3.5.1 Track reconstruction

The LHCb track reconstruction uses hits from the VELO, TT, IT and OT to create tracks [39]. They are divided into five categories that can be seen in Fig. 3.21.

Long tracks Traverse the full tracking system from the VELO to the T stations. Their momentum resolution is the most accurate, and then are the most relevant for studying b- and c-hadron decays.

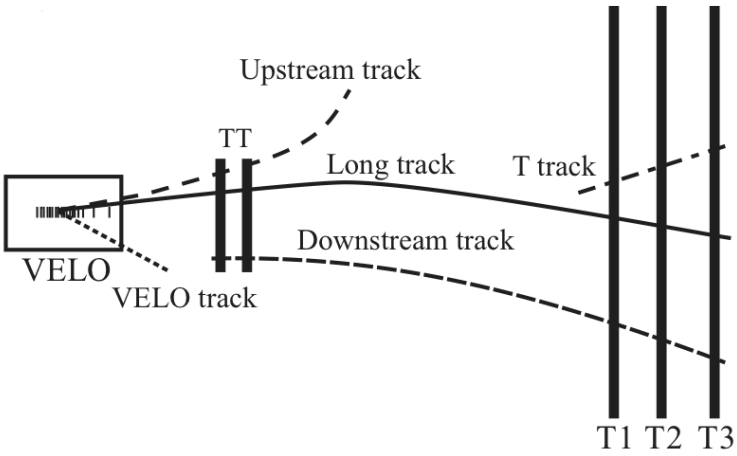

Figure 3.21 – Schematic illustration of the five different track types in LHCb: long, upstream, downstream, VELO and T tracks.

Upstream tracks Traverse only the VELO and TT. Typically, they are low-momentum tracks that are bent out of the detector acceptance by the magnet.

Downstream tracks Traverse only the TT and T stations. The most relevant cases are decay products of long-living particles as K^0_S or Λ that decay outside the acceptance of the VELO detector.

VELO tracks Measured only in the VELO. In most cases, they are large angle or backward tracks useful for the reconstruction of the primary vertex.

T tracks They are only measured in the T stations. They are the result of secondary interactions of particles with the detector material.

The track reconstruction sequence starts with the search for track seeds in the VELO and T stations where the magnetic field is low. After tracks have been found their trajectory is refitted including multiple scattering effects and $\mathrm{d}E/\mathrm{d}x$ energy loss. The momentum resolution of tracks goes from $\mathrm{d}p/p = 0.4\%$ for tracks with $p_T = 5\,\mathrm{GeV}/c$ to $\mathrm{d}p/p = 0.6\%$ for tracks with $p_T = 100\,\mathrm{GeV}/c$. This is translated into a mass resolution of $\sim 22\,\mathrm{MeV}/c^2$ around the B-meson mass for two-body B decays as can be seen in Fig. 3.22.

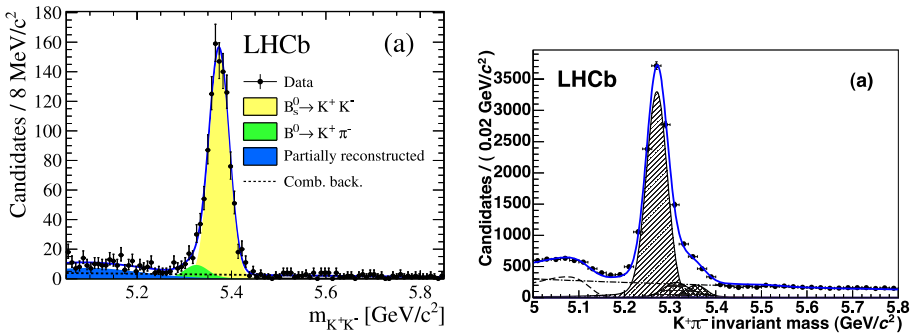

Figure 3.22 – Invariant-mass distribution of KK [66] and $K\pi$ [67] pairs. The mass resolution is $\sim 22\,\mathrm{MeV}/c^2$ for both cases.

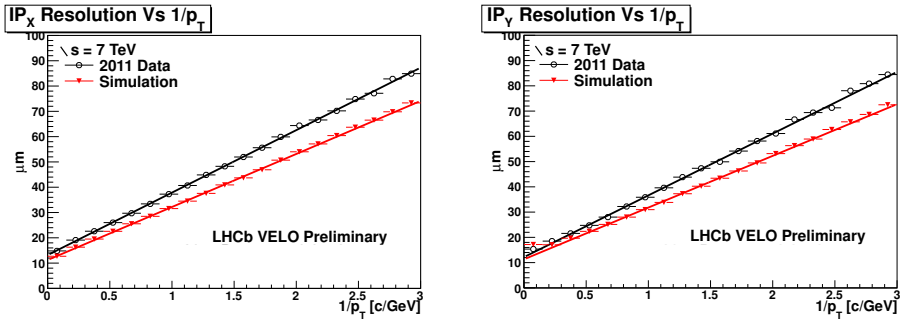

Figure 3.23 – Impact parameter resolution for x (left) and y (right) coordinates as a function of $1/p_T$. The black points are the 2011 minimum bias data and the red points are the simulated data. Events with only one reconstructed PV are considered.

3.5.2 Vertex reconstruction

A distinctive feature of particles coming from B and D decays, is that they have a large IP with respect to the primary interaction. Hence, a good resolution in the position of the primary vertex, as well as in the IP are needed to distinguish uniquely particles coming from the primary or the secondary vertices. The IP resolution achieved by the tracking system is shown in Fig. 3.23 with the comparison between real data and simulation.

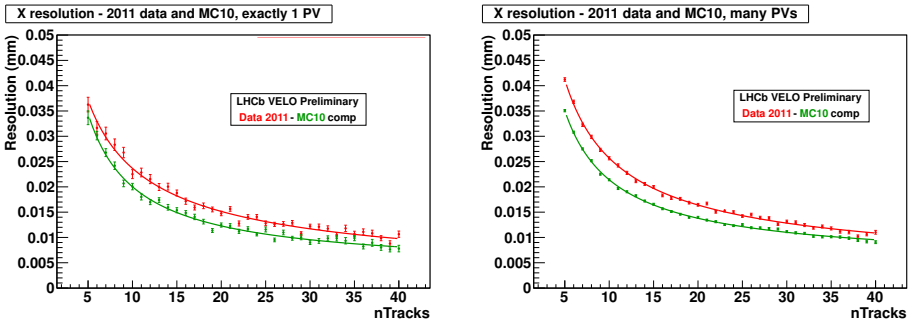

Figure 3.24 – Vertex resolution in x coordinate for events with only one PV (left) and for events with more than one PV (right) as a function of the number of tracks reconstructed in the vertex. The plots depict 2011 data in red and simulation data in green.

The dependence of the IP resolution on $1/p_T$ can be parametrised as

$$\begin{aligned} \sigma_x^{\text{data}} &= 13.2 \pm 24.7/p_T \,\mu\text{m} \\ \sigma_x^{\text{MC}} &= 11.2 \pm 21.0/p_T \,\mu\text{m} \\ \sigma_y^{\text{data}} &= 12.2 \pm 24.4/p_T \,\mu\text{m} \\ \sigma_y^{\text{MC}} &= 11.3 \pm 20.5/p_T \,\mu\text{m}\,. \end{aligned} \tag{3.6}$$

Notice that real data has a $\sim$ 10% worst resolution than simulation. This can be due to the larger number of tracks present in data than in the simulation, that complicates the reconstruction of the event. The resolutions of the vertex position in x, y and z coordinates are shown in Figs. 3.24-3.26, comparing events with only one PV and with more than one PV [68].

As expected, the resolution on the PV position worsens with the presence of more than one primary interactions between $(20-30)\%$, depending on the number of tracks used to reconstruct the vertex.

3.5.3 Particle identification

The identification of charged particles requires the combined information of the RICH, SPD, PS, ECAL and muon sub-detectors. Photons and neutral pions are identified using the calorimeter.

Hadron identification Rings in the RICH detectors are reconstructed, and a likelihood function is maximised by varying the particle hypothesis of each track through electron, muon, pion, kaon and proton. The likelihood considers all the tracks in the event, as well as the information of the three

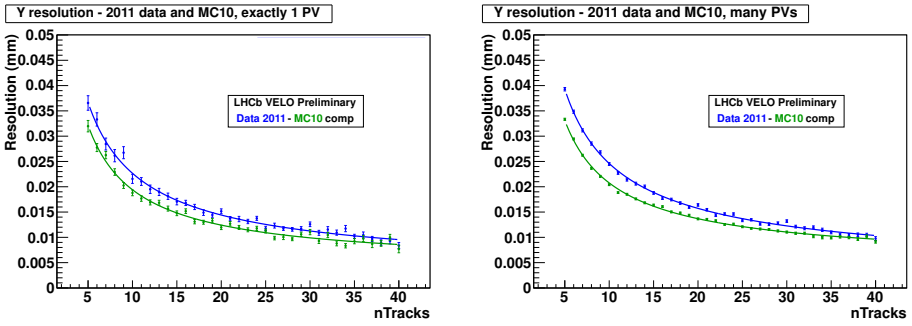

Figure 3.25 – Vertex resolution in y coordinate for events with only one PV (left) and for events with more than one PV (right) as a function of the number of tracks reconstructed in the vertex. The plots depict 2011 data in blue and simulation data in green.

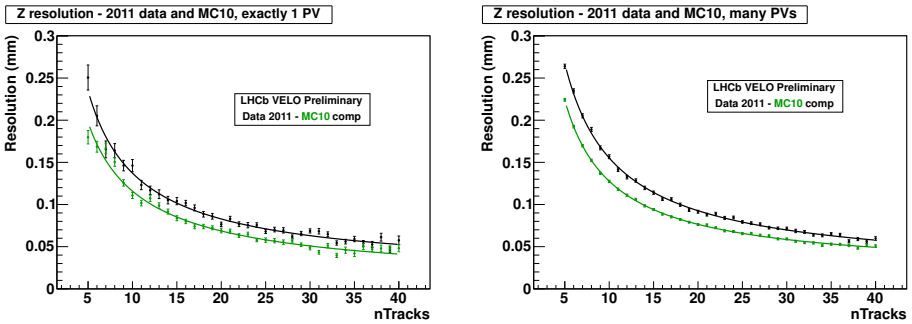

Figure 3.26 – Vertex resolution in z coordinate for events with only one PV (left) and for events with more than one PV (right) as a function of the number of tracks reconstructed in the vertex. The plots depict 2011 data in black and simulation data in green.

radiators simultaneously. The output of the process is a best hypothesis for each track. The Cherenkov angle as a function of the particle momenta for different particle types and the three different RICH radiators is shown in Fig. 3.27, where the ring reconstruction of a simulated event in the RICH1 detector is also represented.

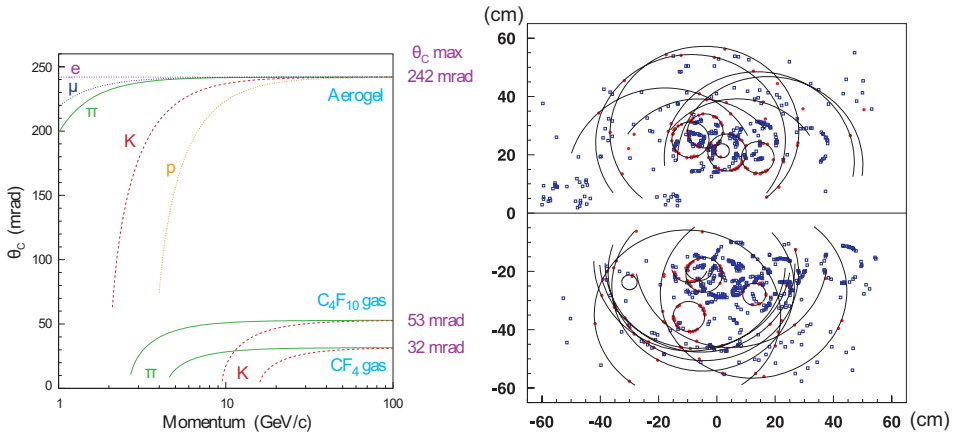

Figure 3.27 – Cherenkov angle θ_c as a function of particle momenta for the three different RICH radiators and different particle types (left), and ring reconstruction in the RICH1 detector of a simulated event.

The average efficiency for kaon identification is $\epsilon(K \to K) \sim 95\%$ for momenta in the range $[2 - 100]\,\text{GeV}/c$. The corresponding pion misidentification rate is $\epsilon(\pi \to K) \sim 5\%$. Figure 3.28 shows the good agreement of the PID performance between 2011 data and simulation [69].

Electron identification Electrons are identified using mainly the balance of the track momentum and the energy cluster in the ECAL, and the matching between the barycentre of the cluster and the track extrapolation. The energy of bremsstrahlung photons emitted by the electrons before the magnet is also used as a discriminant variable as well as the energy deposition in the PS and HCAL. This information is combined with the RICH and muon system to build a likelihood. Using $B^+ \to J/\psi\, K^+$ decays where $J/\psi \to e^+e^-$, the average electron identification efficiency has been measured to be $\sim 93\%$ with a pion mis-identification fraction of $\sim 1\%$ [70]. Figure 3.29 represents the electron E/p using 2011 data [71].

Photon and π^0 identification Electromagnetic clusters without a track associated to them are identified as photons. In order to do that, the re-

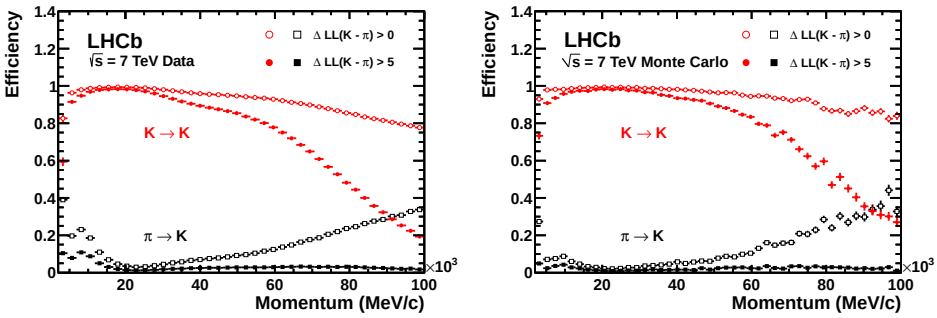

Figure 3.28 – Kaon identification and pion misidentification performance for 2011 data (left) and simulation (right). Two different values of the likelihood for the particle hypothesis are considered.

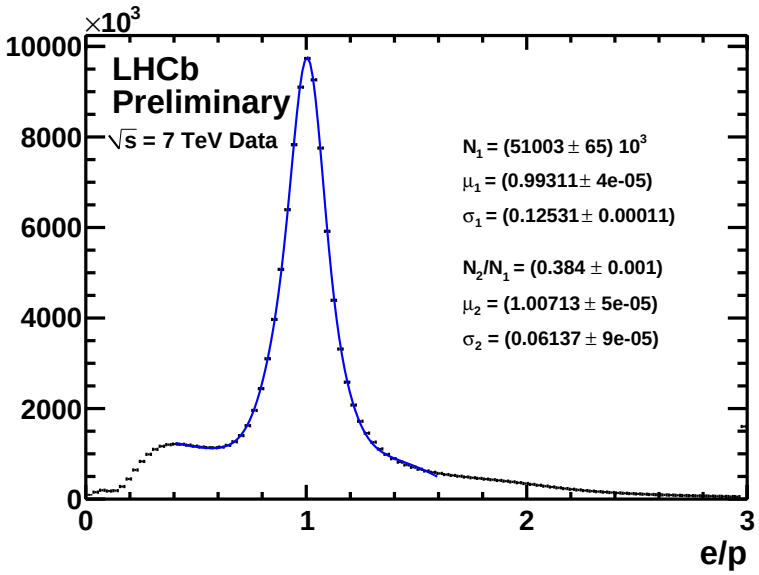

Figure 3.29 – E/p for electrons using 2011 pp collision data.

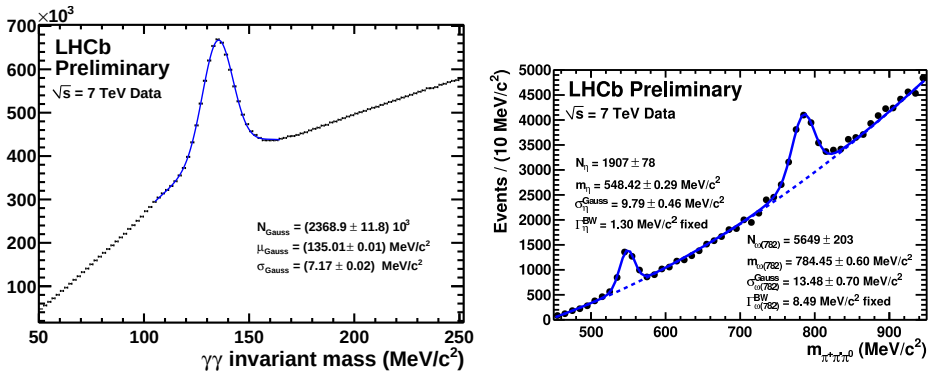

Figure 3.30 – Invariant-mass distribution of the di-photon pairs (left) and $\pi^+\pi^-\pi^0$ (right)

constructed tracks are extrapolated to the ECAL plane and a χ^2_γ estimator is built. A candidate is assigned to be a photon when $\chi^2_\gamma > 4$. Photons converted after the magnet are identified requiring a SPD hit in the cell in front of the centre of the ECAL cluster [72].

Neutral pions are reconstructed as a pair of photons when the pion transverse energy is below $\sim 2\,\text{GeV}$. Above this threshold, the two photons appear as a single cluster in the calorimeter, these pions are called merged π^0. The shape of the ECAL cluster is used to build a discriminant variable to distinguish between a single photon and a merged π^0. With photons from $B^0 \to K^{*0}\gamma$ and merged π^0 from minimum bias events, the efficiency in selecting photons is $\sim 90\%$ with a merged-π^0 rejection of 60%. The invariant mass of photon pairs, alone and in combination with a $\pi^+\pi^-$ pair, can be seen in Fig. 3.30 [71].

Muon identification Only muons with $p > 3\,\text{GeV}/c$ arrive into the muon chambers, as below this threshold they do not have enough energy to reach the muon system. A field of interest (FOI) region around the track extrapolation in the muon plane is defined, and hits are looked for inside the FOI. A track is considered as a muon candidate when a minimum number of stations —that depends on the momentum of the candidate— have hits in the corresponding FOI.

Using a sample of $J/\psi \to \mu^+\mu^-$, the muon identification efficiency was measured to be $\epsilon(\mu \to \mu) \sim 98\%$ with a corresponding pion misidentification of $\epsilon(\pi \to \mu) < 0.6\%$. This efficiency is a flat function of the momentum above $10\,\text{GeV}/c$ [73].

The excellent performance of the muon identification can be seen on the

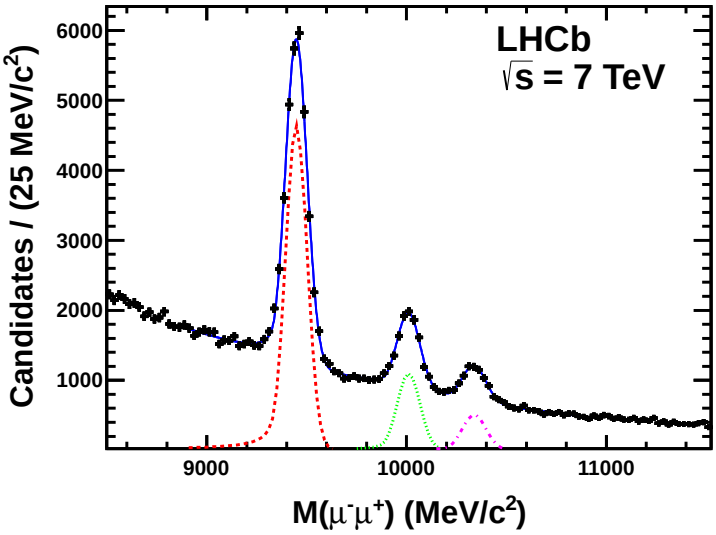

Figure 3.31 – Invariant-mass distribution of the di-muon pairs around the upsilon masses.

early LHCb results [74], where the three upsilon resonances can be resolved when reconstructed as a pair of muons. Figure 3.31 shows the invariant mass of the $\Upsilon(1S)$, $\Upsilon(2S)$ and $\Upsilon(3S)$ candidates, where the mass resolution of the $\Upsilon(1S)$ is $\sigma_{\Upsilon(1S)} = 51.7 \pm 0.4\,\text{MeV}$.

4 Calibration of the SPD detector

The correct calibration of all the LHCb sub-detectors is a necessary ingredient to ensure the good quality of the recorded data. This chapter describes the procedure followed during the commissioning of the detector with cosmic rays and first LHC collisions to achieve the final calibration. The procedure is based on the comparison of the measured energy deposited by particles in the detector, with the expected energy given by the convolution of a Landau distribution with a Poisson distribution.

4.1 Energy deposition of minimum ionizing particles in the SPD

When charged particles traverse a thin material, they deposit an energy given by the Landau distribution, which is characterised by a narrow peak and a long tail towards positive values. The mathematical expression of its probability density function is [75]

$$\psi(\lambda) = \frac{1}{2i\pi}\int_{c-i\infty}^{c+i\infty} e^{(s\log s+\lambda s)}ds\,, \tag{4.1}$$

where c is any positive real number and λ is the dimensionless quantity

$$\lambda = \frac{E - E_{\mathrm{MIP}}}{\Delta}\,, \tag{4.2}$$

being E_{MIP} the most probable energy loss and Δ a parameter depending on the absorber. The parameter Δ can be computed from

$$\Delta = \frac{2\pi N e^4}{m_e v^2}\frac{Z}{A}x\,, \tag{4.3}$$

where N is Avogadro's number, m_e is the electron mass, v is the velocity of the particle, Z and A are the atomic number and the mass number of the absorber respectively, and x is the area density of the absorber. In the case of the SPD, the absorber is made of polystyrene with a $\frac{Z}{A}$ ratio of 0.54 and a density of $1.06\,g\,cm^{-3}$ [29]. Hence, assuming that the particles traversing the detector travel at the speed of light, the Δ parameter for the SPD is equal to 0.13 MeV.

The number of photoelectrons (k) generated in the PMT photo-cathode follows a Poisson distribution given by

$$f(k, N_{\text{phe}}) = \frac{N_{\text{phe}}^{k} e^{-N_{\text{phe}}}}{k!}\,, \tag{4.4}$$

where N_{phe} is the average number of photoelectrons produced in the photo-cathode for a particular cell, which depends on the properties of the cell itself, the fibre and the PMT.

The probability density function of the deposited energy is given by the convolution of both distributions, as displayed in Fig. 4.1.

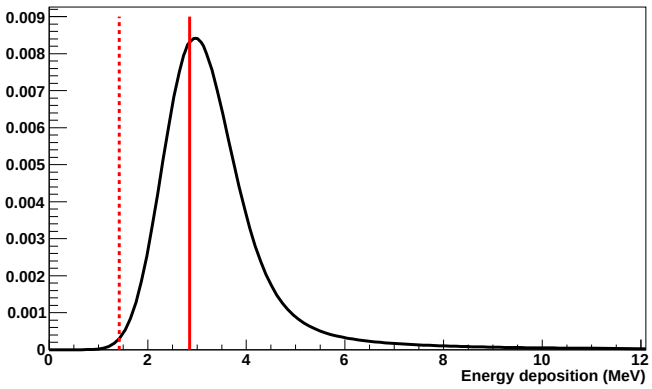

Figure 4.1 – Distribution of the energy deposited by minimum ionizing particles in the SPD from the convolution of the Landau and Poisson distributions. The solid vertical line corresponds to E_{MIP} and the dashed vertical line to the comparator threshold set at $0.5\,E_{\text{MIP}}$

When a particle traverses perpendicularly the SPD cells, it leaves an average energy of 2.85 MeV [76]. The maximum amount of material traversed by particles following a straight line from the interaction point is 107% of the SPD depth. This geometrical dependency, together with the effect of the magnetic field, will be absorbed by the calibration constant as it will be based on the typical tracks that traverse a cell.

The efficiency of the SPD to detect charged particles is given by the integral of the probability density function between a given energy value and infinity. The dependence of this efficiency with the threshold value is shown in Fig. 4.2.

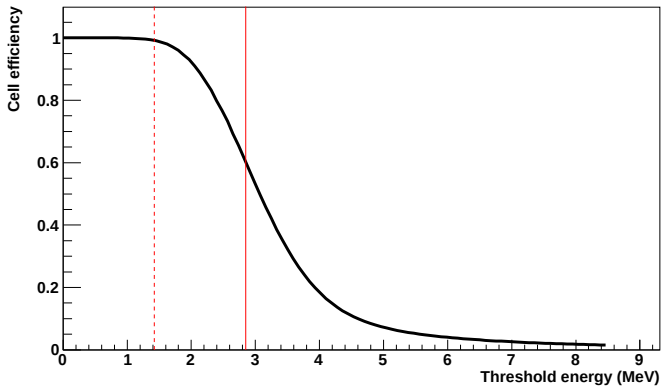

Figure 4.2 – Expected efficiency of the SPD response to particles as a function of the threshold value, as obtained from the integration of the convolution of the Poisson and Landau distributions. The solid vertical line indicates the position of E_{MIP} and the dashed vertical line indicates the position of the comparator threshold set at $0.5\,E_{\mathrm{MIP}}$.

4.2 SPD electronics response to minimum ionizing particles

The output signal of the SPD integrator is the sum of two contributions: the intrinsic offset of the electronics and the signal voltage. The latter depends on the number of photoelectrons, the MAPMT gain, the ASIC gain and the MIP energy. The analytical expression for the MIP signal is given by

$$V_{\mathrm{MIP}} = V_{\mathrm{off}} + e \times N_{\mathrm{phe/\,MeV}} \times G_{\mathrm{MAPMT}} \times G_{\mathrm{ASIC}} \times E_{\mathrm{MIP}}\,, \qquad (4.5)$$

where V_{off} is the electronics offset, e is the electron charge, $N_{\mathrm{phe/\,MeV}}$ is the number of photoelectrons per MeV, G_{PMT} is the MAPMT gain, G_{ASIC} is the ASIC gain and E_{MIP} is the MIP energy in MeV.

In order to work at the aforementioned rate of 40 MHz, each channel consists of two alternating sub-channels running at half-rate which implement their own integrator and comparator. The value of the gain of the MAPMT is

shared by the two sub-channels. To optimise the space and power consumption, the discriminator is implemented through an 8-channel ASIC [77]. The channel-by-channel dispersion of the ASIC gain as well as the sub-channel dispersion is less than 3%. Therefore, the two sub-channels will be considered as a single channel as far as the calibration procedure is concerned.

A reference voltage for each VFE (V_{ref}) is adjusted using an external Digital-to-Analog (DAC) converter. This V_{ref} limits the maximum voltage that can be set in the comparator of any channel of the VFE. The value of V_{ref} has to cope with the different electronics offsets in each channel (see Sec. 4.2.1). The average V_{ref} among the hundred VFE boards is 360 mV. The value of the comparator threshold in each channel can be set at fractions of this voltage using a 7-bit internal DAC, resulting in a resolution of around 3 mV for setting the threshold value. As the output signal from the MAPMT is of the order of 100 mV/MIP (see Sec. 4.2.2) under nominal HV conditions, the resolution relative to the E_{MIP} is around 3%. The objective of the calibration described is to find a calibration factor for each cell with a relative uncertainty of the same order.

The number of photoelectrons on Eq. 4.5 depends on the cell, fibre and MAPMT properties, while the ASIC gain and the offset are intrinsic to the electronics. The gain factor G_{ASIC} is different for every channel although each ASIC reads out 8 channels, and the electronics offset varies from sub-channel to sub-channel. As shown in Fig. 4.3, the G_{PMT} value has a RMS up to a 10% of G_{PMT}.

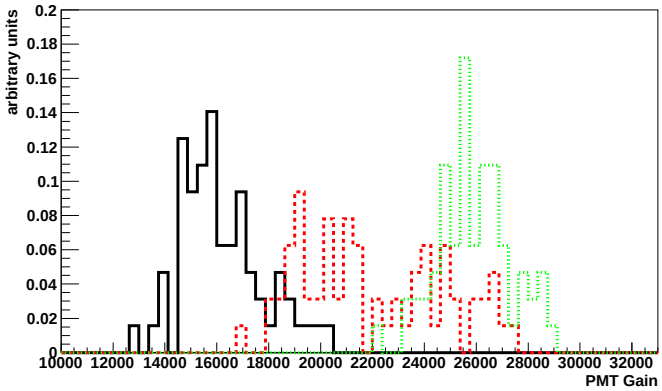

Figure 4.3 – Distribution of the G_{PMT} per channel for a typical MAPMT (black solid), for the MAPMT with higher α (red dashed) and for the MAPMT with lower α (green dotted). See Sec. 4.2.2 for the definition of α.

4.2.1 Measurement of the electronics offset

The electronics offset has been systematically monitored by performing regularly threshold scans in absence of signal. Figure 4.4 shows that the difference in the electronics offset with and without HV applied is negligible and only driven by the electronics noise. This measurement has been done for the alternating two sub-channels in each channel.

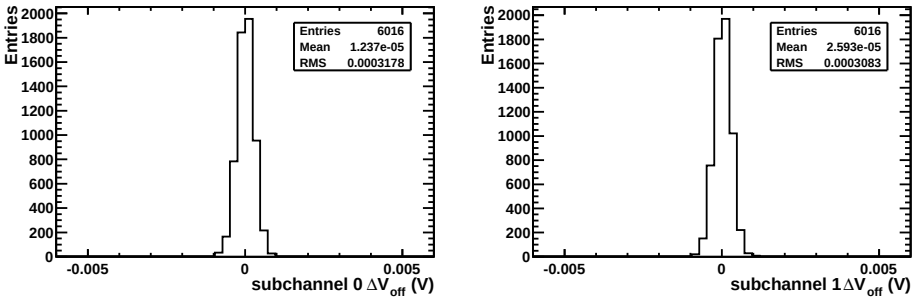

Figure 4.4 – Difference in the electronics offset with and without HV applied for sub-channel 0 (left) and sub-channel 1 (right).

The precision in the determination of V_{off} is given by the internal DAC which is on average 3 mV. Figure 4.5 shows the values of the electronics offset measured on February 23^{th} 2010 which are, on average, around -46 mV.

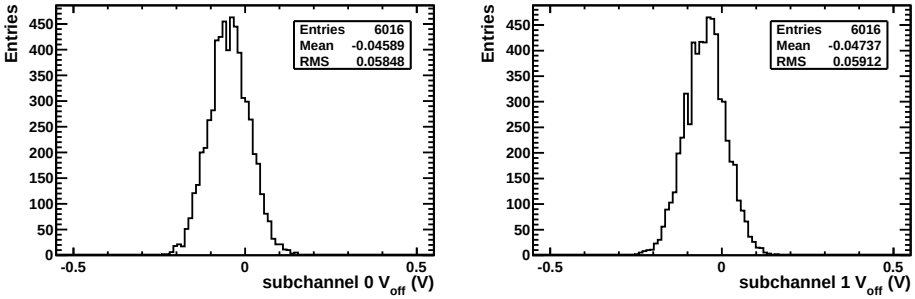

Figure 4.5 – Electronics offset measured on February 23^{th} 2010 for sub-channel 0 (left) and sub-channel 1 (right).

Several measurements of the offset have been performed over the last years. The difference of two different measurements taken on February 23^{th} 2010 and August 13^{th} 2010 for the two sub-channels is shown in Fig. 4.6. The value of the electronics offset is found to be very stable over long periods of time.

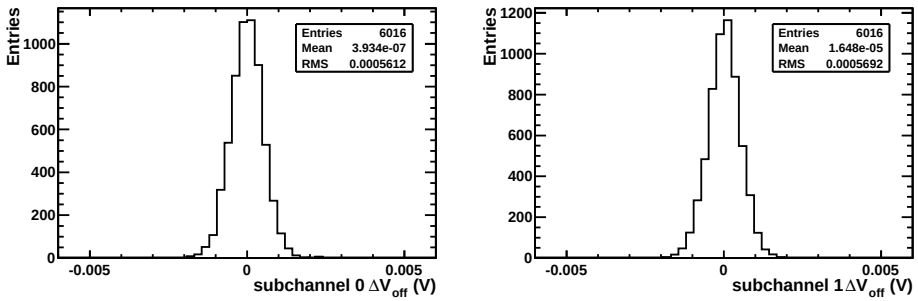

Figure 4.6 – Differences in the electronics offset measurement taken on February 23^{th} 2010 and August 13^{th} 2010 for sub-channel 0 (left) and sub-channel 1 (right).

The RMS of the electronics noise was measured at the laboratory to be between 2.2 and 2.5 mV depending on the channel [78] while the MIP signal is on average 100 mV (see Sec. 4.2.2). Thus, the electronics noise represents, in average, a 2.4% of V_{MIP}.

4.2.2 Pre-calibration

The different gain factors entering in the calibration of the signal output were measured in test benches or in the laboratory before the detector installation. This allowed to compute the pre-calibrated gain factors for each channel [79].

The number of photoelectrons per MIP produced at each photo-cathode when a MIP traverses the detector cells was measured using cosmic rays. The set-up consisted in eight scintillation counters with dimensions of 16 $\times$ 100 $\times$ 2 cm^3 arranged in two planes. The planes were crossed in order to select vertical cosmic rays, and the coincidence of signal in both planes was used as trigger. The vertical trigger rate was about 45 Hz [80]. As the number of photoelectrons produced at the photo-cathode follows a Poisson distribution, it can be measured as

$$N_{\mathrm{phe}}^{\mathrm{MIP}} \simeq \frac{\mu_s^2(\mathrm{MIP})}{\sigma_s^2(\mathrm{MIP})}\,, \tag{4.6}$$

where μ_s and σ_s are the mean and standard deviation of the distribution of the measured charge at the PMT anode. Figure 4.7 shows the distribution of the number of photoelectrons measured for all the cells. The different average values for different detector zones is due to the variations of light collection efficiency as a function of the cell size.

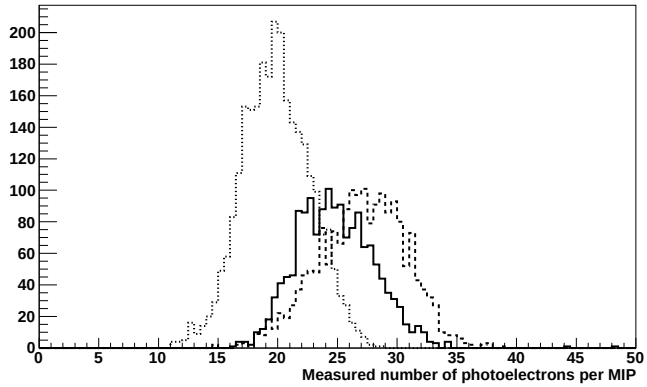

Figure 4.7 – Distribution of the measured number of photoelectrons per MIP obtained in a test bench for the inner (solid), middle (dashed) and outer (dotted) [80].

The PMT gain per channel was measured at the laboratory by using a LED that illuminated directly the whole PMT surface and changing the bias voltage from 450 V to 800 V in steps of 10 V [81]. The gain per channel was then measured as

$$G_{\mathrm{PMT}}^{\mathrm{LED}} \propto \frac{\mu_s^{\mathrm{LED}}}{N_{\mathrm{phe}}^{\mathrm{LED}}}\,, \tag{4.7}$$

and the dependence of the PMT gain on the HV can be parametrised by

$$G_{\mathrm{PMT}} = G_0 V^{\alpha}\,. \tag{4.8}$$

Figure 4.8 shows the gain as a function of the HV for a typical PMT, and for those which have the highest and lowest values of the α exponent. For the normal detector operation, the HV applied to the PMT is chosen to satisfy the requirement that the channel with the highest PMT gain produces an integrated charge of 100 fC/MIP [78]. This value is chosen to avoid a premature ageing of the PMT. On average, this corresponds to a HV around 580 V. Choosing in this way the HV applied to the PMT, implies that the MIP signal for the channels with highest PMT gain in each VFE is always the same.

The HV in the PMT is applied by means of ADC counts. For the typical HV working point the precision in setting the HV is around 3.5 V. The uncertainties in G_0 and α are small, yielding a precision in G_{PMT} of 3%.

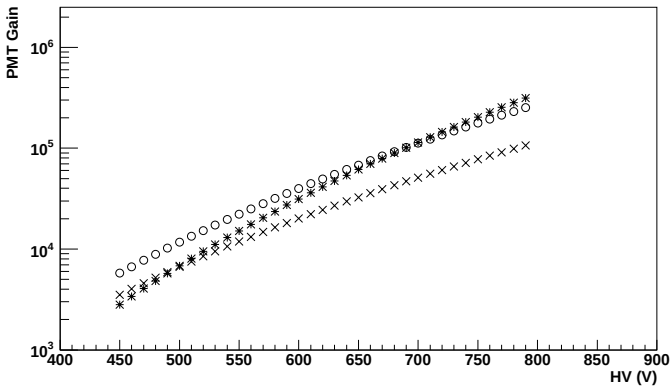

Figure 4.8 – Gain of the PMT as a function of the HV applied for a typical PMT (open circle), for the PMT with higher α (stars) and for the PMT with lowest α (crosses).

As stated before, the dispersion of the ASIC gain for all sub-channels belonging to the same device can be considered negligible. Thus, G_{ASIC} was considered to be a common parameter for all the sub-channels with a value of 1.2 mV/MIP [78].

Taking all the terms into account, the pre-calibration gain factors for each cell were computed. The distribution of these factors in mV/MIP is shown in Fig. 4.9. Note that, for the pre-calibration, the average MIP corresponds to a signal of 100 mV/MIP in the electronics.

4.2.3 Calibration strategy

The energy deposited by MIPs in the SPD will be used as a reference for calibrating the gain and for optimizing the detector response. The gain obtained in this way will be represented as a correction factor per cell to be applied to the pre-calibration gains shown in Fig. 4.9. The threshold value will then be set on the electronics at $0.5\,E_{\mathrm{MIP}}$ taking these factors into account.

The efficiency of the SPD to detect MIPs is a function of the value of the threshold applied (see Fig. 4.2). This efficiency can be measured as the ratio between the number of tracks that have an associated hit and the total number of tracks in a given region.

By fitting the measured efficiency as a function of the threshold, with the theoretical expression displayed in Fig. 4.2, the correction factor can be extracted as well as the number of photoelectrons and the maximum efficiency

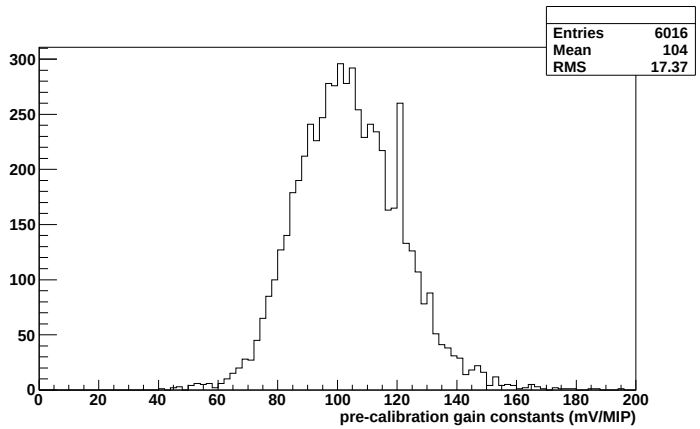

Figure 4.9 – Distribution of the pre-calibrated gain factors in mV/MIP. The accumulation of channels at 120 mV/MIP is due to the fact that the HV applied to the PMT is chosen to satisfy the requirement that the channel with the highest PMT gain produces an integrated charge of 100 fC/MIP. Higher values of the pre-calibrated gain constant are due to a higher number of photoelectrons in channels with lower PMT gain.

for a given cell.

The first calibration was done in the first months of 2009, before the LHC start-up, using cosmic rays as a source of MIP signals. The limited statistics and the random arrival time of cosmic muons with respect to the integrator clock made the calibration with cosmic rays challenging. However, this first step allowed to validate the pre-calibration and hence to prepare the detector to be used to provide the first minimum bias trigger when the collisions started on 23 of November 2009. Afterwards, in the first months of 2010, tracks from proton-proton collision events were used to obtain the final calibration factors with much higher statistics, and under a controlled environment.

Unless stated otherwise, the threshold values in the scans are given as fractions of the energy that would correspond to the MIP peak according to the pre-calibration ($E_{\mathrm{MIP}}^{\mathrm{pre}}$).

4.3 Initial calibration with cosmic rays

Data at four different threshold values were taken for cosmic rays. However, due to their large statistical uncertainty and the large number of free parameters in the fit, it was not possible to fit completely the theoretical

expression. Instead, the method used to obtain the correction factors was to compare the efficiency measured with the threshold value at $1\,E_{\mathrm{MIP}}^{\mathrm{pre}}$ with the theoretical prediction. This point is the one with the highest sensitivity, as it is placed in the middle of the transition region between high and low efficiencies (see Fig. 4.2).

The events were triggered using the coincidence of a signal at ECAL and HCAL, providing a rate of $\sim$10 Hz. In order to increase the efficiency on cosmic muons, higher photomultiplier gains were used. An uniform gain at the level of 10^5 was implemented for all ECAL and HCAL channels.

The LHCb capability of triggering consecutive events was exploited in order to select muons arriving close to the beginning of the integration window. In this mode, the DAQ system packs consecutive events into a Multi Event Packet (MEP) which can contain up to 15 consecutive events centred around the triggering event (T0). A total amount of four million cosmic events were taken under these conditions. Out of them, 420000 were used before the calibration to synchronise the SPD with respect to ECAL and HCAL [82]. For the synchronization, the SPD threshold was set at nine times the RMS of the electronics noise away from the electronics offset, which corresponds roughly to $0.25\,E_{\mathrm{MIP}}^{\mathrm{pre}}$. The total amount of data taken for the calibration at $1\,E_{\mathrm{MIP}}^{\mathrm{pre}}$ was 1.6 million events.

4.3.1 Track reconstruction and selection

The data recorded were analysed with the specific LHCb Calorimeter software for online monitoring and commissioning, Orwell [83]. A dedicated algorithm reconstructs the cosmic tracks using only ECAL and HCAL information. Firstly, the algorithm builds two independent 2D tracks from the hits at ECAL and HCAL separately. Afterwards, the information of the two tracks is combined into a 3D track and a cut in the track χ^2 is applied [84]. Besides, in order to ensure a good purity, events with more than one reconstructed track are vetoed. This procedure yields a track for approximately 80% of the triggered events.

The algorithm also gives information about the direction of the track and the arrival time of the cosmic muon with respect to the start of the signal integration time in the calorimeter. The latter is obtained by comparing the energy collected by the calorimeters in consecutive integration windows [85]. Knowing the distance between the ECAL and the SPD, one can infer the arrival time of the cosmic muons with respect to the start of the SPD integration window.

Certain extra requirements in the track properties were requested to study the SPD efficiency. The requirements are explained below, with the figure

showing always distributions after applying the list of precedent conditions.

Material traversed: in order to mimic as much as possible particles coming from a proton-proton collision, a cut in the material traversed by the muons was applied. Particles traversing more than a 120% of the SPD cell thickness were rejected. This is equivalent to traversing more than 18 mm of scintillator. This requirement selects horizontal cosmic tracks which reduces by a factor seven the available statistics. Figure 4.10 shows the distribution of the material traversed by cosmic rays.

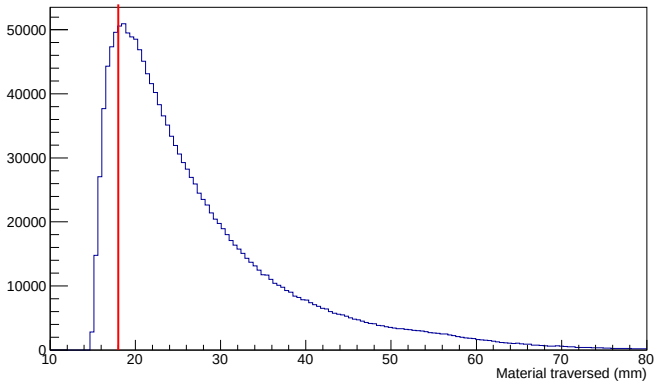

Figure 4.10 – Distribution of the material traversed by reconstructed and selected cosmic rays as described in the text above. The vertical line indicates the cut applied at 18 mm.

Arrival time: as there can be partial energy deposition in consecutive integration windows, a cut in the arrival time of the muons to the SPD was applied. Figure 4.11 illustrates the dependency of the global SPD efficiency as a function of the arrival time of the cosmic muons, being 0 the start of the integration window. The central arrival time was chosen as the value that maximised the efficiency and a window of ± 5 ns around this value was used to select the events. This condition represents an extra factor four in the reduction of the available statistics.

Single SPD hit: so as to purify the sample of single cosmic muons, events with more than one SPD hit were removed. Also, for the two previous and two following integration windows, hits can only be present in the same cell as the T0.

Track uncertainty: the uncertainty in the extrapolation to the SPD plane was required to be small to avoid badly extrapolated tracks. Thus, requirements in the uncertainties of the X and Y coordinates of 150 mm were

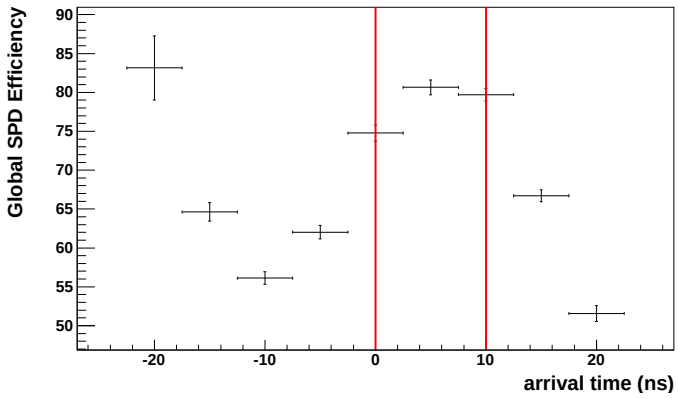

Figure 4.11 – Efficiency as a function of the arrival time of the cosmic muons with respect to the SPD integration start for tracks that have passed the requirements as explained in the text above. The vertical lines indicate the window cut around the value that maximises the efficiency.

applied. The distribution of the extrapolation uncertainty is displayed in Fig. 4.12 for X (left) and Y (right) coordinates.

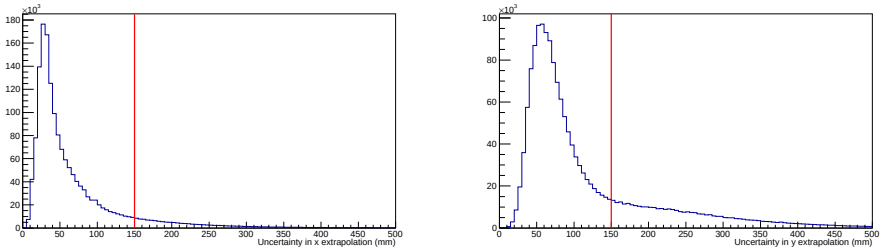

Figure 4.12 – Distribution of the uncertainty in the extrapolation to the SPD plane for X (left) and Y (right) coordinates for cosmic tracks having passed the above requirements. The cut applied is 150 mm for both coordinates.

PS Energy and single PS hit in 3σ: in order to confirm the reconstructed track, it was required the presence of one and only one hit in the PS closer than 3σ to the extrapolation with an energy higher than 1.14 MeV. In this case, σ is defined as the uncertainty in the extrapolation at the PS plane. The energy requirement to define a hit is roughly equivalent to $\sim \frac{2}{3}$ of a MIP (approximately 40 ADC counts). The distribution of the PS energy is represented in Fig. 4.13.

After these requirements, the available statistics is reduced to a 3% of

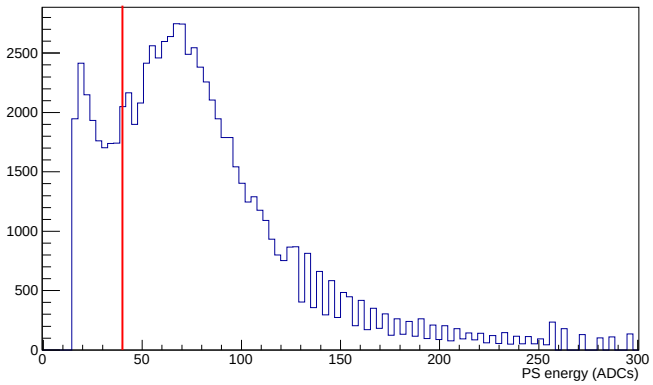

Figure 4.13 – Distribution of the energy deposited in the PS by cosmic muons in ADC counts after passing the previous requirements. The cut applied for the PS energy was 40 ADC counts, roughly equivalent to 1.14 MeV. The structure at high energy is due to the integer value in ADCs of PS energy.

the initial sample. Table 4.1 shows the number of remaining events after each cut is applied. Having 6016 cells, a cell-by-cell efficiency measurement could not be obtained with the remaining statistics, instead, a VFE-by-VFE efficiency was measured.

Requirement	Number of events ($\times 10^3$)
Total events	1605.0
Material traversed	231.0
Arrival time	60.4
Single SPD hit	58.0
Track uncertainty	57.5
PS Energy and single PS hit in 3σ	44.2

Table 4.1 – Number of events remaining after each of the requirements are applied for cosmic track selection.

4.3.2 Results

As stated above, only the point taken at $1\,E_{\mathrm{MIP}}^{\mathrm{pre}}$ was used in the calibration as it is the most sensitive to E_{MIP}. As the efficiency was computed by VFE,

the number of photoelectrons considered in the theoretical expression was the average among the different cells that correspond to a single VFE.

Figure 4.14 shows the correction factor per VFE obtained from cosmic data. The results show that the overall pre-calibration was correct to a 15% level [86].

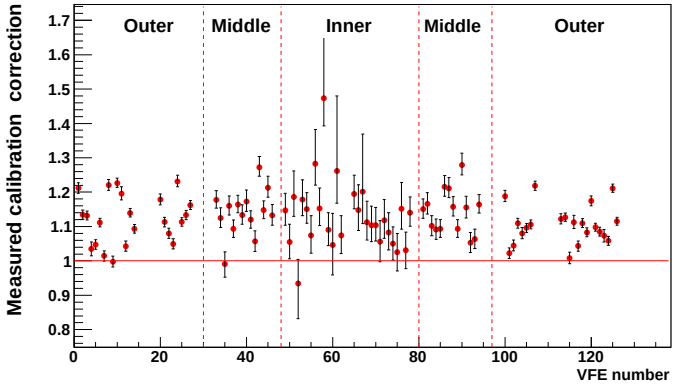

Figure 4.14 – Correction factor per VFE to be applied to the pre-calibrated gains as obtained from cosmic analysis. The horizontal solid line correspond to a perfect pre-calibration. The vertical dashed lines divide the different regions.

4.4 Calibration with LHC collisions at 7 TeV

In November 2009 the LHC started to provide proton-proton collisions at a center-of-mass energy of $\sqrt{s} = 900\,\text{GeV}$. About 3.5 million collisions were collected with a minimum bias trigger. These data were used first to synchronise the SPD with the other detectors and with respect to the LHC clock to the level of 1 ns [87]. Afterwards, 10^5 events were recorded with the SPD thresholds at $1\,E^{\text{pre}}_{\text{MIP}}$. This allowed to measure the occupancy ratio between data at the nominal point and at $1\,E^{\text{pre}}_{\text{MIP}}$, which could be compared with the theoretical ratio in order to cross-check the results obtained with the cosmic rays calibration.

In March 2010, collisions at the LHC reached a center of mass energy of $\sqrt{s} = 7\,\text{TeV}$, starting the data taking for the 2010 calibration campaign.

4.4.1 Data sample for calibration

Data at seven different threshold values have been recorded using LHC collisions. The first six points taken correspond to 0.3, 0.5, 0.8, 1.0, 1.4 and 1.8 $E^{\text{pre}}_{\text{MIP}}$. The criterion used to choose them was to have enough points in the transition region to maximise the sensitivity to E_{MIP} and also to ensure that the maximum and minimum efficiency was reached in all the cells. Only for a 3% of the cells a seventh point at 2.1 $E^{\text{pre}}_{\text{MIP}}$ was taken, keeping the other 97% at the nominal threshold of 0.5 $E^{\text{pre}}_{\text{MIP}}$. Table 4.2 shows the initial statistics and the conditions for each point [88].

fraction of $E^{\text{pre}}_{\text{MIP}}$	# initial events ($\times 10^3$)	μ	Pile-up
0.3	4383	0.1	1.03
0.5	33241	0.1	1.03
0.8	20500	0.1	1.03
1.0	10868	0.1	1.03
1.4	989	0.8	1.5
1.8	954	0.8	1.5
2.1 (only 3% of cells)	668	1.2	1.7

Table 4.2 – Initial statistics in thousands and conditions of visible proton-proton interactions per crossing (μ) and proton-proton interactions per visible event (Pile-up).

4.4.2 Event reconstruction and selection

All charged particles with a relatively perpendicular incidence to the SPD are valid for calibration. In this study, all T-tracks are used, without any requirement on the Vertex Locator (VELO) or Tracker Turicensis (TT). The standard LHCb reconstruction algorithm makes T-tracks after having removed the hits belonging to a long or downstream track [39]. Here, the T-track reconstruction algorithm is run standalone using all the available hits.

The data used in the analysis are those selected by the minimum bias stripping stream. Due to the large downscaling of the minimum bias triggers when the point at 2.1 $E^{\text{pre}}_{\text{MIP}}$ was taken, data from the charm stripping stream are used in this case to increase the statistics.

The global requirement for any event to be considered is that it has to belong to the beam-beam bunch crossing category and has to have at least one hit in the SPD.

4.4.3 Track selection

Tracks are required to satisfy certain quality criteria. Below, distributions of variables on which requirements are applied are shown for tracks that have passed the precedent series of conditions.

Track χ^2/DoF: in order to remove ghost tracks, the χ^2/DoF from the track fit has to be smaller than 2.5. Fig. 4.15 illustrates the distribution of the track fit χ^2/DoF.

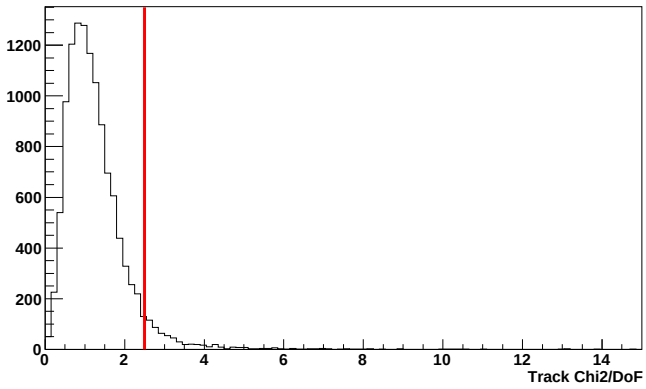

Figure 4.15 – Distribution of the χ^2/DoF of the tracks used. The vertical line indicates the cut applied at 2.5.

Extrapolation uncertainty: to ensure a good extrapolation to the SPD plane, the uncertainty in the extrapolations at the SPD plane on the X and Y coordinates is required to be smaller than 1.5 mm. Fig. 4.16 shows the distributions of these two uncertainties.

Number of track hits: by studying the number of track hits, a good fraction of ghost tracks can be rejected. The maximum number of hits that a T-track can have depends on whether it is made out of Outer Tracker (OT) or Inner Tracker (IT) measurements. For OT, the maximum number of measurements is 24 [45] while for IT it is 12 [44]. Figure 4.17 shows the distribution of the number of OT hits for tracks with and without an associated SPD hit (note that here the SPD information is used as an estimator of the ghost-track likelihood). Requiring at least 18 hits for tracks containing

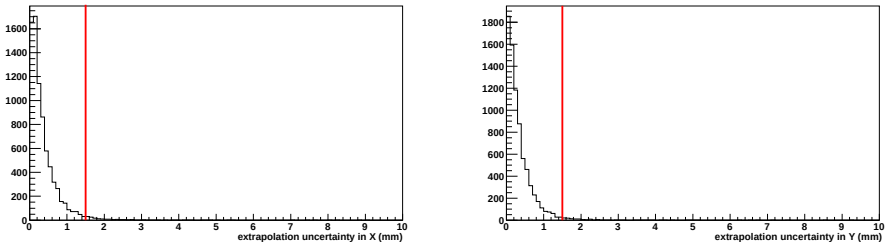

Figure 4.16 – Distribution of the uncertainties in the track extrapolation at the SPD plane for X (left) and Y (right) coordinates, for tracks satisfying all the previous requirements. The vertical line shows the cut applied at 1.5 mm for both coordinates.

OT hits reduces significantly the number of ghost tracks. The difference in the number of IT hits for tracks with and without an associated SPD hits is very small. Thus, tracks made out of IT hits are not required to have a minimum number of hits.

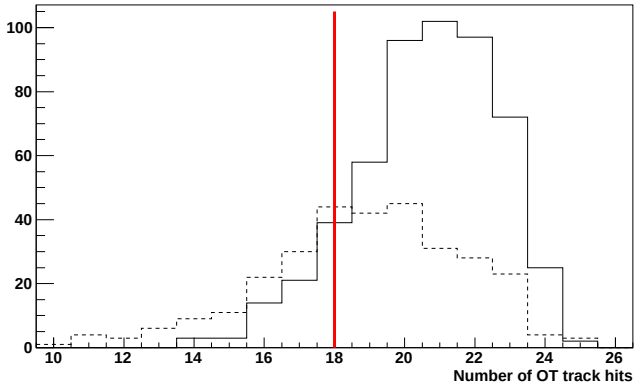

Figure 4.17 – Distribution of the number of OT hits for tracks with an associated SPD hit (solid) and without an associated SPD hit (dashed), for tracks satisfying all the previous requirements. The vertical line indicates the cut applied at 18 hits.

Material traversed: in order to avoid particles leaving an excessive ionization in teh SPD cells due to a high bending angle, particles are required to traverse at most 120% of the SPD thickness, which corresponds to 18 mm. Fig. 4.18 illustrates the distribution of the material traversed in the SPD by T-tracks.

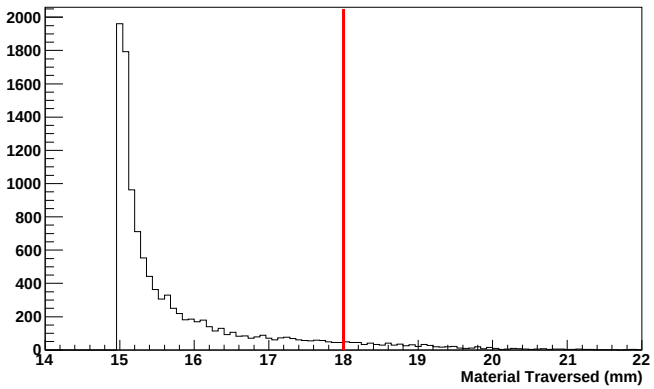

Figure 4.18 – Distribution of the material traversed in the SPD by tracks passing the previous requirements. The vertical line indicates the cut applied at a 120% of the cell thickness.

Extrapolation well within the cell limits: to minimise the impact of alignment problems, the effective area of the cell is reduced in the borders by 8 mm. The alignment between the SPD and the tracking stations will be treated in depth in Sec. 4.5.

The extrapolations in X and Y have to be at least $3\,\sigma$ away from the borders of the SPD cell effective area.

Track confirmation with PS: only events were the extrapolation in the PS plane is in the cell behind the SPD hit are kept. Besides, the PS cell energy has to be in the range $[1.5\,,4.0]$ MeV, at the cost of rejecting some electrons but having a higher single-particle purity. In addition, the track has to be inside the PS cell limits with, at least, $3\,\sigma$. Here, σ is defined as the uncertainty in the extrapolation at the PS plane. The distribution of the PS energy in the cell behind the SPD hit is shown in Fig. 4.19.

After all the requirements are applied, the available number of tracks per event is reduced by a factor three. Table 4.3 shows the reduction of the number of useful T-tracks per event after each cut.

Residual effects from ghost tracks and misalignment are expected to reduce by the same factor the efficiency at any value of the threshold. Hence, their effects do not displace the position of the transition region but only can change the value of the slope. This leads to the fact that these effects do not affect significantly the estimation of the correction factor, but only the number of photoelectrons and the maximum efficiency reachable.

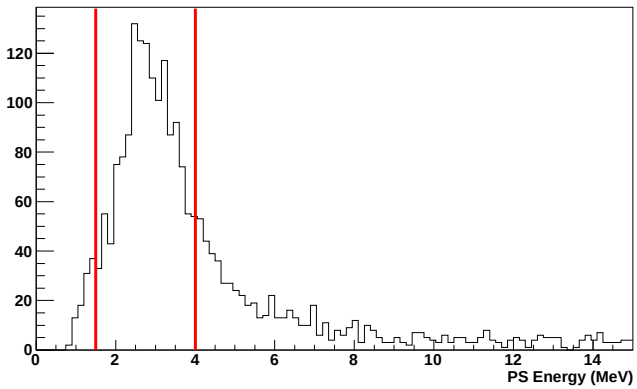

Figure 4.19 – Distribution of the PS energy in the cell behind the SPD hit for tracks passing all previous requirements. The vertical lines indicate the window cut applied in the region $[1.5\,, 4.0]$ MeV to select only single MIPs.

Requirement	# of tracks per event
Total	18.5
χ^2/DoF	17.5
Extrapolation uncertainty	17.3
Number of track hits	16.4
Material traversed	15.3
Extrapolation in SPD eff. area	6.8
Track confirmation with PS	5.9

Table 4.3 – Number of T-tracks per event remaining after each condition is required.

4.4.4 Calibration results

By fitting the theoretical curve depicted in Fig. 4.2 to the measured efficiency-threshold curve, we obtain the correction factor, the number of photoelectrons and the maximum efficiency reachable by each cell. An example of the fit for the cells with the highest and lowest correction factor and for a typical cell are shown in Fig. 4.20.

The distribution of the correction factors in each region is shown in Fig. 4.21. On average, the correction factor is ∼0.8, which indicates that the pre-calibration overestimated the detector and electronics response by a

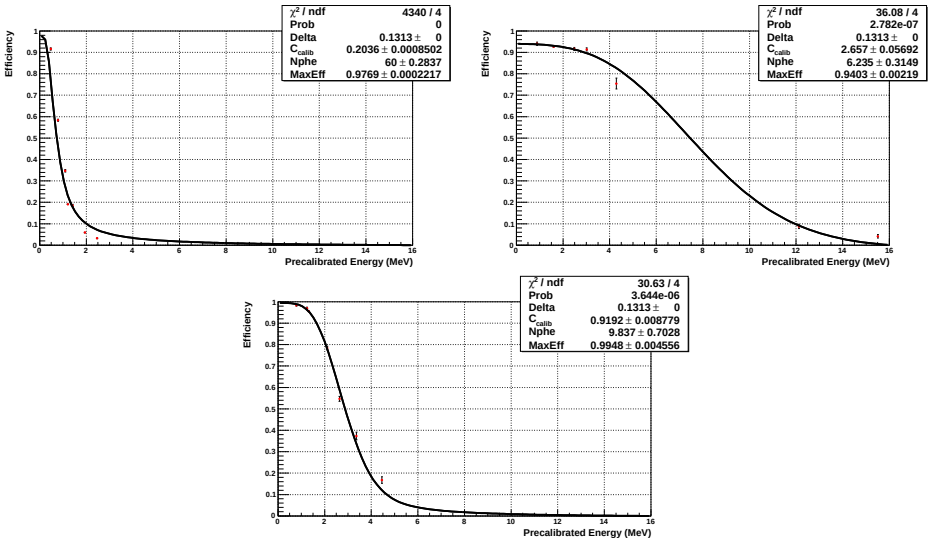

Figure 4.20 – Fits for the cell with the lowest correction factor (top left), for the cell with the highest correction factor (top right) and for a typical cell (bottom).

20%. Figure 4.22 illustrates the distribution of the relative fit uncertainty in the correction factors. The statistical uncertainty given by the fit is of the order of 1.5%, which is well below the resolution in setting the threshold value due to the step of the internal DAC of the ASIC. The systematic uncertainty in the calibration factor may come from a poor track purity and a high ghost-track abundance. However, as discussed in the previous section, this only affects the maximum reachable efficiency by a cell and do not affect the calibration factor. Another source of systematic uncertainty could be a wrong estimation on the number of photoelectrons, but this will change the slope of the transition region and leave unaffected the calibration factor. The complete calibration constants corresponding to the product of the pre-calibration constants and correction factors are displayed in Fig. 4.23. On average, the calibration constant for the cells corresponds to $\sim 80\,\mathrm{mV/MIP}$.

Figure 4.24 shows the distributions of the threshold set in the electronics which are well centred at $0.5\,E_{\mathrm{MIP}}$ as this is the nominal working point, and their width is given by the resolution in setting the threshold due to the internal DAC step. The RMS in the threshold values is a 4% of E_{MIP} in good agreement with the expected limit.

Once the correction factors were computed, the threshold values where set to the nominal working point of $0.5\,E^{\mathrm{pre}}_{\mathrm{MIP}}$. It was then checked that the output signal of the detector is far enough from the electronic noise. Figure 4.25

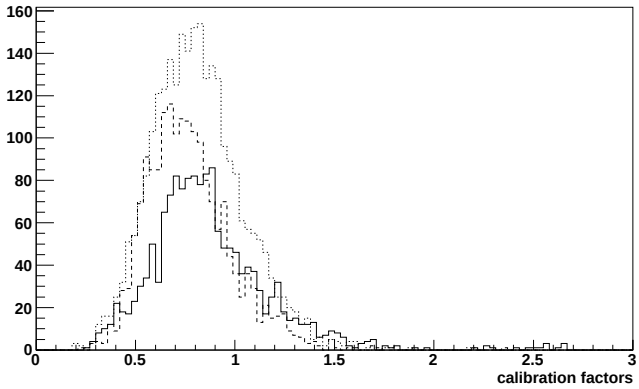

Figure 4.21 – Distribution of the correction factors to be applied to the cells as obtained from 2010 proton-proton collisions, for inner (solid), middle (dashed) and outer (dotted). The average values are 0.87, 0.77 and 0.81, respectively.

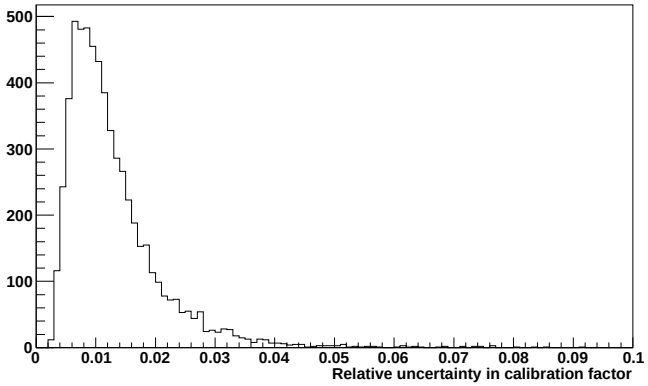

Figure 4.22 – Distribution of the relative fit uncertainty in the correction factors as obtained from 2010 proton-proton collisions.

illustrates the distributions corresponding to $(V_{\text{th}} - V_{\text{offset}})/\sigma_{\text{noise}}$ for each sub-channel at the nominal working point. This distribution represents the separation in number of noise σ between the threshold and the electronics offset. The average value is around 15 noise σ, being the lowest value close to 5 noise σ. Table 4.4 shows the number of channels and sub-channels below 5 and 9 noise σ.

After these checks were done, the correction factors were applied into

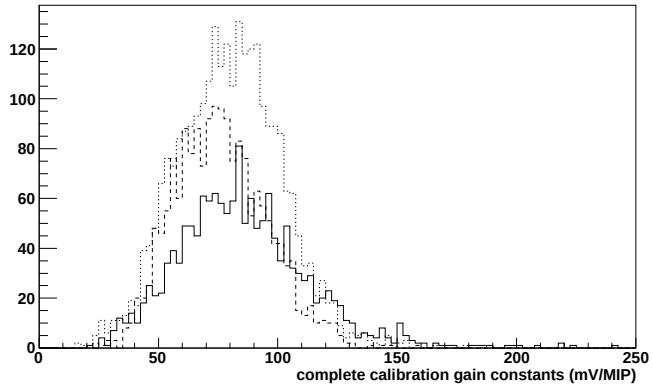

Figure 4.23 – Distribution of the complete calibration factors of the cells as obtained from pre-calibration and 2010 proton-proton collisions, for inner (solid), middle (dashed) and outer (dotted). The average values are 85, 77 and 81 mV/MIP, respectively.

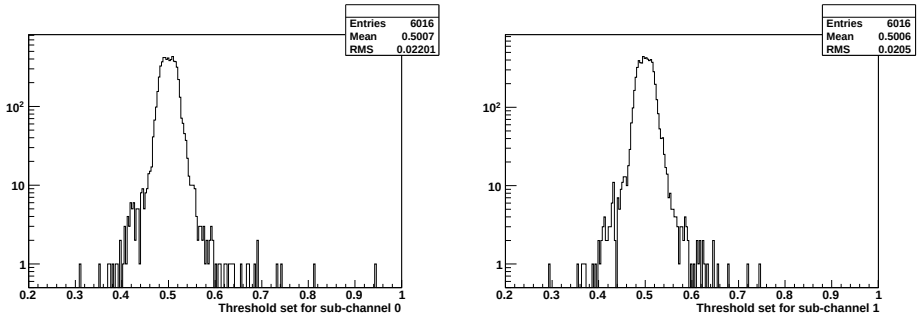

Figure 4.24 – Distribution of the $E_{\mathrm{th}}/E_{\mathrm{MIP}}$ threshold set in the electronics for sub-channel 0 (left) and sub-channel 1 (right) assuming a perfect calibration. The dispersion in the threshold values corresponds to the finite step given by the internal DAC of the VFE electronics.

# noise σ	sub-channel 0	sub-channel 1	both sub-channels
5	10	8	5
9	237	223	192

Table 4.4 – Number channels and sub-channels closer to the electronics noise in less than 5 or 9 of noise σ.

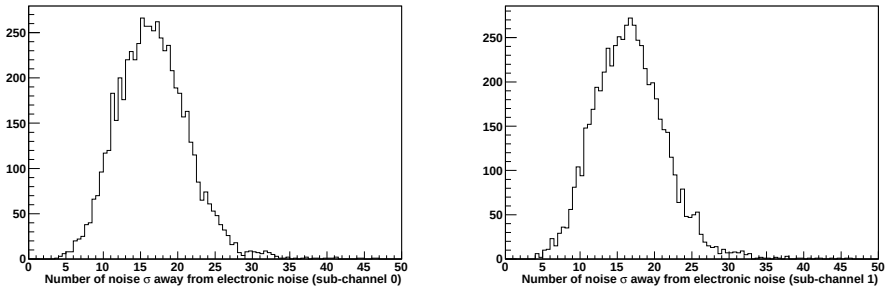

Figure 4.25 – Distribution of the number of noise *sigmas* between the threshold and the electronics noise for sub-channel 0 (left) and sub-channel 1 (right).

the SPD electronics since the beginning of the 2011 data taking. Finally, the calibrated-cell efficiencies were checked using 2011 collision data. Figure 4.26 shows the distribution and the two-dimensional map of the cell efficiencies for 2011 collision data. After the calibration procedure, the SPD detector has a mean cell efficiency of 95% with a RMS of 3%.

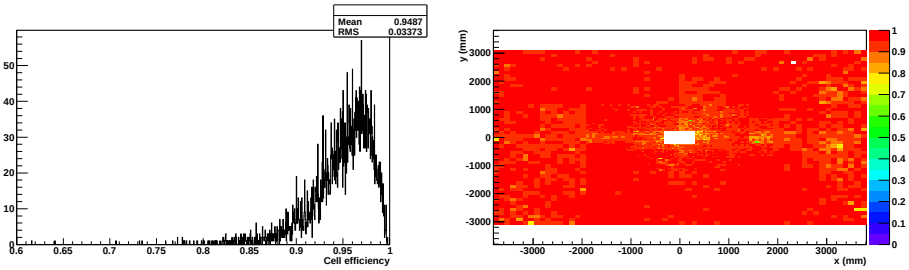

Figure 4.26 – Distribution of the 2011 cell efficiencies (left) and two-dimensional map of the cell efficiencies in their real position on the detector (right).

Number of photoelectrons

The number of photoelectrons obtained from the fit is represented in Fig. 4.27, showing an average value of 11.5 photoelectrons per MIP with a dispersion of the 35%.

The difference between these values and those obtained in the test bench (Sec. 4.2.2) are shown in Fig. 4.28. On average, the fit value and the test bench measurement of the number of photoelectrons per MIP are in good agreement.

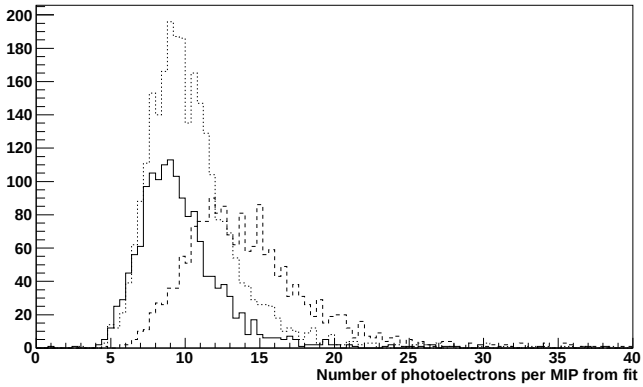

Figure 4.27 – Distribution of the number of photoelectrons per MIP extracted from the fit, for inner (solid), dashed (middle) and dotted (outer).

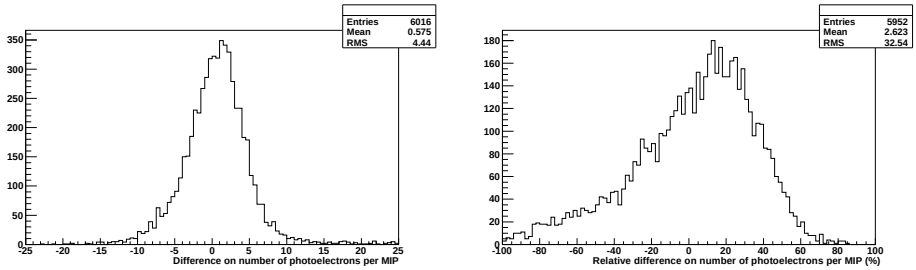

Figure 4.28 – Difference between the number of photoelectrons per MIP from the fit and the number of photoelectrons per MIP measured in the test bench (left), and relative difference between the number of photoelectrons (right).

4.5 Alignment of the SPD with respect to the trackers

The alignment of the SPD was not studied during the cosmic campaign, therefore LHC collisions provided the first data to study its effect on the cell efficiency. To evaluate the impact of alignment with respect to the trackers in the efficiency of the SPD, the cut in the border of the SPD cell has been studied. Two different cuts for the border have been considered, 3 mm and 8 mm. A comparison of the efficiency at the working point ($0.5\,E^{\mathrm{pre}}_{\mathrm{MIP}}$) for the two different values of the cut is shown in Fig. 4.29.

Table 4.5 shows the changes in the efficiency per region, as the average of the different cells in each region, for the two values of the border cut. It can

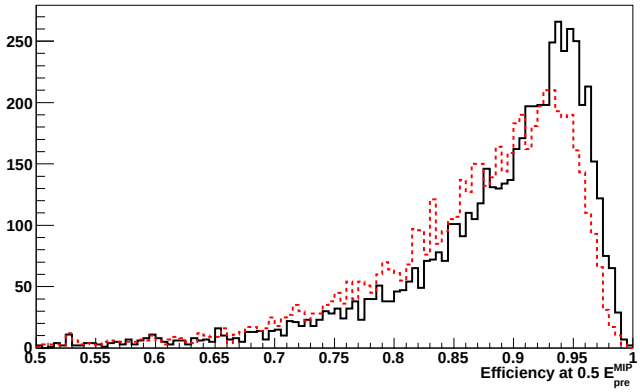

Figure 4.29 – Comparison of the efficiency at $0.5\,E^{\mathrm{pre}}_{\mathrm{MIP}}$ with a border cut of 8 mm (black solid) and 3 mm (red dashed).

be concluded that a misalignment between the SPD and the trackers exists and that it affects the efficiency computation mostly in the inner part due to the smaller size of the cells.

	Eff. with 3 mm	Eff. with 8 mm
Inner	85.98%	90.72%
Middle	92.02%	93.84%
Outer	93.70%	94.46%

Table 4.5 – Average efficiency of the cells per region at $0.5\,E^{\mathrm{pre}}_{\mathrm{MIP}}$ for two values of the border cut.

To study the SPD alignment with respect to the OT/IT cell by cell, the profile of the efficiency as a function of the extrapolated position to the SPD plane in x and y has been studied. Figure 4.30 shows the efficiency profile for a typical cell in the x and y coordinates.

The average of the distribution is taken as the real position of the center of the cell with respect to the tracking detectors. Comparing the real and nominal position one can extract the misalignment for each cell.

The displacement with respect to the nominal position of the cell in the detector is shown for x and y in Fig. 4.31. For the left side of the detector (C-side) the top part is displaced to the right, while the bottom part is

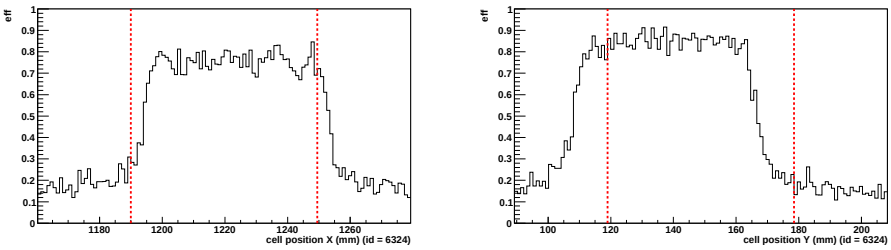

Figure 4.30 – Efficiency as a function of the track extrapolation position in a typical cell for the x (left) and y (right) coordinates. The dashed red lines indicates the nominal position of the cell.

displaced to the left. This indicates a clockwise rotation around the z-axis. On the other hand, the top part of the right side of the detector (A-side) is displaced to the left, while its bottom part is displaced to the right, which indicates a counter-clockwise rotation around the z-axis. As far as the y coordinate is concerned, the whole detector is displaced downwards with a higher displacement on the top part than on the bottom. Both vertical and horizontal shifts as well as rotations can be set into the alignment database.

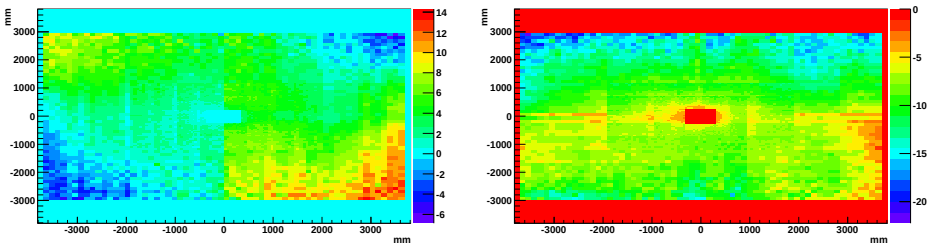

Figure 4.31 – Displacement per cell with respect to the nominal position for x (left) and y (right) coordinates.

In order to extract a quantitative amount of rotation and displacement, the average misalignment per VFE has been considered as illustrated in Fig. 4.32. The rotations and vertical displacement can also be seen clearly in this case.

The SPD is divided into 208 modules which correspond to a square active part of $48 \times 48\,\mathrm{cm}^2$. Groups of modules are arranged into eight vertical structures, Super Modules, whose active part has a rectangular shape of $96 \times 619\,\mathrm{cm}^2$. The rotation around the z-axis is extracted by fitting a linear function to the x misalignment as a function of the vertical VFE position.

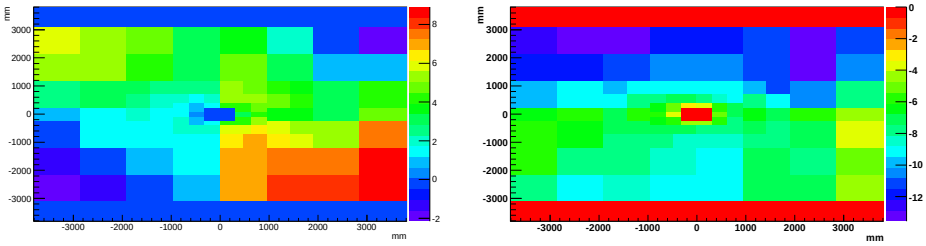

Figure 4.32 – Average displacement per VFE of the cells with respect to their nominal position, for x (left) and y (right) coordinates.

An example of the fit for Super Module 1, is displayed in Fig. 4.33.

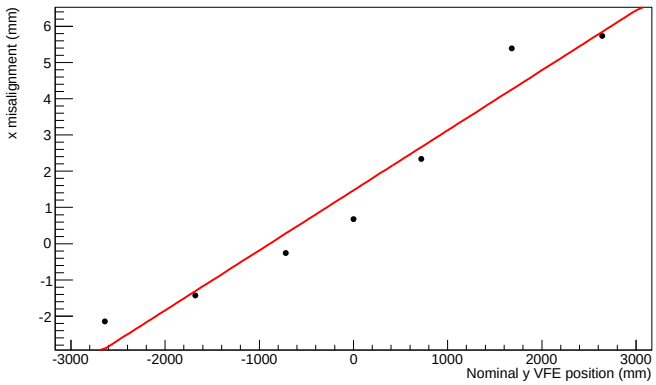

Figure 4.33 – Fit to the average x displacement of the cells with respect to their nominal position for Super Module 1.

With the fit parameters one can compute the rotation angle needed to correct the misalignment. Table 4.6 shows the rotation angle around the z-axis for each Super Module in degrees.

C-side		A-side	
SM 1	-0.093 ± 0.010	SM 5	0.041 ± 0.006
SM 2	-0.077 ± 0.006	SM 6	0.072 ± 0.003
SM 3	-0.046 ± 0.004	SM 7	0.103 ± 0.007
SM 4	-0.028 ± 0.004	SM 8	0.125 ± 0.014

Table 4.6 – Rotation around the z-axis per Super Module in degrees.

Rotations are higher for the external Super Module than for the internal ones. In the conditions database (condDB) there is only one possible rotation applicable per side. Considering that the Super Modules with higher occupancy are those in the inner part, the global rotation per side should be the one from the most internal Super Modules, i.e. SM 4 for C-side and SM 5 for A-side.

For the y coordinate, the average of the displacement per Super Module and per region has been computed (see Table 4.7). All the Super Modules are displaced by a similar amount. In this case, the databases allow to include a displacement per Super Module and per region, so these are the parameters that will be used for future data reprocessing.

	Displacement (mm)		
SM	Outer	Middle	Inner
1	-7.7		
2	-8.7		
3	-10.2	-7.7	
4	-10.2	-8.7	-6.8
5	-10.4	-9.3	-7.4
6	-10.0	-8.3	
7	-10.5		
8	-7.9		

Table 4.7 – Vertical displacement per Super Module and per region.

4.6 Conclusions on the SPD calibration

Before data from *pp* collisions arrived, the commissioning of the SPD detector with cosmic rays provided an excellent starting point for the calibration of its cells. It showed that the pre-calibration was correct up to the 15% level.

The method to calibrate the SPD detector using tracks from LHC collisions has confirmed the results obtained with cosmic rays and has provided a fine calibration factor for each cell with an associated statistical uncertainty of 1.5%. These fine calibration factors will be used since the start of 2011 data taking.

The fit of the theoretical expression to obtain the correction factors and the number of photoelectrons provides a good description for all the cells. The uncertainty obtained from the fits for the correction factors is smaller than the step width to set the threshold voltage. Finally, there is a good

agreement between the number of photoelectrons obtained from the fit and the number of photoelectrons measured in the test bench with cosmic rays.

The alignment of the SPD with respect to the OT and IT has also been measured for 2010 data. The misalignment observed is explained by a rotation around the Z-axis with opposite sign in the two SPD sides and by a vertical downwards displacement.

The stability of the cell efficiencies with time has also been studied to check if the hard radiation environment affect the performance. With data taken in mid 2011, it has been found that the decrease in the cell efficiency is 0.3% overall in a period of four months. However, the origin of this decrease can be due to the degradation of the detector due to the harsh environment, or to the different performance of the reconstruction algorithms overtime, as the running conditions have been changing in 2011.

Besides, as the detector has been opened and closed during the winter shut-down periods, the alignment of the detector may have changed. The differences observed in the alignment after opening and closing the detector, are less than 10%, so they can be neglected.

5

Measurement of the CP asymmetry in $B^0 \to K^{*0}\gamma$ decays

The main goal of this work is to measure the direct *CP* asymmetry in the $B^0 \to K^{*0}\gamma$ decays. The SM prediction for the asymmetry on this channel is very small, which makes this measurement specially interesting as any large value could indicate the presence of physics beyond the SM. The chapter starts by motivating the measurement with the current theoretical and experimental results, as well as by describing briefly some models that predict enhancements on the *CP* asymmetry. Then, the selection of the events and the characterisation of the signal and background components is treated. Finally, the relation between the physical asymmetry and the raw asymmetry measured in the data is given, and the necessary corrections are taken into account to provide a measurement.

5.1 Introduction

In the SM, the decay $B^0 \to K^{*0}\gamma$ —and its charged conjugated— proceed at leading order through the $b \to s\gamma$ one-loop electromagnetic-penguin transition, dominated by a virtual intermediate top quark coupling to a W boson as shown in Fig. 5.1. Extensions of the SM predict additional one-loop contributions that can introduce sizeable effects on the probability and dynamics of the transition [89]. The precise determination of the branching fractions, asymmetries and angular distributions of the radiative decays is a powerful probe for the indirect search of new physics phenomena.

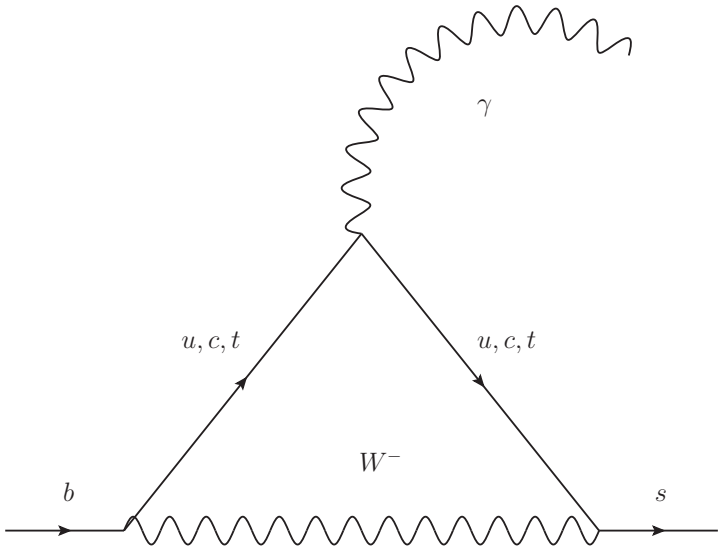

Figure 5.1 – The $b \to s\gamma$ electromagnetic-penguin transition.

The direct *CP* asymmetry in the $B^0 \to K^{*0}\gamma$ decay is defined as

$$A_{CP} = \frac{\Gamma(\overline{B}^0 \to \overline{f}) - \Gamma(B^0 \to f)}{\Gamma(\overline{B}^0 \to \overline{f}) + \Gamma(B^0 \to f)}\,, \tag{5.1}$$

and, in general, the theoretical calculations depend less on hadronic form factors —than, for example, in branching fractions— as many uncertainties cancel in the ratio. In this way, the comparison of *CP* asymmetries in the SM with the experimental results is an effective way of searching effects beyond the SM.

5.1.1 Current theoretical status

In the SM, radiative decays are dominated by a single amplitude from the $O_{7\gamma}$ operator. To have a sizeable *CP* asymmetry, at least two amplitudes with non-vanishing relative weak and strong phase must interfere. This makes that the direct *CP* asymmetry of the $B^0 \to K^{*0}\gamma$ decay is expected to be small within the SM. The SM prediction of the direct *CP* violation in the $B^0 \to K^{*0}\gamma$ decay is [90],

$$A_{CP} = \frac{\Gamma(\bar{B} \to \bar{K}^*\gamma) - \Gamma(B \to K^*\gamma)}{\Gamma(\bar{B} \to \bar{K}^*\gamma) + \Gamma(B \to K^*\gamma)} = (-0.61 \pm 0.43)\%\,. \tag{5.2}$$

Scenarios beyond the SM, can present extra contributions that may interfere with the $O_{7\gamma}$ operator, leading to an enhanced *CP* asymmetry [91–94].

In particular, Super Symmetric extensions of the SM, predict additional $C_7^{\rm SUSY}$ and $C_8^{\rm SUSY}$ gluino-mediated Flavour Changing Neutral Current (FCNC) contributions which can lead to an enhancement of the *CP* asymmetry while keeping the same value for the branching fraction of the decay. Some of these extensions are sensitive to the squark mixing parameter $(\delta^d_{23})_{LR} = \rho e^{i\phi}$ that introduces an extra source of *CP* violation, as well as to the mass ratio of the gluino and squark $x = m^2_{\tilde{g}}/m^2_{\tilde{q}}$. Thus, precise measurements of the *CP* asymmetry can help to constrain the parameter space of these models.

On a model independent approach [94], it has been shown that a *CP* asymmetry exceeding 10%, would be a strong hint towards enhanced chromomagnetic dipole transitions caused by some new flavour physics at high scales. This is the case for models that contain new neutral scalars and vector-like quarks, or others with techniscalars, in which large values for the *CP* asymmetry in a wide range of their parameter space are predicted. An enhancement of the electroweak penguin operator is also predicted for models with charged Higgs-top or Higgsino-stop couplings, for instance. However, the asymmetries predicted in these models can only be at the few percent level, due to constrains on the branching ratio of the $b \to s\gamma$ transitions.

5.1.2 Current experimental status

Radiative decays of the B^0 meson were first observed by the CLEO collaboration in 1993 [95] through the decay mode $B^0 \to K^{*0}\gamma$. Precise measurements of the branching fraction of this decay have been performed by the $B-$factories during the last decade.

The direct *CP* asymmetry in a $b \to s\gamma$ transition was first measured by the CLEO collaboration in 1999 [96]. The most precise measurement to date in the $B^0 \to K^{*0}\gamma$ decay, $A_{CP}(B^0 \to K^{*0}\gamma) = (-1.6 \pm 2.2 \pm 0.7)\%$ [29, 97] is from the BaBar collaboration and it is statistically limited. The current experimental status is summarised in Table 5.1.

The first measurement of LHCb concerning radiative $B-$meson decays has been the ratio of branching fractions of $B^0 \to K^{*0}\gamma$ with respect to $B^0_s \to \phi\gamma$ [99]. This measurement has provided the world best measurement of the branching fraction of the $B^0_s \to \phi\gamma$, and has proved the capabilities of the LHCb detector to produce high-quality results of physics involving photons in the final state.

Besides, the potential of LHCb to perform measurements requiring larger data samples has been extensively studied on simulated data in [55]. The feasibility of a measurement of the photon polarisation in $B^0_s \to \phi\gamma$ decays with first years of data has also been addressed [100].

Experiment	$A_{CP}(B^0 \to K^{*0}\gamma)$
CLEO	$(+8 \pm 13 \pm 3)\%$
BaBar	$(-1.6 \pm 2.2 \pm 0.7)\%$
Belle	$(+1.5 \pm 4.4 \pm 1.2)\%$

Table 5.1 – Status of the current measurements of the direct *CP* asymmetry in $B^0 \to K^{*0}\gamma$ decays from CLEO [96], BaBar [97] and Belle [98] collaborations.

5.2 Data sample and software versions

5.2.1 Real data

The analysis presented in this thesis is performed on the data collected by the LHCb experiment at $\sqrt{s} = 7\,\text{TeV}$ during 2011, corresponding to $1.0\,\text{fb}^{-1}$. Given the integrated luminosity, the measured branching fractions and the $b\bar{b}$ production cross-section at LHC [101], the approximate number of signal events produced in the detector acceptance is 1.5 million, where the trigger, reconstruction and selection efficiencies are not taken into account.

Collected data have been reprocessed using the Reco12 version of the reconstruction configuration, and the Stripping17 configuration of the stripping selection. Reconstruction has been performed with Brunel v41r1 and Stripping with DaVinci v29r1.

5.2.2 Monte Carlo simulation

Signal and background studies have been performed on simulated samples, mostly corresponding to the MC11 simulation campaign. In order to mimic as much as possible the running conditions of the bulk of data from 2011, the mean number of visible interactions per crossing is set to $\nu = 2.0$ in the MC11 series. For $B^0_s \to K^+\pi^-\pi^0$ decays, MC10 samples have been used. Table 5.2 summarises the statistics of the simulated samples used in the analysis.

5.3 Event selection

The event selection of the $B^0 \to K^{*0}\gamma$ candidates is done in three steps, namely

Decay channel	statistics ($\times 10^6$)
$B^0 \to K^{*0}\gamma$	7.55
$B^+ \to K^{*0}\pi^+\gamma$	2.01
$\Lambda_b \to \Lambda_{1520}\gamma$	0.49
$\Lambda_b \to \Lambda_{1670}\gamma$	1.00
$B^0 \to \pi^+\pi^-\pi^0$	1.11
$B^0 \to K^{*0}e^+e^-$	4.01
$B^0 \to K^+\pi^-\pi^0$	2.00
$B_s^0 \to K^+\pi^-\pi^0$	2.16

Table 5.2 – Simulated signal (top) and background (bottom) dataset statistics used in the analysis. All samples have been generated at $\sqrt{s} = 7\,\text{TeV}$ and reconstructed using the same stripping version as for the data.

- The trigger selection.
- The stripping selection.
- The offline selection.

The trigger selection is performed in the LHCb trigger system described in Sec. 3.3, while the stripping and offline selection are done in the offline system detailed in Sec. 3.4.2.

5.3.1 Trigger strategy

The radiative candidates are reconstructed from a sample of events passing a definite trigger path for $B^0 \to K^{*0}\gamma$ decays. At L0, the event must have been triggered by an ECAL candidate with $E_T > 2.5\,\text{GeV}$. At HLT1 events are selected when a good track is reconstructed with IP $\chi^2 > 16$. The IP χ^2 is defined as the difference between the χ^2 of the reconstructed PV fit with and without the considered track. Then, charged tracks are required to have either $p_T > 1.7\,\text{GeV}/c$ for a photon with $E_T > 2.5\,\text{GeV}/c$ or $p_T > 1.2\,\text{GeV}/c$ for a photon with $E_T > 4.2\,\text{GeV}/c$. At HLT2 a track passing the HLT1 criteria must form a K^{*0} candidate when combined with an additional track, and the invariant mass of the combination of the K^{*0} candidate and the photon candidate is requested to lie within a $\pm 1\,\text{GeV}/c^2$ window around the world average B^0 mass. In order to control the trigger efficiencies, the photon and

the vector meson daughters of the reconstructed candidates are required to explicitly be involved in the event triggering at both L0 and HLT steps [99].

5.3.2 Stripping

After having been triggered and stored, the events are reconstructed and stripped in order to reduce the computing time spent by the users and the storage capacity required. The *Radiative* stream of the LHCb stripping is designed as a set of lines, each of which performs an exclusive selection of a radiative B decay. In Stripping17, $B^0 \to K^{*0}\gamma$ decays are selected performing an offline-like selection with looser requirements.

The selection asks for good-quality tracks with $\chi^2 < 5$ and ensures that tracks do not point to any PV by requiring IP $\chi^2 > 10$. The invariant mass of the K^{*0} candidate needs to be on a window of $< 100\,\mathrm{MeV}/c^2$ around the K^{*0} world average mass and has to have a vertex-fit $\chi^2 < 15$. Photons with $E_T > 2600\,\mathrm{GeV}/c$ are combined with K^{*0} candidates to form a B^0 meson with a mass lying in a window of $< 1\,\mathrm{GeV}/c^2$ around the world average B^0 mass. Moreover, the B^0 candidates are required to point to a primary vertex by requiring IP $\chi^2 < 15$. Also, the angle between the direction of flight of the B^0 meson, formed with the primary and secondary vertexes, and the sum of the momentum of its decay products (DIRA), has to be small DIRA $< 0.02\,\mathrm{rad}$. The stripping criteria are reported in Table 5.3. In addition, several monitoring lines have been devised, allowing to access parts of the dataset that would otherwise be cut by the Stripping selection, for instance, the K^{*0} or B^0 sidebands.

	$B^0 \to K^{*0}\gamma$
Track IP χ^2	>10
Track χ^2	< 5
K^{*0} ΔM_{PDG} (MeV/c^2)	$< 100(150)$
K^{*0} vertex χ^2	< 15
E_{T_γ} (MeV/c)	>2600
B IP χ^2	< 15
B DIRA (rad)	$< 0.02(0.06)$
ΔM_{PDG} B (MeV/c^2)	$< 1000(2000)$

Table 5.3 – Stripping criteria applied in the radiative stream. Requirements in the monitoring lines are given in parentheses.

5.3.3 Offline selection

Candidates are selected using a cut-based selection, with the value of the cuts chosen to maximise the signal significance [102] $\frac{S}{\sqrt{S+B}}$, where S and B are the number of signal and background events, respectively. Signal candidates come from a simulated sample of $B^0 \to K^{*0}\gamma$ decays, and background is considered to be simulated $b\bar{b}$-inclusive events with at least one b quark inside the detector acceptance.

The B^0 mesons are reconstructed from a selected K^{*0}, built from oppositely charged kaon-pion pairs, combined with a photon. The two charged tracks used to build the vector meson are required to have $p_T > 500\,\text{MeV}/c$ and at least one among them to have $p_T > 1200\,\text{MeV}/c$. In addition, a requirement of IP $\chi^2 > 25$ means that charged tracks must be incompatible with coming from any PV. The identification of the kaon and pion tracks is made by applying requirements to the PID provided by the RICH system. The PID is based on the comparison between two particle hypotheses, and it is represented by the difference in logarithms of the likelihoods (DLL) between the two hypotheses

$$\begin{aligned} \text{DLL}_{\text{K}\pi} &= \text{LL}_K - \text{LL}_\pi \\ \text{DLL}_{\text{Kp}} &= \text{LL}_K - \text{LL}_p\,. \end{aligned} \tag{5.3}$$

Kaons are required to have $\text{DLL}_{\text{K}\pi} > 5$ and $\text{DLL}_{\text{Kp}} > 2$, while pions are required to have $\text{DLL}_{\text{K}\pi} < 0$. With these criteria, kaons (pions) coming from the signal channel are identified with a $\sim 70\,(83)\,\%$ efficiency for a $\sim 3\,(2)\,\%$ pion (kaon) contamination.

Two-track combinations are accepted as K^{*0} candidates if they form a vertex with $\chi^2 < 9$ and if their invariant mass lies within a $\pm 50\,\text{MeV}/c^2$ mass window of the world average K^{*0} mass. The resulting vector meson candidate is combined with a photon of $E_T > 2.6\,\text{GeV}/c$. Neutral and charged electromagnetic clusters in the ECAL are separated based on their compatibility with extrapolated tracks [72]. The difference in likelihoods for the photon and electron hypothesis are transformed into a confidence-level variable (CL_γ) distributed in the range [0,1], defined as

$$\text{CL}_\gamma = \frac{\tanh(\Delta \ln \mathcal{L}) + 1}{2}\,. \tag{5.4}$$

Photon candidates are required to have $\text{CL}_\gamma > 0.25$.

The photon and merged-π^0 deposits are identified on the basis of the shapes of the electromagnetic shower in the ECAL [103, 104]. The B^0 candidate invariant-mass resolution is dominated by the photon energy resolution and is $\sim$100 MeV/c^2.

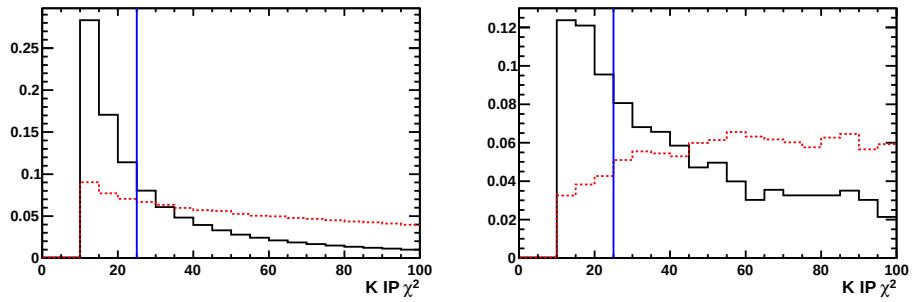

Figure 5.2 – Distribution of the IP χ^2 of kaons before (left) and after (right) the offline selection without the IP χ^2 of kaons requirement applied. The red dashed histogram corresponds to $B^0 \to K^{*0}\gamma$ simulated data, the solid black histogram is real collision data and the vertical blue line is the offline selection cut.

B^0 candidates are required to have an invariant mass within a $1\,\text{GeV}/c^2$ window around the world average mass, to have $p_T > 3\,\text{GeV}/c$ and to point to a pp interaction vertex by applying a cut at $\text{IP}\chi^2 < 9$. In addition, the combinatorial background is further reduced by requiring the flying distance (FD) of the B mesons to have $\chi^2(\text{FD}) > 100$.

The helicity angle of the decay is defined as the angle between the momentum of any of the daughters of the K^{*0} and the momentum of the B^0 candidate, in the rest frame of the K^{*0}. For the $B^0 \to K^{*0}\gamma$ decay, the distribution of the helicity angle is expected to follow a $\sin^2\theta_H$ function and for $B^0 \to K^{*0}\pi^0$ background decays, it is expected to follow a $\cos^2\theta_H$ function. This is exploited to remove $B^0 \to K^{*0}\pi^0$ background, in which the neutral pion is misidentified as a photon, by requiring that $|\cos\theta_H| < 0.8$.

Background coming from partially reconstructed $b-$hadron decays is rejected by requiring vertex isolation: the χ^2 of the B^0 vertex must increase by more than two units when adding any other track in the event. The selection requirements applied to $B^0 \to K^{*0}\gamma$ candidates are listed in Table 5.4.

The normalised distributions of the variables used in the selection for the simulated samples and real data are shown in Figs. 5.2-5.16. In order to understand the effect of each requirement, the distributions are extracted applying the full offline selection with the exception of the requirement under study.

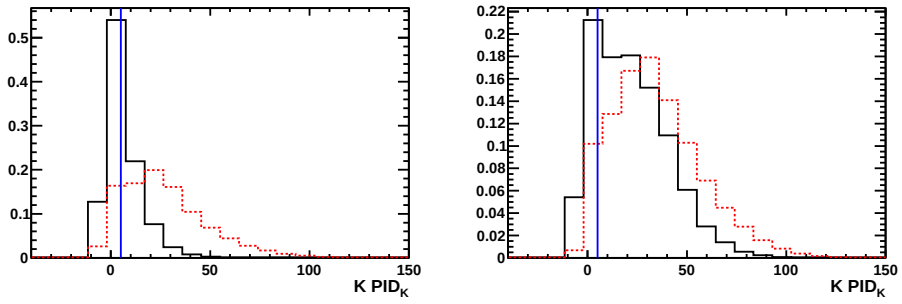

Figure 5.3 – Distribution of the $\mathrm{DLL_{K\pi}}$ of kaons before (left) and after (right) the offline selection without the kaon $\mathrm{DLL_{K\pi}}$ requirement applied. The red dashed histogram corresponds to $B^0 \to K^{*0}\gamma$ simulated data, the solid black histogram is real collision data and the vertical blue line is the offline selection cut.

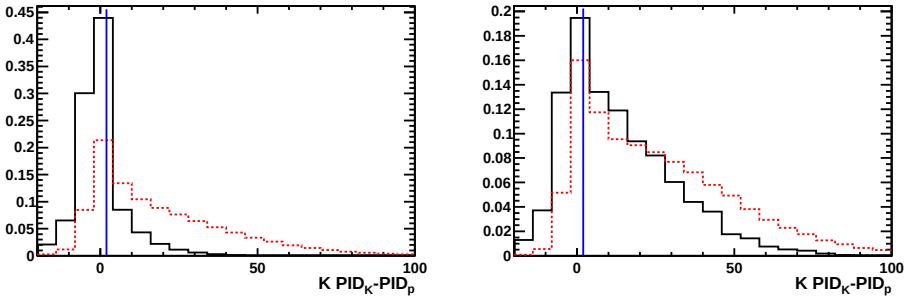

Figure 5.4 – Distribution of the $\mathrm{DLL_{Kp}}$ of kaons before (left) and after (right) the offline selection without the kaon $\mathrm{DLL_{Kp}}$ requirement applied. The red dashed histogram corresponds to $B^0 \to K^{*0}\gamma$ simulated data, the solid black histogram is real collision data and the vertical blue line is the offline selection cut.

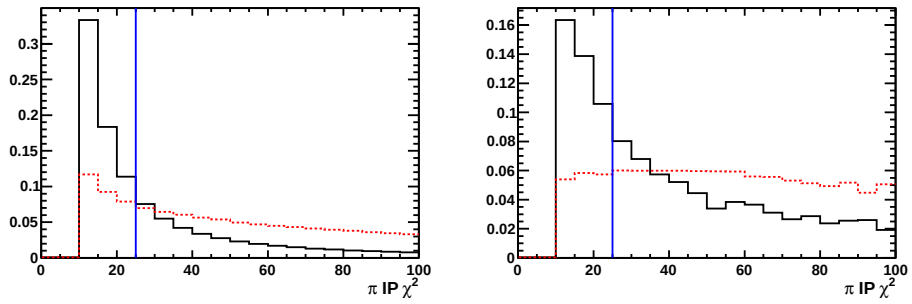

Figure 5.5 – Distribution of the IP χ^2 of pions before (left) and after (right) the offline selection without the IP χ^2 of pions requirement applied. The red dashed histogram corresponds to $B^0 \to K^{*0}\gamma$ simulated data, the solid black histogram is real collision data and the vertical blue line is the offline selection cut.

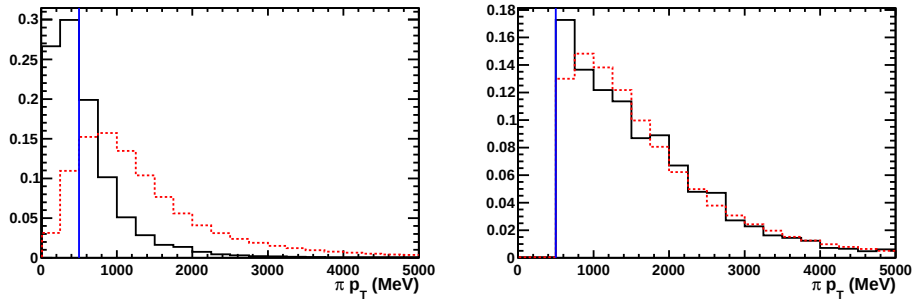

Figure 5.6 – Distribution of the p_T of pions before (left) and after (right) the offline selection without the p_T of pions requirement applied. The red dashed histogram corresponds to $B^0 \to K^{*0}\gamma$ simulated data, the solid black histogram is real collision data and the vertical blue line is the offline selection cut.

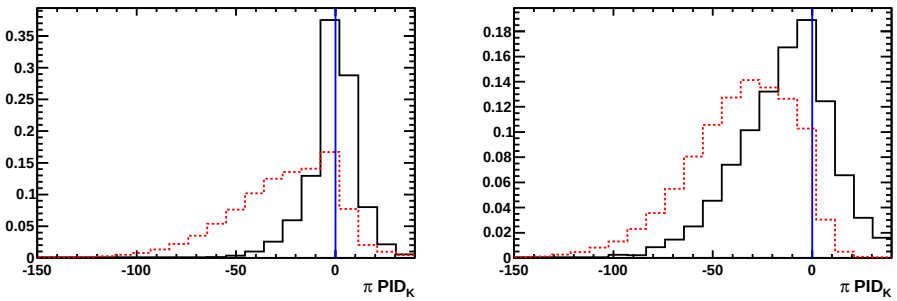

Figure 5.7 – Distribution of the $\mathrm{DLL}_{\mathrm{K}\pi}$ of pions before (left) and after (right) the offline selection without the pion $\mathrm{DLL}_{\mathrm{K}\pi}$ requirement applied. The red dashed histogram corresponds to $B^0 \to K^{*0}\gamma$ simulated data, the solid black histogram is real collision data and the vertical blue line is the offline selection cut.

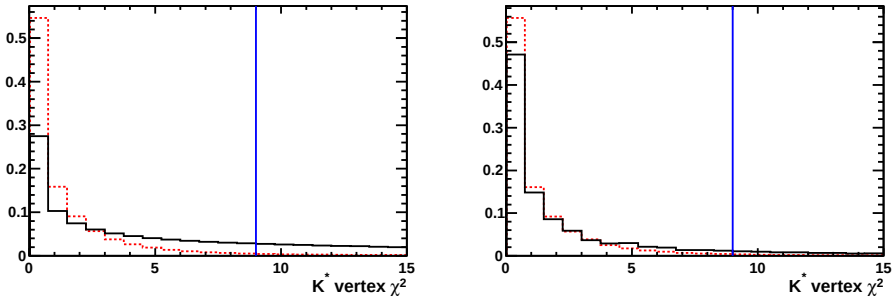

Figure 5.8 – Distribution of the vertex χ^2 of K^{*0} candidates before (left) and after (right) the offline selection without the K^{*0} vertex-χ^2 requirement applied. The red dashed histogram corresponds to $B^0 \to K^{*0}\gamma$ simulated data, the solid black histogram is real collision data and the vertical blue line is the offline selection cut.

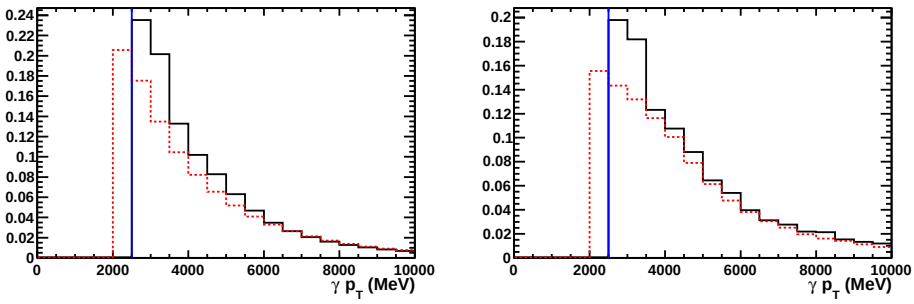

Figure 5.9 – Distribution of the p_T of photons before (left) and after (right) the offline selection without the photon p_T requirement applied. The red dashed histogram corresponds to $B^0 \to K^{*0}\gamma$ simulated data, the solid black histogram is real collision data and the vertical blue line is the offline selection cut.

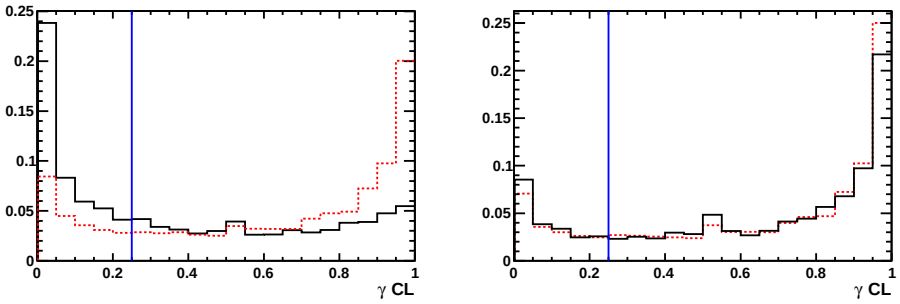

Figure 5.10 – Distribution of the confidence level (CL) of photons before (left) and after (right) the offline selection without the photon CL requirement applied. The red dashed histogram corresponds to $B^0 \to K^{*0}\gamma$ simulated data, the solid black histogram is real collision data and the vertical blue line is the offline selection cut.

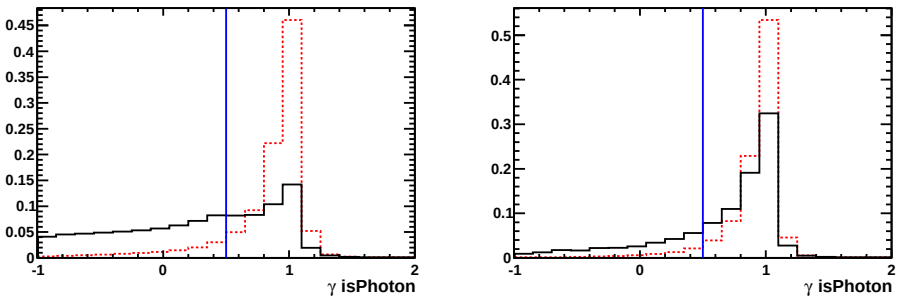

Figure 5.11 – Distribution of the γ/π^0 separation variable before (left) and after (right) the offline selection without the separation requirement applied. The red dashed histogram corresponds to $B^0 \to K^{*0}\gamma$ simulated data, the solid black histogram is real collision data and the vertical blue line is the offline selection cut.

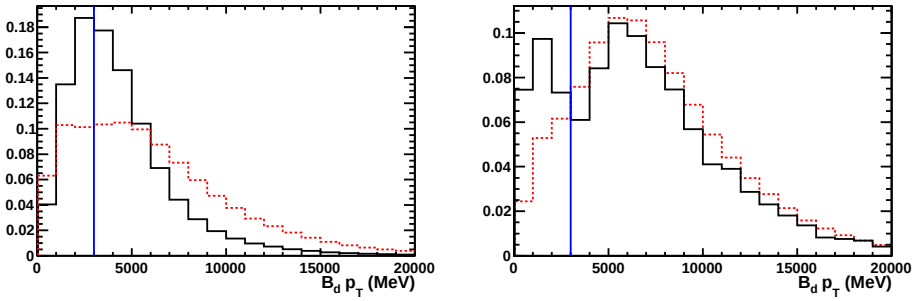

Figure 5.12 – Distribution of the p_T of B^0 candidates before (left) and after (right) the offline selection without the p_T of B^0 candidates requirement applied. The red dashed histogram corresponds to $B^0 \to K^{*0}\gamma$ simulated data, the solid black histogram is real collision data and the vertical blue line is the offline selection cut.

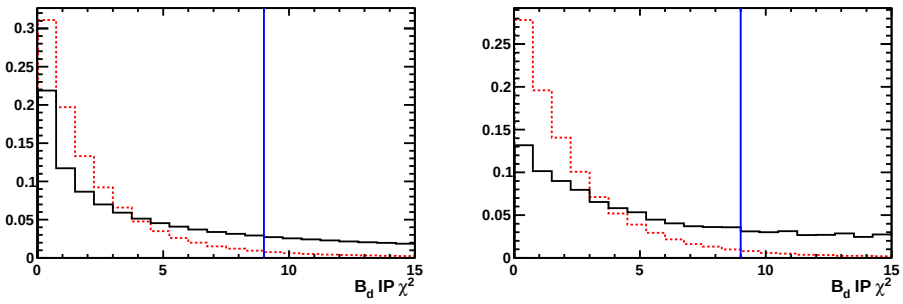

Figure 5.13 – Distribution of the IP χ^2 of B^0 candidates before (left) and after (right) the offline selection without the IP χ^2 of B^0 requirement applied. The red dashed histogram corresponds to $B^0 \to K^{*0}\gamma$ simulated data, the solid black histogram is real collision data and the vertical blue line is the offline selection cut.

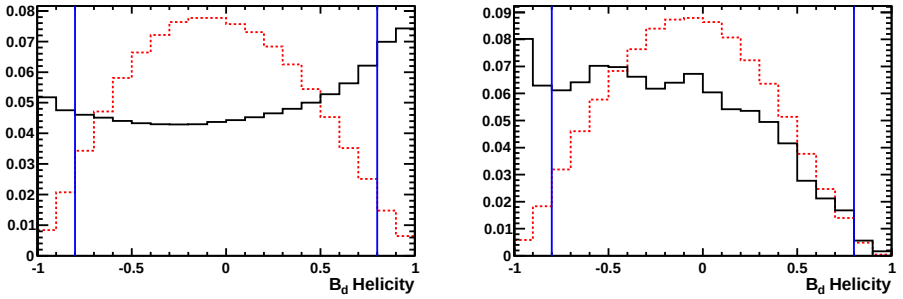

Figure 5.14 – Distribution of the helicity angle of B^0 candidates before (left) and after (right) the offline selection without the helicity angle requirement applied. The red dashed histogram corresponds to $B^0 \to K^{*0}\gamma$ simulated data, the solid black histogram is real collision data and the vertical blue line is the offline selection cut.

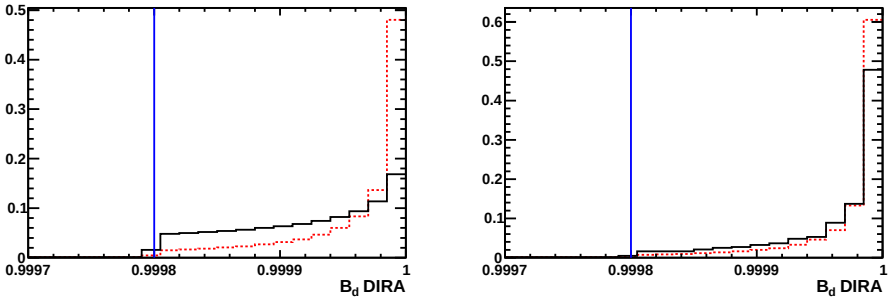

Figure 5.15 – Distribution of the DIRA of B^0 candidates before (left) and after (right) the offline selection without the DIRA requirement applied. The red dashed histogram corresponds to $B^0 \to K^{*0}\gamma$ simulated data, the solid black histogram is real collision data and the vertical blue line is the offline selection cut.

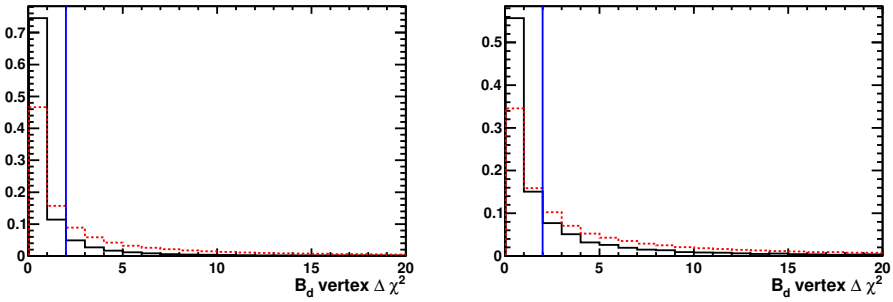

Figure 5.16 – Distribution of the vertex isolation variable of B^0 candidates before (left) and after (right) the offline selection without the vertex isolation requirement applied. The red dashed histogram corresponds to $B^0 \to K^{*0}\gamma$ simulated data, the solid black histogram is real collision data and the vertical blue line is the offline selection cut.

		$B^0 \to K^{*0}\gamma$
Track IP χ^2		> 25
$p_{T,\text{track}}$	(MeV/c)	> 500
$\max(p_{T,\text{tracks}})$	(MeV/c)	> 1200
K $\text{DLL}_{\text{K}\pi}$		> 5
K DLL_{Kp}		> 2
π $\text{DLL}_{\text{K}\pi}$		< 0
K^{*0} ΔM_{PDG}	(MeV/c^2)	< 50
K^{*0} vertex χ^2		< 9
γ E_T	(MeV/c)	> 2600
γ CL_γ		> 0.25
π^0/γ separation		> 0.5
B p_T	(MeV/c)	> 3000
B IP χ^2		< 9
B helicity		< 0.8
B isolation $\Delta\chi^2$		> 2.0
B flying distance χ^2		> 100

Table 5.4 – Selection requirements applied to $B^0 \to K^{*0}\gamma$ candidates. The requirements are divided in sections, which in order are: track requirements, PID requirements, vector meson requirements, photon requirements and B candidate requirements.

5.4 Signal characterisation

5.4.1 Invariant-mass fit

The expected mass shape for signal and background have been studied using the simulated samples listed in Table 5.2. As the invariant-mass resolution of the radiative decays is dominated by the ECAL resolution, special care has been taken regarding the reliability of the simulation to reproduce the actual calorimeter performance. A 2% Gaussian smearing has been added to the reconstructed energy of the simulated photon to reproduce the $B^0 \to K^{*0}\gamma$ signal resolution. This additional factor is in good agreement with the performance achieved by the ECAL calibration procedure based on large

samples of π^0 decays [105].

A significant ageing of the ECAL response has been experienced along the 2011 data taking period. The observed decrease in the gain has been continuously monitored using the π^0 peak position, and a set of time-dependent cell-by-cell corrections have been applied in the data reconstruction processing. This ageing correction was, however, not applied in the online HLT processing. As a result, the resolution on the kinematic parameters of the signal is improving at each step of the data-flow, from HLT and stripping processing to the final offline analysis. As the same $\pm 1\,\mathrm{GeV}/c^2$ mass window is applied on B candidates in HLT2, stripping and offline selections, the different resolutions results in an acceptance bias in the vicinity of the corrected mass-window borders. The acceptance is modelled by adding a 3-parameter threshold function in the mass fit model

$$T(m_B) = \left(1 - \mathrm{erf}\left(\frac{m_B - t_\mathrm{L}}{\sqrt{2}\sigma_\mathrm{d}}\right)\right) \times \left(1 - \mathrm{erf}\left(\frac{t_\mathrm{U} - m_B}{\sqrt{2}\sigma_\mathrm{d}}\right)\right), \tag{5.5}$$

where erf is the Gauss Error Function. The parameter $t_\mathrm{L}(t_\mathrm{U})$ represents the actual lower (upper) threshold on the corrected mass and σ_d represents the quadratic difference between uncorrected and corrected masses.

5.4.2 Signal shape

The invariant-mass distribution of the K^{*0} meson is described by a relativistic P-wave Breit-Wigner distribution [106, 107] defined as,

$$\mathrm{BW}(m) = \frac{m m_0 \Gamma(m)}{\left(m_0^2 - m^2\right)^2 + \left(m_0 \Gamma(m)\right)^2} \tag{5.6}$$

$$\Gamma(m) = \Gamma_0 \left(\frac{q}{q_0}\right)^{2l+1} \frac{m_0}{m}, \tag{5.7}$$

where $\Gamma_0 = \Gamma(m_0)$ is the natural width of the K^{*0} resonance, $q(m)$ is the momentum of the decay products in the rest frame of the mother particle, and it is defined as

$$q(m) = \frac{\sqrt{m^2 - (m_K + m_\pi)^2}\sqrt{m^2 - (m_K - m_\pi)^2}}{2m}, \tag{5.8}$$

being $q_0 = q(m_0)$, and $l = 1$ is the angular momentum transferred. The natural width of the resonance is fixed to the world average value [29]. To account

for any possible effect due to the detector resolution, the Breit-Wigner distribution is convoluted with a Gaussian distribution with resolution σ. A polynomial shape is used to describe the present background. The invariant-mass distribution is shown in Fig. 5.17 together with the fitted function.

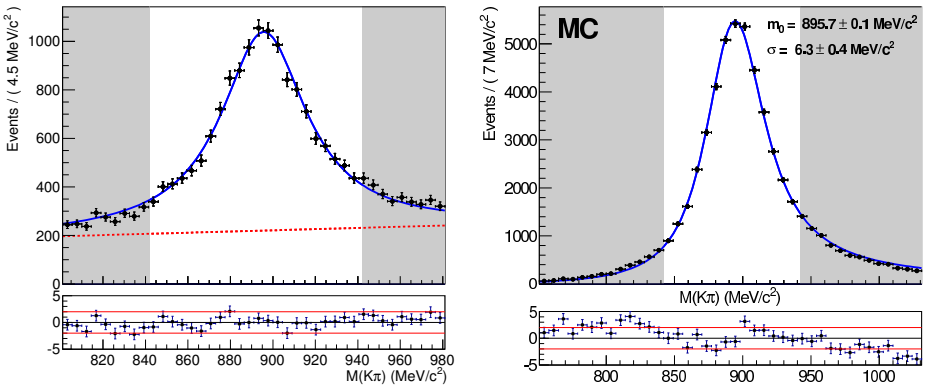

Figure 5.17 – Invariant-mass distribution of the K^{*0} resonance candidates from real data (left) and simulation (right). The black points represent the data and the fit result is represented as a solid blue line. The regions outside the vector meson invariant-mass window are shaded. The fit function is described in the text. The Poisson χ^2 residuals [108] are shown below the fits with the ± 2 confidence-level interval delimited by solid red lines.

The fit on data of the invariant mass of the K^{*0} yields a resonance mass of $m_{\text{data}} = 895.7 \pm 0.4\,\text{MeV}/c^2$, in agreement with the world average [29]. The detector resolution extracted from the fit is $\sigma_{\text{data}} = 5 \pm 4\,\text{MeV}/c^2$. For the simulation, the K^{*0} invariant-mass value is $m_{\text{sim}} = 895.7 \pm 0.1\,\text{MeV}/c^2$, which agrees with the data. The detector resolution extracted from the simulation is $\sigma_{\text{sim}} = 6.3 \pm 0.4\,\text{MeV}/c^2$, which also agrees with the result from real data.

Based on the $B^0 \to K^{*0}\gamma$ simulated samples, two contributions in the B^0 signal mass shape have been considered:

- In the low mass region, possible losses in the photon energy due to the fiducial volume of the calorimeter have been accounted for by making use of the Crystal-Ball (CB) distribution. It consists of a Gaussian core and a power-law tail below a certain threshold, and it is given by

$$f(x;\alpha,n,\bar{x},\sigma) = N \times \begin{cases} \exp(-\frac{(x-\bar{x})^2}{2\sigma^2}), & \text{for } \frac{x-\bar{x}}{\sigma} > -\alpha \\ A \times (B - \frac{x-\bar{x}}{\sigma})^{-n}, & \text{for } \frac{x-\bar{x}}{\sigma} \leq -\alpha\,, \end{cases} \tag{5.9}$$

where A and B are

$$A = \left(\frac{n}{|x|}\right)^n \exp\left(-\frac{\alpha^2}{2}\right) \tag{5.10}$$

$$B = \frac{n}{|\alpha|} - |\alpha| \,. \tag{5.11}$$

- A tail at high masses has been observed in several analyses and can be partially explained by the spread in the uncertainty of the reconstructed B-meson mass. Large pile-up deposits in the ECAL cluster forming the photon candidate are also likely to contribute. This high mass tail can be parametrised by a CB distribution with $\alpha < 0$.

parameter	$B^0 \to K^{*0}\gamma$
$\mu\,(\,\mathrm{MeV}/c^2)$	5278.6 ± 0.6
$\sigma\,(\,\mathrm{MeV}/c^2)$	92.8 ± 0.5
n_{left}	0.99 ± 0.07
α_{left}	2.14 ± 0.06
n_{right}	7 ± 2
α_{right}	-1.10 ± 0.20
f	0.71 ± 0.04

Table 5.5 – Fit results for the simulated $B^0 \to K^{*0}\gamma$ decays.

Taking the two contributions into account, the B^0 meson signal shape is parametrised as the sum of two CB distributions with a common mean position μ and width σ, and different tail parameters. The relative fraction of the CB accounting for the low mass tail is described by f. The result of the fit to the $B^0 \to K^{*0}\gamma$ invariant-mass distribution from simulation is displayed in Fig. 5.18. The values of the fit parameters are reported in Table 5.5.

5.5 Background composition

A detailed study of the background sources is conducted using large samples of simulated data. Significant contaminations from different specific sources are identified, essentially from other mis-reconstructed radiative B decays

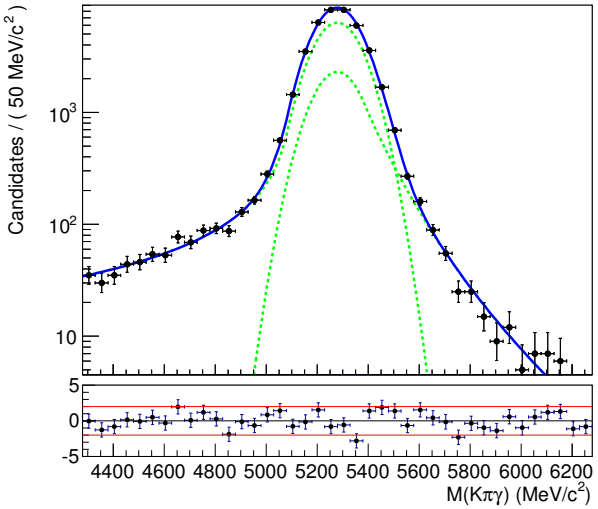

Figure 5.18 – Invariant-mass distribution for the $B^0 \to K^{*0}\gamma$ candidates reconstructed from simulation. The distribution is fitted with a double-sided Crystal-Ball function. The Poisson χ^2 residuals [108] are shown below the fits with the ± 2 confidence-level interval delimited by solid red lines.

or other charmless decays involving energetic π^0. The mis-identified $B \to h^+h^-\gamma$ and $B \to h^+h^-\pi^0$ decays produce background contributions mostly peaking under the signal peak. Partially reconstructed decays such as $B \to h^+h^-\gamma X$ and $B \to h^+h^-\pi^0 X$, produce a peaked background at lower masses with a large tail contaminating the signal region. The overall amplitude of these partially reconstructed decays is poorly known, and possibly reaches few percent of the signal yield in the entire $\pm 1\,\mathrm{GeV}/c^2$ window around the B^0 mass. The various contaminations are summarised in Table 5.6 and each contribution is discussed in detail in the following subsections.

Unless stated otherwise, the relative contamination to the $B^0 \to K^{*0}\gamma$ signal from the considered b-hadron decay, $H_b \to X$, is evaluated using

$$C_{H_b\to X} = \frac{N^{\mathrm{sel}}(H_b \to X)}{N^{\mathrm{sel}}(B^0 \to K^{*0}\gamma)} = \frac{\epsilon_{\mathrm{MC}}(H_b \to X)}{\epsilon_{\mathrm{MC}}(B^0 \to K^{*0}\gamma)} \times \frac{f_{H_b}}{f_d} \times \frac{\mathcal{B}(H_b \to X)}{\mathcal{B}(B^0 \to K^{*0}\gamma)}\,, \tag{5.12}$$

where ϵ_{MC} is the total efficiency from the simulation including decay acceptance and trigger, $\frac{f_{H_b}}{f_d}$ is the b-quark hadronisation rate into the b-hadron H_b, relative to the B^0 [111], and $\mathcal{B}(H_b \to X)/\mathcal{B}(B^0 \to K^{*0}\gamma)$ is the branching fraction of the studied background relative to the $B^0 \to K^{*0}\gamma$ decay. The branching fractions of the charmless B_s^0 and Λ_b decays are unknown.

	Branching fraction $\times 10^6$	Relative contamination to $B^0 \to K^{*0}\gamma$
$\Lambda_b \to \Lambda^* \gamma$	estimated from data	$(1.0 \pm 0.3)\%$
$B_s^0 \to K^{*0}\gamma$	1.26 ± 0.31 (theo. [109])	$(0.8 \pm 0.2)\%$
$B^0 \to K^+\pi^-\pi^0$	$35.9^{+2.8}_{-2.4}$ (exp. [110])	$(0.5 \pm 0.1)\%$
$B_s^0 \to K^+\pi^-\pi^0$	estimated from SU(3) symmetry	$(0.2 \pm 0.2)\%$
$B_s^0 \to K^+K^-\pi^0$	estimated from SU(3) symmetry	$\mathcal{O}(10^{-4})$
$B^+ \to K^{*0}\pi^+\gamma$	20^{+7}_{-6} (exp. [110])	$(3.3 \pm 1.1)\%$
$B^+ \to K^+\pi^-\pi^0\gamma$	41 ± 4 (exp. [110])	$\mathcal{O}(5\%)$
$B^+ \to \phi K^+\gamma$	3.5 ± 0.6 (exp. [110])	3×10^{-4}
$B \to K^{*0}\pi^0 X$	$\mathcal{O}(10\%)$ [110]	$\mathcal{O}(1\%)$

Table 5.6 – Relative contaminations expected to the $B^0 \to K^{*0}\gamma$ yield in the $\pm 1\,\mathrm{GeV}/c^2$ mass window from the specific background channels : radiative decays, $h^+h^-\gamma$ (top), charmless b-decays involving energetic π^0, $h^+h^-\pi^0$ (middle) and partially reconstructed decays (bottom). The measured (exp.) or theoretical (theo.) branching fraction is given when available.

5.5.1 Combinatorial background

The mass shape of the combinatorial background is extracted from the low-mass side-band of the K^{*0} meson $M(K^{*0}_{\mathrm{data}}) - M(K^{*0}_{\mathrm{PDG}}) < -100\,\mathrm{MeV}/c^2$ using a dedicated monitoring selection with an enlarged K^{*0} and B^0 mass windows, as explained in Sec. 5.3.2. The invariant-mass distribution of the candidates is found to be consistent with an exponential function as displayed on Fig. 5.19, where the B^0 signal region [5079-5479] MeV/c^2 has been removed from the fit, as a residual signal might still be present. The mass window acceptance is included by multiplying the exponential function by the threshold function discussed in Sec. 5.4.1.

Within the limited statistics present in the pre-scaled monitoring selection, no peaking structure is observed. Furthermore, there is a good matching between the decay constant found in the K^{*0} side-band

$$\tau_{CB} = -1.14 \pm 0.07\,\mathrm{GeV}^{-1}c^2\,, \tag{5.13}$$

and the value obtained when performing the full signal fit as discussed in

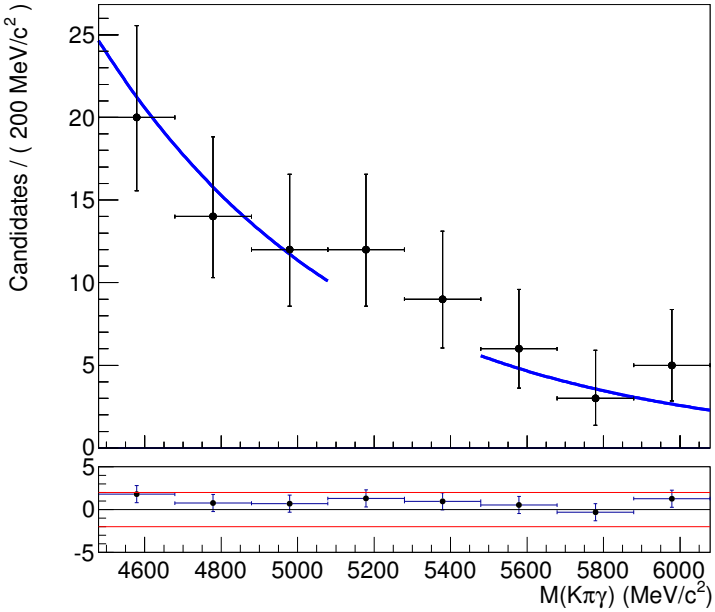

Figure 5.19 – $K\pi\gamma$ invariant-mass shape for the combinatorial background selected in the low-mass K^{*0} invariant-mass side-band. The invariant-mass shape is modelled with a single exponential multiplied by the threshold function discussed in Sec. 5.4.1. The fit is performed without considering the B^0 signal region [5079-5479] MeV/c^2. The Poisson χ^2 residuals [108] are shown below the fits with the ± 2 confidence-level interval delimited by solid red lines.

Sec. 5.6.1.

5.5.2 Partially reconstructed decays

The partial reconstruction of decays $B \to K^{*0}\pi^0$X may provide a sizeable contamination in the low-mass side of the signal region. Although the rejection power of the selection reduces this contribution by a factor 10^6, the remaining contamination may still be significant. A cocktail of several simulated decays has been used to estimate the shape of this background.

Some of the potentially dangerous decays have been scrutinised using a large sample of simulated $B \to h^+h^-\pi^0 X$ decays, where X stands for a single particle or an intermediate state, including the modes

- $B^0 \to D^0(K^+\pi^-\pi^0)K^{*0}(K^+\pi^-)$,
- $B^0 \to \pi^+\pi^-\pi^0 K^0_S(\pi^+\pi^-)$,
- $B^0 \to D^-(K^+\pi^-\pi^-)\rho^+(\pi^+\pi^0)$,

- $B^+ \to K^+K^-K^+\pi^0$,
- $B^+ \to J/\psi\,(\pi^+\pi^-\pi^0)K^+$,
- $B^+ \to K^{*+}(K^+\pi^0)\pi^+\pi^-$.

As shown in Fig. 5.20, these decays produce a peaked shape in the low-mass region, around 4000 MeV/c^2, with a large tail penetrating the signal region. The overall branching fraction of the b-hadron mixture to $K^{*0}\pi^0$X can be of $\mathcal{O}(10\%)$ [29] at low masses.

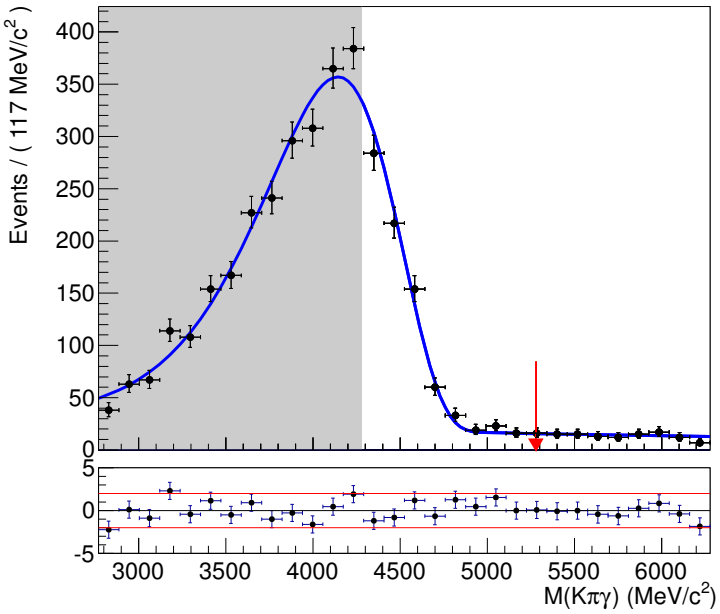

Figure 5.20 – Invariant-mass distribution of the $K^+\pi^-\gamma$ combinations reconstructed in a sample of $B \to h^+h^-\pi^0$X simulated events. The mass distribution is fitted with an Argus function plus an exponential function to model the pure combinatorial component. The shaded region is outside the selection mass window, and the red arrow indicates the position of the signal peak. The Poisson χ^2 residuals [108] are shown below the fits with the ± 2 confidence-level interval delimited by solid red lines.

Charged B decays, $B^+ \to K^{*0}\gamma\pi^+$ are also a dangerous source of contamination. When accompanied with a non-reconstructed soft π^+, these decays exhibit a final state topology very similar to the signal with a branching fraction of the same magnitude. Several variables used in the signal selection are designed to fight against these partially reconstructed B decays, in particular the angle of the B momentum with respect to its flight direction —provided

by the primary and the decay vertices— as well as the isolation of the K^{*0} decay vertex that reduces by a factor 2.5 their contamination. These decays produce a peaked background around 5000 MeV/c^2, competing with the left tail of the $B^0 \to K^{*0}\gamma$ signal, as shown on Fig. 5.21. Using simulated data and the measured branching fraction $\mathcal{B}(B^+ \to K^{*0}\gamma\pi^+) = (20^{+7}_{-6}) \times 10^{-6}$ [110], the relative contamination of $B^+ \to K^{*0}\ \gamma\ \pi^+$ to $B^0 \to K^{*0}\gamma$ in the ± 1 GeV/c^2 mass window, is estimated to be

$$C_{B^+ \to K^{*0}\gamma\pi^+ / B^0 \to K^{*0}\gamma} = (3.3 \pm 1.1)\% \,. \tag{5.14}$$

Other similar decays also contaminate the signal region with a similar shape. In particular, the $B^0 \to K^{*0}\gamma\pi^0$ decay, for which the vertex isolation criteria has no effect. The measured branching fraction of this decay is $\mathcal{B}(B^0 \to K^{*0}\gamma\pi^0) = (41 \pm 4) \times 10^{-6}$ [110], and assuming the same selection efficiency than $B^+ \to K^{*0}\gamma\pi^+$, the expected relative contamination is $C_{B^0 \to K^{*0}\gamma\pi^0 / B^0 \to K^{*0}\gamma} \sim 5\%$. Other channels, such as $B^0 \to K^{*0}\eta(\gamma\gamma)$, $B^0 \to K^{*0}e^+e^-$ or $B^+ \to \rho e^+\nu$ could also contribute with a similar mass shape.

This means that the overall contamination of these background peaking at around 5000 MeV/c^2 might be of $\mathcal{O}(10\%)$.

5.5.3 Contamination from decays containing a photon

Irreducible contamination from $B^0_s \to \overline{K}^{*0}\gamma$ decays

The branching fraction of this suppressed $b \to d\ \gamma$ transition is predicted to be $\mathcal{B}(B^0_s \to \overline{K}^{*0}\gamma) = (1.26 \pm 0.25 \pm 0.18) \times 10^{-6}$ [109]. As this decay has never been observed experimentally, the contamination of this decay is estimated assuming the theoretical branching fraction value. The contamination to the $B^0 \to K^{*0}\gamma$ yield is

$$C_{B^0_s \to \overline{K}^{*0}\gamma} = \frac{f_s}{f_d} \times \frac{\mathcal{B}(B^0_s \to \overline{K}^{*0}\gamma)}{\mathcal{B}(B^0 \to K^{*0}\gamma)} = (0.8 \pm 0.2)\% \,. \tag{5.15}$$

The mass shape of this contribution is obtained from the $B^0 \to K^{*0}\gamma$ signal shape, shifted by $m_{B^0_s} - m_{B^0} = 87.3 \pm 0.4$ MeV/c^2 [112].

Hadron mis-identification

The contamination due to hadron mis-identification includes two contributions

- The $B^0_s \to \phi\gamma$ contamination to $B^0 \to K^{*0}\gamma$ due to $\pi \to K$ misidentification, which is found to be $\mathcal{O}(10^{-4})$, and thus is neglected.

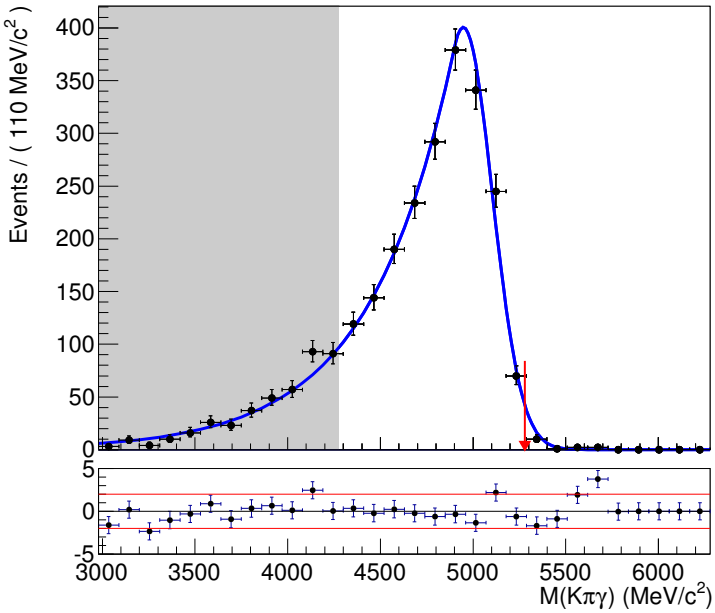

Figure 5.21 – Invariant-mass distribution of the $K^+\,\pi^-\,\gamma$ combinations reconstructed in 2×10^6 $B^+\to K^{*0}\gamma\pi^+$ simulated events. The mass distributions are fitted with a Crystal-Ball function. The shaded region is outside the selection mass window, and the red arrow indicates the position of the signal peak. The Poisson χ^2 residuals [108] are shown below the fits with the ±2 confidence-level interval delimited by solid red lines.

- Multiple candidates. Studies from simulated samples show that the fraction of $B^0 \to K^{*0}\gamma$ events with several reconstructed candidates is expected to be $\mathcal{O}(10^{-4})$. The contamination to the signal yield is also considered to be negligible.

5.5.4 Baryonic radiative decays

The contamination from the radiative decays of b-baryons, $\Lambda_b \to \Lambda\gamma$, is also studied. The Λ_b decay involving the long-living resonance $\Lambda(1115) \to p\pi^-$, exhibits a very different topology from the signal, and it is found to contaminate at a negligible level. On the other hand, the $\Lambda_b \to \Lambda^*(pK^-)\gamma$ decay —which has not been observed yet— where Λ^* stands for the $\Lambda(1520)$ and further massive-baryon resonances promptly decaying into a pK^- final state is found to contaminate the signal significantly. The contamination proceeds via the misidentification of the proton into a pion, which shifts at the same time the Λ_b and the Λ^* reconstructed mass towards the B^0 and the K^{*0} mass regions, respectively.

The invariant-mass distribution of these backgrounds is extracted from a simulated data sample of $\Lambda_b \to \Lambda(1520)\gamma$ and $\Lambda_b \to \Lambda(1670)\gamma$ decays. The contamination to the $B^0 \to K^{*0}\gamma$ can be seen as the peaked shape displayed on Fig. 5.22. The mass shape is modelled with a *CB* distribution, peaking around $5300\,\mathrm{MeV}/c^2$.

The relative contamination to $B^0 \to K^{*0}\gamma$ is given by Eq. 5.12, with the extra factor $\mathcal{B}(\Lambda^* \to pK^-)/\mathcal{B}(K^{*0} \to \pi^+K^-)$ added. In order to estimate the unknown ratio of branching fractions between $\Lambda_b \to \Lambda^*\gamma$ and $B^0 \to K^{*0}\gamma$ decays, a dedicated $\Lambda_b \to \Lambda^*\gamma$ selection has been designed and applied on the full 2011 data sample. This selection is based on the $B^0 \to K^{*0}\gamma$ selection described in section Sec. 5.3, replacing the pion identification requirement with tight proton identification criteria, $\mathrm{DLL}_{p\pi}(p) > 20$ and $\mathrm{DLL}_{pK}(p) > 2$, in order to reduce the cross-contamination from mis-identified $B^0 \to K^{*0}\gamma$ decays. In addition, the invariant mass of the pK^- system is required to be less than $2.5\,\mathrm{GeV}/c^2$ to cover a large range of the massive Λ^* resonances. As shown in Fig. 5.23, a clear signal of 527 ± 29 (stat.) $\Lambda_b \to \Lambda^*(pK^-)\gamma$ candidates are observed in the $1.0\,\mathrm{fb}^{-1}$ dataset.

The ratio of branching fractions between $\Lambda_b \to \Lambda^*\gamma$ and $B^0 \to K^{*0}\gamma$ decays

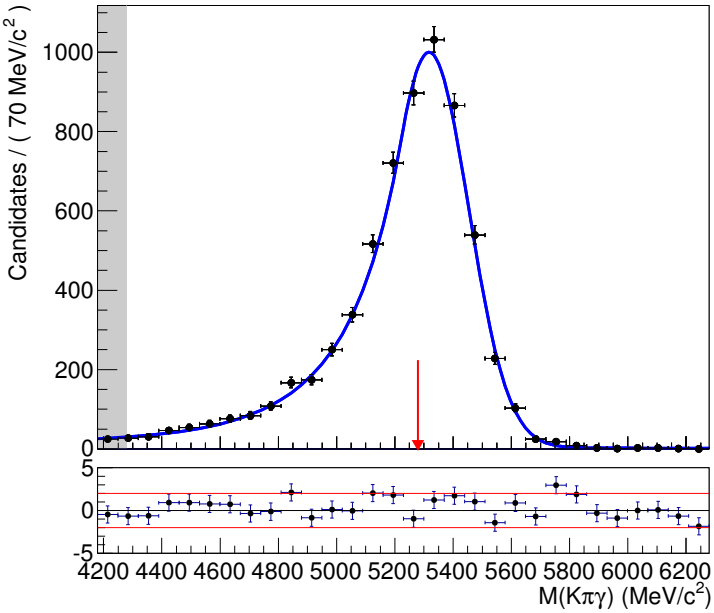

Figure 5.22 – Invariant-mass distribution of the K^+ π^- γ combinations, reconstructed in a sample of $\Lambda_b \to \Lambda^*(pK^-)\gamma$ simulated events. The mass shape is modelled with a Crystal-Ball function. The shaded region is outside the selection mass window, and the red arrow indicates the position of the signal peak. The Poisson χ^2 residuals [108] are shown below the fits with the ± 2 confidence-level interval delimited by solid red lines.

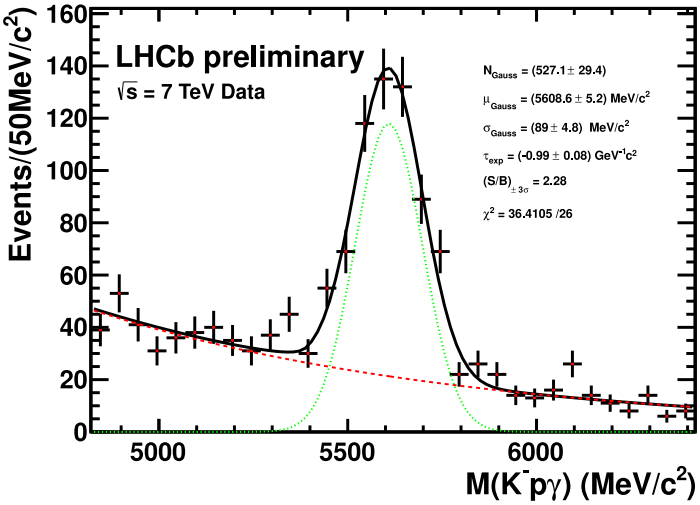

Figure 5.23 – Invariant-mass distribution for the $\Lambda_b \to \Lambda^*(pK^-)\gamma$ decay, reconstructed in the $1.0\,\text{fb}^{-1}$ of data collected by LHCb in 2011.

is estimated as

$$\frac{\mathcal{B}(\Lambda_b \to \Lambda^* \gamma)}{\mathcal{B}(B^0 \to K^{*0}\gamma)} \times \frac{\mathcal{B}(\Lambda^* \to pK)}{\mathcal{B}(K^{*0} \to \pi K)} \times \frac{f_{\Lambda_b}}{f_d} = \\ = \frac{\epsilon_{\rm MC}^{{\rm sel}(B^0 \to K^{*0}\gamma)}(B^0 \to K^{*0}\gamma)}{\epsilon_{\rm MC}^{{\rm sel}(\Lambda_b \to \Lambda^*\gamma)}(\Lambda_b \to \Lambda^*\gamma)} \times \frac{N(\Lambda_b \to \Lambda^*\gamma)}{N(B^0 \to K^{*0}\gamma)}\,, \tag{5.16}$$

where $N(X)$ is the selected data yield for the considered decay applying the corresponding selection. Combining Eq. 5.12 and Eq. 5.16, the relative contamination of $\Lambda_b \to \Lambda^*\gamma$ decays to $B^0 \to K^{*0}\gamma$ is reduced to

$$C_{\Lambda_b \to \Lambda^*\gamma} = \frac{\epsilon_{\rm MC}^{{\rm sel}(B^0 \to K^{*0}\gamma)}(\Lambda_b \to \Lambda^*\gamma)}{\epsilon_{\rm MC}^{{\rm sel}(\Lambda_b \to \Lambda^*\gamma)}(\Lambda_b \to \Lambda^*\gamma)} \times \frac{N(\Lambda_b \to \Lambda^*\gamma)}{N(B^0 \to K^{*0}\gamma)}\,, \tag{5.17}$$

where $N(B^0 \to K^{*0}\gamma)$ is evaluated from a fit to the data, neglecting the Λ_b contamination in a first approximation.

Samples of $\Lambda_b \to \Lambda(1520)\gamma$ and $\Lambda_b \to \Lambda(1670)\gamma$ simulated events give a similar relative contamination to $B^0 \to K^{*0}\gamma$, estimated as

$$C_{\Lambda_b \to \Lambda^*\gamma} = (0.027 \pm 0.004) \times r^p_{\rm PID}\,, \tag{5.18}$$

where $r^p_{\rm PID}$ is the relative rate of the proton to pion mis-identification defined as

$$r^p_{\rm PID} = \frac{\epsilon^{p\to\pi}_{\rm PID}}{\epsilon^{p\to p}_{\rm PID}}\,. \tag{5.19}$$

The $r^p_{\rm PID}$ value has been extracted from a calibration sample of $\Lambda(p\pi)$ reconstructed decays selected using kinematic criteria only, and found to be $r^p_{\rm PID} = (36 \pm 8)\%$. Finally, the $\Lambda_b \to \Lambda^*\gamma$ contamination to the $B^0 \to K^{*0}\gamma$ signal is estimated to be

$$C_{\Lambda_b \to \Lambda^*\gamma / B^0 \to K^{*0}\gamma} = (1.0 \pm 0.3)\%\,. \tag{5.20}$$

As a by-product, using $\mathcal{B}(B^0 \to K^{*0}\gamma) = (4.33 \pm 0.15) \times 10^{-5}$ [110] and $\mathcal{B}(K^{*0} \to K^+\pi^-) = (66.507 \pm 0.014) \times 10^{-2}$ [29], the branching fraction of the $\Lambda_b \to \Lambda^*(pK^-)\gamma$ with the invariant mass of the pK^- pair below 2.5 GeV/c^2 is measured as

$$\mathcal{B}(\Lambda_b \to \Lambda^*(pK^-)\gamma) \times \frac{f_{\Lambda_b}}{f_d} = (4.2 \pm 0.7) \times 10^{-6}\,, \tag{5.21}$$

where the uncertainty is statistical only.

Further contaminations arising from the double mis-identification of hadrons $pK^- \to K^+\pi^-$ are found to be negligible, due to the anti-proton PID requirement applied on the kaon candidate in the $B^0 \to K^{*0}\gamma$ selection (see Table 5.4).

5.5.5 Contamination from merged π^0

High-energy π^0 are likely to mimic a single photon when the electromagnetic showers of the photon pair cannot be resolved in the ECAL granularity. These *merged*–π^0 , are allowed by the kinematics of the decay when the transverse momentum of the π^0 exceeds 2 GeV/c. Charmless $B \to hh\pi^0$ decays with branching fractions of few 10^{-5} can produce a significant contamination to $B^0 \to K^{*0}\gamma$ decays. The contamination level and the shape of these charmless decays have been studied using simulated samples.

Contamination from $B^0 \to K^+\pi^-\pi^0$ decays

The $B^0 \to K^+\pi^-\pi^0$ decays have a branching fraction comparable to that of the signal, $\mathcal{B}(B^0 \to K^+\pi^-\pi^0) = (35.9^{+2.8}_{-2.4}) \times 10^{-6}$ [110]. These decays, produce a peaking background that accumulates around 5200 MeV/c^2. Its invariant-mass distribution, obtained from simulated samples, is modelled using a *CB* function, as displayed on Fig. 5.24.

The contribution where the $K\pi$ pair is resonant and forms a K^{*0} meson, $B^0 \to K^{*0}\pi^0$, is colour-suppressed for both the dominating $\bar{b} \to \bar{s}(\bar{d}d)$ penguin transition, and the sub-leading contribution from the Cabibbo-suppressed $\bar{b} \to \bar{u}(u\bar{s})$ tree transition. Based on simulated data, the relative contamination of $B^0 \to K^+\pi^-\pi^0$ decays to $B^0 \to K^{*0}\gamma$ is estimated to be

$$C_{B^0 \to K^\pm\pi^\mp\pi^0 / B^0 \to K^{*0}\gamma} = (0.5 \pm 0.1)\% \,, \tag{5.22}$$

where the uncertainty includes the contribution from the experimental resolution on the branching fractions and the limited statistics of the sample.

Contamination from $B_s^0 \to K^-\pi^+\pi^0$ decays

The $B_s^0 \to K^-\pi^+\pi^0$ decay has not been observed experimentally, but it could produce a peaked background accumulating around 5300 MeV/c^2, as shown in Fig. 5.25.

The overall $B_s^0 \to K^-\pi^+\pi^0$ branching fraction is expected to be at the same level as for the B^0 counterpart [113, 114], but the intermediate contributions have a very different pattern. As before, the most direct contamination with a resonant K^{*0} meson, $B_s^0 \to \overline{K}^{*0}\pi^0$, is colour-suppressed.

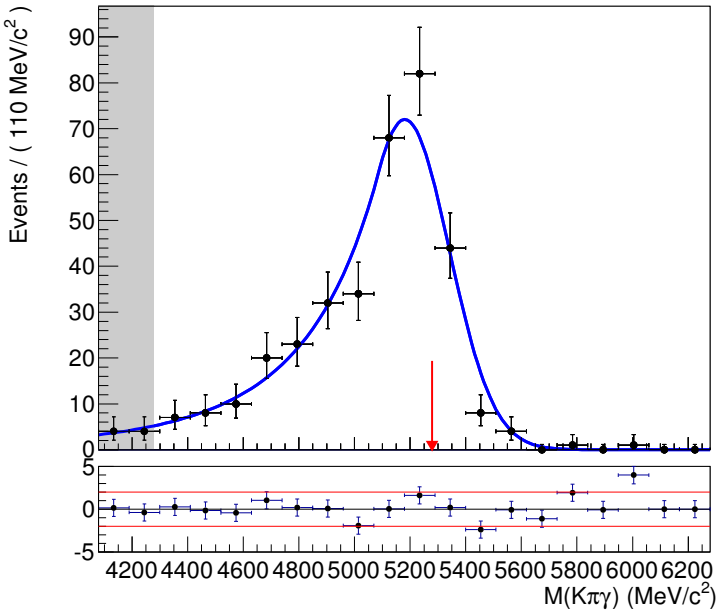

Figure 5.24 – Invariant-mass distribution of the $K^+\,\pi^-\,\gamma$ combinations reconstructed in 2×10^6 $B^0\to K^+\pi^-\pi^0$ simulated events. The mass distribution is fitted with a *CB* function. The shaded region is outside the selection mass window, and the red arrow indicates the position of the signal peak. The Poisson χ^2 residuals [108] are shown below the fits with the ±2 confidence-level interval delimited by solid red lines.

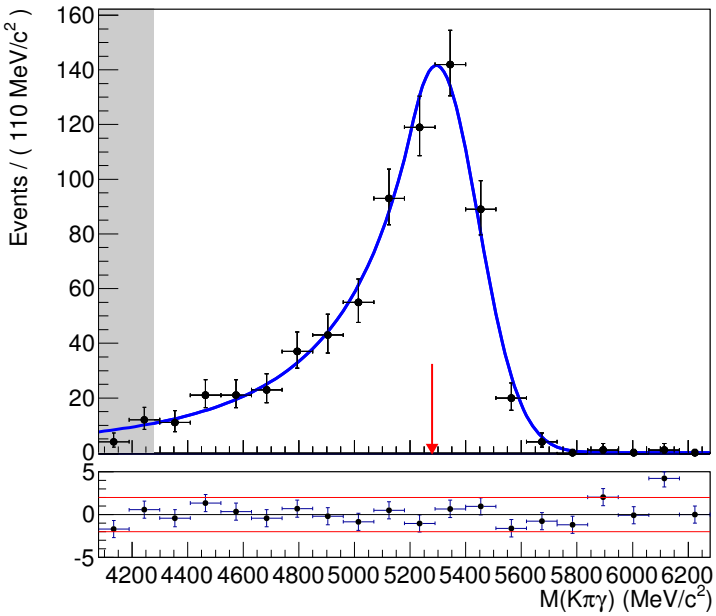

Figure 5.25 – Invariant-mass distribution of the $K^+\,\pi^-\,\gamma$ combinations reconstructed in 2×10^6 $B_s^0\to K^-\pi^+\pi^0$ simulated events. The mass distribution is fitted with a Crystal-Ball function. The shaded region is outside the selection mass window, and the red arrow indicates the position of the signal peak. The Poisson χ^2 residuals [108] are shown below the fits with the ±2 confidence-level interval delimited by solid red lines.

However, in the B_s^0 decay, the penguin contribution $\bar{b} \to \bar{d}(d\bar{d})$ is CKM-suppressed and the leading contribution is the Cabibbo-allowed tree transition $\bar{b} \to \bar{u}(u\bar{d})$ [113, 114]. The corresponding branching fraction is expected to be $\mathcal{B}(B_s^0 \to \overline{K}^{*0}\pi^0) = 7^{+5}_{-2} \times 10^{-8}$ [114].

The relative contamination of $B_s^0 \to K^-\pi^+\pi^0$ to $B^0 \to K^{*0}\gamma$ is conservatively taken as

$$C_{B_s^0 \to K^{*0}\pi^0 / B^0 \to K^{*0}\gamma} = (0.2 \pm 0.2)\% \,, \tag{5.23}$$

which is obtained by assuming the same branching fraction as for the B^0 decay, with a 100% uncertainty.

Other contamination from charmless decays with π^0

The contamination from $B^0 \to \pi^+\pi^-\pi^0$ and $B_s^0 \to K^+K^-\pi^0$ requires a π/K misidentification and is therefore suppressed. Both relative contributions are found to be of $\mathcal{O}(10^{-4})$ and are neglected.

5.6 Measurement of the *CP* asymmetry in the $B^0 \to K^{*0}\gamma$ decay

5.6.1 Extraction of the raw asymmetry

The raw *CP* asymmetry is extracted from an extended unbinned maximum likelihood fit, simultaneously to the $B^0 \to K^{*0}\gamma$ and $\overline{B}^0 \to \overline{K}^{*0}\,\gamma$ invariant-mass distributions. The peak position and width are kept the same for both B^0 and $\overline{B}^0$, as well as the mass-window threshold parameters. The relative amplitudes of the specific peaking backgrounds, $\Lambda_b \to \Lambda^*\gamma$, $B_s^0 \to K^{*0}\,\gamma$ and $B_s^0 \to K^\pm\pi^\mp\pi^0$, are fixed to the same value for both B flavours. The possible *CP* asymmetry of those decays will be included in the systematic uncertainties. Combinatorial background and partially reconstructed decays are allowed to vary freely and independently.

Fig. 5.26 shows the result of the simultaneous fit. The total signal yield extracted from the fit is measured to be $N(\overline{B}^0 \to \overline{K}^{*0}\gamma) + N(B^0 \to K^{*0}\gamma) = 5300 \pm 100$. The *CP* asymmetry is

$$A_{\mathrm{RAW}} = \frac{N(\overline{B}^0) - N(B^0)}{N(\overline{B}^0) + N(B^0)} = (0.3 \pm 1.7\,(\mathrm{stat.}))\% \,, \tag{5.24}$$

where the quoted uncertainty is statistical only. The yields of the combinatorial background across the entire mass window are compatible within statistical uncertainty. The number of combinatorial background candidates

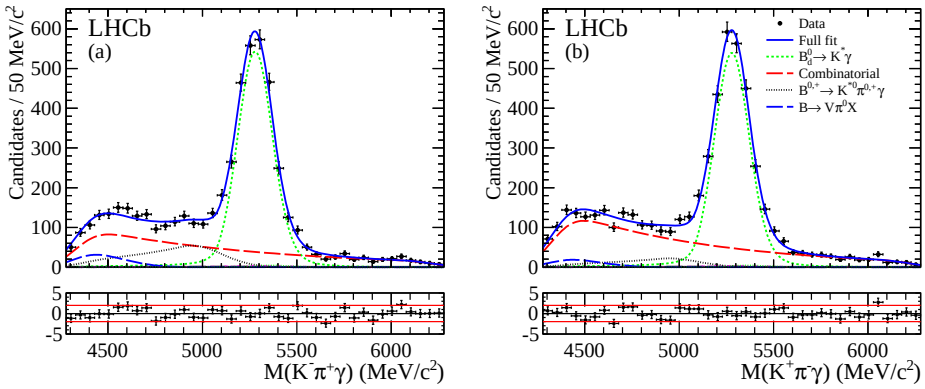

Figure 5.26 – Invariant-mass distributions of the $\overline{B}^0 \to \overline{K}^{*0}\ \gamma$ (left) and $B^0 \to K^{*0}\gamma$ (right) decay candidates. The black points represent the data and the fit result is represented as a solid blue line. The different background components are also shown. The Poisson χ^2 residuals [108] are shown below the fits with the ± 2 confidence-level interval delimited by solid red lines.

is 2070±414 and 1552±422 in the full mass range for the $B^0 \to K^{*0}\gamma$ and $\overline{B}^0 \to \overline{K}^{*0}\gamma$ decays, respectively. The contribution from the partially reconstructed decay $B \to K^{*0}\pi\gamma$ to $B^0 \to K^{*0}\gamma$ and $\overline{B}^0 \to \overline{K}^{*0}\gamma$ is $(10 \pm 6)\%$ and $(24 \pm 7)\%$ of the signal yield, respectively. Furthermore, the charmless partially reconstructed decays $B \to K^{*0}\pi^0$X contribute with $(7 \pm 8)\%$ and $(9 \pm 8)\%$ of the signal yield to the $B^0 \to K^{*0}\gamma$ and $\overline{B}^0 \to \overline{K}^{*0}\gamma$ decays, respectively. The last decays give contributions that are mainly located outside the signal invariant-mass region, as depicted in Fig. 5.26. The parameters obtained from the simultaneous fit are listed in Table 5.7.

5.6.2 Validation of the fit

The goodness of the fit is quantified by the p-value of the χ^2 test statistic [115], and it is defined as

$$p = \int_{\text{nDoF}}^{\infty} \chi^2(\text{nDoF}')\, d\text{nDoF}', \tag{5.25}$$

where nDoF is the number of degrees of freedom, and the χ^2 is defined as

$$\chi^2 = \sum_{c=1}^{n_c} \frac{(o_c - e_c)^2}{e_c}, \tag{5.26}$$

Fit parameter	Value
N_{exp,B^0}	2070 ± 414
τ_{B^0} $(\text{GeV}^{-1}\text{c}^2)$	-1.17 ± 0.21
$B \to K^{*0}\gamma\pi$	$(10 \pm 6)\%$
$B \to K^{*0}\pi^0\text{X}$	$(7 \pm 8)\%$
$N_{\text{exp},\bar{B}^0}$	1552 ± 422
$\tau_{\bar{B}^0}$ $(\text{GeV}^{-1}\text{c}^2)$	-0.98 ± 0.30
$B \to \bar{K}^{*0}\gamma\pi$	$(24 \pm 7)\%$
$B \to \bar{K}^{*0}\pi^0\text{X}$	$(9 \pm 8)\%$
$N_{\bar{B}^0} + N_{B^0}$	5300 ± 100
A_{RAW}	$(0.3 \pm 1.7)\%$
μ_{B^0} (MeV/c^2)	5279.1 ± 1.8
σ_{B^0} (MeV/c^2)	92.6 ± 1.6
t_L (MeV/c^2)	4351 ± 21
t_U (MeV/c^2)	6247 ± 27
σ_d (MeV/c^2)	142 ± 31

Table 5.7 – Fit parameters for $B^0 \to K^{*0}\gamma$ background (first section), $\overline{B}^0 \to \overline{K}^{*0}\,\gamma$ background (second section) and common parameters, including the total signal yield, the *CP* asymmetry, the signal shape parameters and the threshold function discussed in Sec. 5.4.1 (third section).

where n_c is the number of bins and o_c (e_c) are the number of observed (expected) events in the c^{th} bin. The χ^2 residuals are represented in the bottom plot of Fig. 5.26, and their sum is χ^2 =84.63. The number of degrees of freedom is computed as nDoF $= n_c - n_p - 1 - 1 = 63$, where $n_c = 80$ is the total number of bins, $n_p = 15$ is the number of free parameters in the fit, and one is subtracted to account for the normalisation of each histogram. This yields a p-value of $p = 0.036$ which shows the agreement between the data and the fitted p.d.f. Notice that there are six entries in the bin containing the minimum number of candidates.

In order to test the validity of the fitting procedure, toy experiments have been performed. Pseudo-data is generated following the fitted distribution, with the value of the parameters extracted from the fit to data and varied within their uncertainty. A good estimator of the stability of the fit is the

pull distribution [116], defined as

$$\mathcal{P}_x = \frac{x_{\rm Toy} - x_{\rm Fit}}{\sigma_{\rm x_{Toy}}}\,, \tag{5.27}$$

where x is the variable under study, $x_{\rm Toy}$ and $\sigma_{\rm x_{Toy}}$ are the central value and its uncertainty for a given toy experiment, and $x_{\rm Fit}$ is the value that has been obtained from the real data fit. As the toy experiments have been generated using as central value the value from the data fit, the pull distribution should follow a Gaussian distribution centred at $\mu = 0$ with mean $\sigma = 1$. If the fit is sensitive to the particular fluctuations of data, a bias in the central value of the pull distribution will be observed, while if the uncertainties are wrongly estimated, the width will differ from unit.

For each of the 3000 toy experiments performed, the $A_{\rm RAW}$ value has been extracted and its pull distribution has been calculated. The mean value and width are $\mu = -0.040 \pm 0.018$ and $\sigma = 0.998 \pm 0.014$, respectively, hence no significant bias is observed. The pull distribution is displayed on Fig. 5.27.

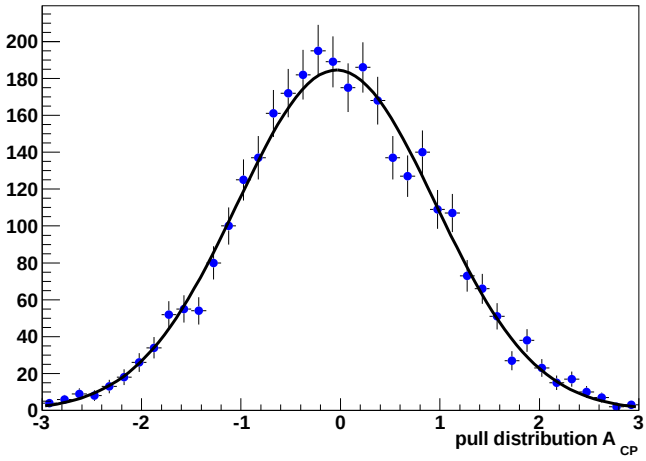

Figure 5.27 – Pull distribution of the $A_{\rm RAW}$ parameter obtained with 3×10^3 toy Monte Carlo experiments. A Gaussian fit is superimposed to the toy experiments.

5.6.3 Systematic uncertainty

The systematic uncertainty induced by the background modelling has been extracted by varying in the fit the fixed parameters of each specific background within their uncertainties. In addition, the *CP* asymmetry of those

backgrounds has been varied in the ±100% range, except for the $B^0 \to K\pi\pi^0$ decay, for which the experimental world average, $A_{CP}(B_d \to K^{*0}\pi^0) = (-15 \pm 12)\%$ [110], has been used. A_{RAW} has been extracted for 10000 fits with the variation of the raw asymmetry displayed on Fig. 5.28. It follows a Gaussian distribution centred on −0.2% with a standard deviation of 0.7%, therefore, a correction of $\Delta A_{\mathrm{bkg}} = (-0.2 \pm 0.7)\%$ is applied to the raw value of the asymmetry.

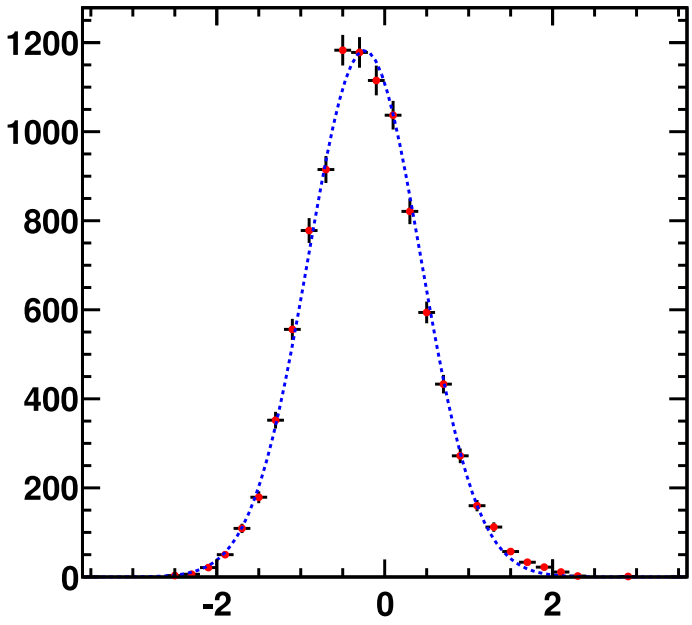

Figure 5.28 – Variation of the raw asymmetry (%) when varying the fixed parameters of the background model within their uncertainty. A Gaussian fit is superimposed to the 10000 fits.

Using the same procedure, a negligible systematic uncertainty induced by the signal modelling has been obtained. The presence of double misidentification, $K^-\pi^+ \to K^+\pi^-$, that would induce a dilution of the measured raw asymmetry has been evaluated using simulated events and also found to be negligible.

Including the systematics associated to the background model, the raw asymmetry is

$$A_{\mathrm{RAW}} = (0.1 \pm 1.7\,(\mathrm{stat.}) \pm 0.7\,(\mathrm{syst.}))\%\,. \tag{5.28}$$

5.6.4 Detection and production asymmetry

To extract the physical *CP* asymmetry, the raw asymmetry needs to be corrected from the effects induced by the detector geometry, the event reconstruction and the strong interaction of the final state particles with the detector material, as well as the relative initial abundances of B^0 and $\overline{B}^0$.

The physical *CP* asymmetry is related to the raw asymmetry by

$$A_{CP}(B^0 \to K^{*0}\gamma) = A_{\rm RAW}(B^0 \to K^{*0}\gamma) - A_{\rm D}(K\pi) - \kappa A_{\rm P}(B^0)\,, \qquad (5.29)$$

where $A_{\rm D}(K\pi)$ and $A_{\rm P}(B^0)$ represent the detection and production asymmetry, respectively. The κ factor is a dilution factor due to the neutral B meson oscillation.

Detection asymmetries

The detection asymmetry is due to the different interaction rate of kaons and antikaons with the detector material, due to the presence of the s or $\overline{s}$ quark. The differences induced by the pion can be neglected at first order as the $u-\overline{u}$ and $d-\overline{d}$ interactions are approximately the same. The detection asymmetry can be defined in terms of the detection efficiencies of the charged-conjugate final states by

$$A_{\rm D}(K\pi) = \frac{\epsilon(K^-\pi^+) - \epsilon(K^+\pi^-)}{\epsilon(K^-\pi^+) + \epsilon(K^+\pi^-)}\,. \qquad (5.30)$$

The detection asymmetry can be expressed as [117]

$$A_{\rm D}(K\pi) = A_{\rm I}(K\pi) + \alpha(K\pi)A_{\rm R}(K\pi)\,, \qquad (5.31)$$

where $A_{\rm I}(K\pi)$ is the asymmetry due to the different strong interaction cross-section with the detector material of $K^+\pi^-/K^-\pi^+$ final state particles, and $A_{\rm R}(K\pi)$ is the asymmetry arising from the presence of a left-right detector asymmetry and a possible reconstruction asymmetry. The factor $\alpha(K\pi)$ accounts for different signal yields in the data sets with opposite magnet polarities, due to the different values of the corresponding integrated luminosities and to the changing trigger conditions in the course of the run. It is extracted from the signal yield of $B^0 \to K\ \pi$ as

$$\alpha(K\pi) = \frac{(N^{\rm up} - N^{\rm down})}{(N^{\rm up} + N^{\rm down})} = -0.202 \pm 0.011\,. \qquad (5.32)$$

The $A_{\rm I}(K\pi)$ and $A_{\rm R}(K\pi)$ contributions present a different behaviour when reverting the magnetic field polarity form up to down. $A_{\rm I}(K\pi)$ is not

expected to change value when changing the magnet polarity, as the difference in the interaction length of positive and negative particles for opposite polarities is small. On the other hand, the sign of $A_{\rm R}(K\pi)$ changes when reverting the magnet polarity (see [117] for a more detailed explanation)

The related instrumental asymmetries have been studied using control samples of $D^{*+} \to D^0(K^-\pi^+)\pi^+$, $D^{*+} \to D^0(K^-K^+)\pi^+$ and $D^0(K^-\pi^+)$ decays, with their charge-conjugate modes. The combination of the integrated raw asymmetries of all these decay modes is necessary to disentangle the various contributions to the raw asymmetries of each mode —notably including the $K\pi$ instrumental asymmetry as well as that of the pion from the D^{*+} decay— and the production asymmetries of the D^{*+} and D^0 mesons. Thus, $A_{\rm I}(K\pi)$ and $A_{\rm R}(K\pi)$ have been measured to be

$$\begin{aligned} A_{\rm I}(K\pi) &= (-1.0 \pm 0.2) \times 10^{-2} \\ A_{\rm R}(K\pi) &= (-1.8 \pm 0.2) \times 10^{-3}\,, \end{aligned} \tag{5.33}$$

where the uncertainties come from the limited statistics on the control samples. Combining these results into Eq. 5.31, it has been found that the detection asymmetry for $K\pi$ pairs is dominated by the $A_{\rm I}(K\pi)$ term being

$$A_{\rm D}(K\pi) = (-1.0 \pm 0.2)\%\,. \tag{5.34}$$

Within the statistics available, no dependence of the detection asymmetry on the kinematics of the $(K\pi)$ system has been found.

Another instrumental bias might be induced by the magnetic field that spreads out the opposite charge in different regions of the detector. Any non-uniformity of the instrumental performance could introduce a bias in the asymmetry measurement. This possible bias is experimentally reduced by regularly flipping the magnetic polarity during the data taking. The raw asymmetry and the number of signal candidates obtained on the data samples corresponding to each of the magnet polarities is given in Table 5.8.

The values at different magnet polarities are compatible within statistical uncertainty and with the luminosity-weighted average, which is in agreement with the raw asymmetry measured on the full data sample. As the luminosity is slightly unbalanced between the two polarities, a residual bias could remain. This possible bias can be extracted from the polarity-split asymmetries as

$$\Delta A_{\rm M} = \frac{\mathcal{L}^{\rm up} - \mathcal{L}^{\rm down}}{\mathcal{L}^{\rm up} + \mathcal{L}^{\rm down}} \times \frac{A^{\rm down} - A^{\rm up}}{2}\,, \tag{5.35}$$

where $\mathcal{L}_{\rm up}$ and $\mathcal{L}_{\rm down}$ are the amount of luminosity collected in the up and down magnet configuration, respectively. For the entire 2011 data taking

	Magnet Up	Magnet Down	Luminosity-weighted average
$\int \mathcal{L} dt$ (pb^{-1})	432 ± 15	588 ± 21	1020 ± 36
$A_{\rm RAW}$ (%)	1.3 ± 2.6	-0.4 ± 2.2	0.4 ± 1.7
Signal candidates	2189 ± 65	3103 ± 71	5300 ± 100

Table 5.8 – *CP* asymmetry measured for each magnet polarity. The last column gives the luminosity-weighted average.

period the asymmetry in the luminosity collected is $(15 \pm 1)\%$, and a residual bias consistent with zero is obtained

$$\Delta A_{\rm M} = (+0.1 \pm 0.2)\% \,, \tag{5.36}$$

where the uncertainty comes from the limited signal sample.

B^0 meson production asymmetry

Because of the d quark content of the protons, B^0 and $\overline{B}^0$ mesons are not produced exactly with the same rate in proton-proton collisions. The B production asymmetry, $A_{\rm P}(B^0)$, is given in terms of the different production rates as

$$A_{\rm P}(B^0) = \frac{R(\overline{B}^0) - R(B^0)}{R(\overline{B}^0) + R(B^0)} \,. \tag{5.37}$$

It has been measured using a large sample of $B^0 \to J/\psi\, K^{*0}$ decays [117] —where the possible presence of *CP* violation in $b \to c\bar{c}s$ transitions has been neglected as in the SM is predicted to be at the 10^{-3} level— to be

$$A_{\rm P}(B^0) = (1.0 \pm 1.3)\% \,, \tag{5.38}$$

where the uncertainty comes from the limited amount of statistics present in the sample. No dependence on the kinematic properties of the $B^0 - \overline{B}^0$ system has been found within the statistics available. Its contribution to the measured *CP* asymmetry is diluted due to the neutral B^0 meson oscillation. The dilution factor κ is defined as

$$\kappa = \frac{\int \cos(\Delta m_d t) e^{-\Gamma_d t} \epsilon(t) dt}{\int \cosh(\frac{\Delta\Gamma_d t}{2}) e^{-\Gamma_d t} \epsilon(t) dt} \,, \tag{5.39}$$

where Δm_d and $\Delta\Gamma_d$ are the mass difference and the decay width difference between the mass eigenstates of the $B^0 - \overline{B}^0$ system, Γ_d is the average of their decay widths and $\epsilon(t)$ is the decay-time acceptance function of the signal selection. The decay-time acceptance function has been extracted from data by means of the sPlot technique and it has been fit with the PDF

$$f(t) = Ae^{-\Gamma_d t} \otimes G(0,\sigma) \times \frac{(at)^c}{1+(at)^c}\,, \tag{5.40}$$

where A is a normalization factor, Γ_d is the B^0 decay width, G is a Gaussian resolution function centred at 0 and with $\sigma = 40\,\text{fs}$, the expected decay-time resolution, and a and c a free parameters governing the decay-time acceptance of the selection. The fitted distribution of the decay-time acceptance is shown in Fig. 5.29.

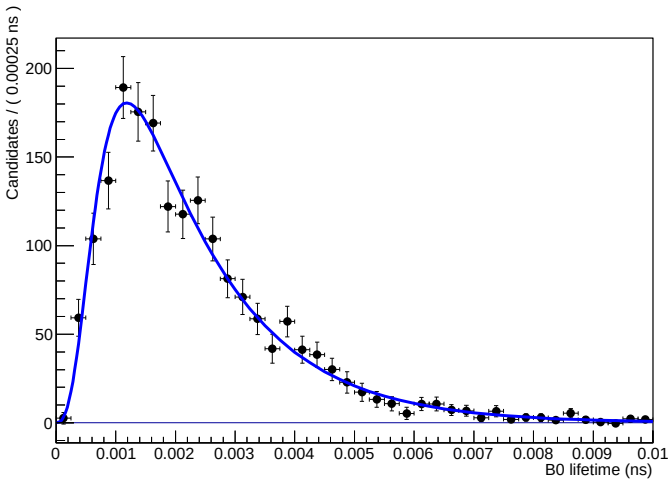

Figure 5.29 – Fit of the decay time acceptance function of signal events, extracted with sPlot technique.

The values of the a and c parameters as well as the κ factor value are given in Table 5.9.

In the calculation of κ, it has been assumed that $\Delta\Gamma_d = 0$, and the central values of the current world averages for Γ_d and Δm_d have been used [29]. The value of the parameters obtained on data is fully consistent with the simulation expectation. Any variation of the decay-time resolution σ between 20 fs and 200 fs is found to not affect significantly the result.

The entire list of corrections is summarised in Table 5.10.

Parameter	value
a (ps^{-1})	1416 ± 109
c	3.71 ± 0.37
κ	0.411 ± 0.035

Table 5.9 – Parameters governing the decay time acceptance function for reconstructed $B^0 \to K^{*0}\gamma$ decays with the corresponding κ factor.

		correction(%)	uncertainty(%)
Background model	: ΔA_{bkg}	-0.2	± 0.7
Detection	: $-A_{\mathrm{D}}(K\pi)$	$+1.0$	± 0.2
Magnet polarity	: ΔA_M	$+0.1$	± 0.2
B^0 production	: $-\kappa A_{\mathrm{P}}(B^0)$	-0.4	± 0.5
Total		$+0.5$	± 0.9

Table 5.10 – Corrections to the raw asymmetry and their corresponding systematic uncertainties.

5.7 *CP* asymmetry results

Adding the above corrections to the raw asymmetry, the direct *CP* asymmetry in $B^0 \to K^{*0}\gamma$ decays using $1\,\mathrm{fb}^{-1}$ of pp collisions at a centre-of-mass energy of $\sqrt{s} = 7\,\mathrm{TeV}$ is measured as

$$A_{CP}(B^0 \to K^{*0}\gamma) = (0.8 \pm 1.7\,(\mathrm{stat.}) \pm 0.9\,(\mathrm{syst.}))\%\,. \tag{5.41}$$

in agreement with the SM expectation of $(-0.61 \pm 0.43)\%$ [90]. This is consistent with previous measurements [96,97,118], and it is the most precise result of the direct *CP* asymmetry in $B^0 \to K^{*0}\gamma$ decays to date.

6 Conclusions

This document has presented the calibration and alignment of the SPD detector as well as the measurement of the direct *CP* asymmetry in $B^0 \to K^{*0}\gamma$ decays using $1.0\,\text{fb}^{-1}$ of data collected with the LHCb detector at a centre-of-mass energy of $\sqrt{s} = 7\,\text{TeV}$.

The SPD detector has been commissioned using cosmic rays before the LHC start-up, and then with *pp* collisions. A precision in the calibration factor of 15% was obtained with cosmic rays, allowing, for example, to use the SPD detector as the trigger for the first LHC collisions. The final calibration with *pp* collisions provided a precision in the calibration factor of 1.5%.

The alignment of the SPD with respect to the tracking system has also been studied, finding a rotation around the z axis, clockwise in the C-side and counter-clockwise in the A-side. Besides, a vertical displacement of 10 mm has been observed.

The evolution of the efficiency with time has been measured, and an overall decrease of 0.3% — which is statistically significant— has been observed in a period of time of four months. As far as the alignment is concerned, the openings and closings of the detector during the shut-downs, have modified the original misalignment by $\sim 10\%$.

The direct *CP* asymmetry in the $B^0 \to K^{*0}\gamma$ decay has been measured using $1.0\,\text{fb}^{-1}$ of *pp* collisions taken with the LHCb detector at a centre-of-mass energy of $\sqrt{s} = 7\,\text{TeV}$. The result found is

$$A_{CP}(B^0 \to K^{*0}\gamma) = (0.8 \pm 1.7\,(\text{stat.}) \pm 0.9\,(\text{syst.}))\%\,, \tag{6.1}$$

which is in agreement with the SM expectation of $(-0.61 \pm 0.43)\%$ and improves by 20% the previous world best measurement. This measurement can be combined with the previous BaBar result, and by doing a fit to both

values the combination yields

$$A_{CP}^{\rm comb}(B^0 \to K^{*0}\gamma) = (-0.23 \pm 1.51)\%\,, \tag{6.2}$$

which is also in agreement with the SM prediction. This result constrains a large fraction of the parameter space for several beyond-the-SM scenarios. For instance, a small *CP* violation reduces the possibility of having large corrections to the chromo-magnetic penguin operator, and also reduces heavily the parameter-space available for large corrections to the electroweak penguin operator. On a model dependent approach, this result implies that large values for an extra *CP* violating phase coming from the squark mixing parameter $(\delta^d_{23})_{LR}$, are not allowed.

Another interesting result, obtained as a by-product of the main analysis, is the observation of the first radiative decay of Λ_b baryons into $\Lambda_b \to \Lambda^*\gamma$, where Λ^* is any resonant state above the pK threshold. A clear signal has been observed and a very preliminary branching fraction of this decay has been measured to be

$$\mathcal{B}(\Lambda_b \to \Lambda^*(pK^-)\gamma) = 4.2 \pm 0.7 \times 10^{-6}\,, \tag{6.3}$$

where the uncertainty is statistical only. The systematic uncertainty induced by the signal and background description, as well as by the selection of the signal still needs to be addressed for this channel.

During the 2012 data taking more than $2\,\text{fb}^{-1}$ at a centre-of-mass energy of $\sqrt{s} = 8\,\text{TeV}$, are expected. Including these data into the analysis of the *CP* asymmetry in $B^0 \to K^{*0}\gamma$ decays, will improve significantly the precision of the measurement. The increase in the energy of the collisions, is translated into a 15% increase in the $b\bar{b}$ production cross-section. However, the tighter trigger requirements cancel this increase, resulting in a negligible net increase of the expected number of signal candidates per fb^{-1}. The factor ~ 3 more statistics in the 2011+2012 data sample with respect to 2011, is expected to reduce the statistical uncertainty of the *CP* asymmetry to $\sim 1\%$. Furthermore, the systematic uncertainty can be reduced thanks to the efforts made in measuring the branching fractions and *CP* asymmetries in decay channels present as background contamination. Putting all these together, a measurement of the direct *CP* asymmetry in the $B^0 \to K^{*0}\gamma$ decays with a precision at the 1% level is expected when combining the data of 2011 and 2012.

Bibliography

[1] A. Sakharov, *Violation of CP invariance, C asymmetry, and baryon asymmetry of the Universe*, Pisma Zh. Eksp. Teor. Fiz. **5** (1967) 32. 1

[2] M. Kobayashi and T. Maskawa, *CP-violation in the renormalizable theory of weak interaction*, Progress of Theoretical Physics **49** (1973), no. 2 652. 1, 16

[3] M. Shaposhnikov, *Possible appearance of the baryon asymmetry of the Universe in an electroweak theory*, JETP Lett. **44** (1986) 465. 1

[4] J. Christenson, J. Cronin, V. Fitch, and R. Turlay, *Evidence for the 2π decay of the k_2^0 meson*, Phys. Rev. Lett. **13** (1964) 138. 1

[5] Belle collaboration, K. Abe *et al.*, *Observation of large CP violation in the neutral B meson system*, Phys. Rev. Lett. **87** (2001) 091802. 1

[6] BaBar collaboration, B. Aubert *et al.*, *Measurement of the $B^0 - \overline{B}^0$ oscillation frequency with inclusive dilepton events*, Phys. Rev. Lett. **88** (2002) 221803. 1

[7] M. Han and Y. Nambu, *Three triplet model with double SU(3) symmetry*, Phys. Rev. **139** (1965) B1006. 3, 4

[8] S. Glashow, *Partial symmetries of weak interactions*, Nucl. Phys. **22** (1961) 579. 3, 4

[9] S. Weinberg, *A model of leptons*, Phys. Rev. Lett. **19** (1967) 1264. 3, 4

[10] A. Salam, *Weak and electromagnetic interactions*, Conf. Proc. **C680519** (1968) 367. 3, 4

[11] C.-N. Yang and R. L. Mills, *Conservation of isotopic spin and isotopic gauge invariance*, Phys. Rev. **96** (1954) 191. 5

[12] F. Englert and R. Brout, *Broken symmetry and the mass of gauge vector mesons*, Phys. Rev. Lett. **13** (1964) 321. 6

[13] P. W. Higgs, *Broken symmetries, massless particles and gauge fields*, Phys. Lett. **12** (1964) 132. 6

[14] P. W. Higgs, *Broken symmetries and the masses of gauge bosons*, Phys. Rev. Lett. **13** (1964) 508. 6

[15] G. Guralnik, C. Hagen, and T. Kibble, *Global conservation laws and massless particles*, Phys. Rev. Lett. **13** (1964) 585. 6

[16] P. W. Higgs, *Spontaneous symmetry breakdown without massless bosons*, Phys. Rev. **145** (1966) 1156. 6

[17] T. Kibble, *Symmetry breaking in non-abelian gauge theories*, Phys. Rev. **155** (1967) 1554. 6

[18] ATLAS collaboration, G. Aad *et al.*, *The ATLAS Experiment at the CERN Large Hadron Collider*, JINST **3** (2008) S08003. 6, 21

[19] CMS collaboration, S. Chatrchyan *et al.*, *The CMS experiment at the CERN LHC*, JINST **3** (2008) S08004. 6, 21

[20] ATLAS collaboration, G. Aad *et al.*, *Observation of a new particle in the search for the Standard Model Higgs boson with the ATLAS detector at the LHC*, Phys. Lett. B (2012) , arXiv:1207.7214. 6

[21] CMS collaboration, S. Chatrchyan *et al.*, *Observation of a new boson at a mass of 125* GeV *with the CMS experiment at the LHC*, Phys. Lett. B (2012) , arXiv:1207.7235. 6

[22] R. Fleischer, *CP violation and the role of electroweak penguins in nonleptonic B decays*, Int. J. Mod. Phys. **A12** (1997) 2459, arXiv:hep-ph/9612446. 6

[23] S. Weinberg, *The quantum theory of fields. Vol. 2: Modern applications*, Cambridge University Press (1996). 7

[24] A. Pich, *Effective field theory: Course*, arXiv:hep-ph/9806303. 7

[25] K. G. Wilson, *Non-lagrangian models of current algebra*, Phys. Rev. **179** (1969) 1499. 7

[26] G. Buchalla, A. J. Buras, and M. E. Lautenbacher, *Weak decays beyond leading logarithms*, Rev. Mod. Phys. **68** (1996) 1125, arXiv:hep-ph/9512380. 8

[27] I. I. Bigi and A. Sanda, *CP violation*, Camb. Monogr. Part. Phys. Nucl. Phys. Cosmol. **9** (2000) 1. 11

[28] N. Cabibbo, *Unitary symmetry and leptonic decays*, Phys. Rev. Lett. **10** (1963) 531. 16

[29] Particle Data Group, J. Beringer *et al.*, *Review of particle physics*, Phys. Rev. **D86** (2012) 010001. 16, 51, 81, 95, 96, 101, 106, 118

[30] L. Wolfenstein, *Parametrization of the Kobayashi-Maskawa matrix*, Phys. Rev. Lett. **51** (1983) 1945. 16

[31] A. J. Buras and R. Fleischer, *Quark mixing, CP violation and rare decays after the top quark discovery*, Adv. Ser. Direct. High Energy Phys. **15** (1998) 65, arXiv:hep-ph/9704376. 17

[32] C. Dib, I. Dunietz, F. J. Gilman, and Y. Nir, *Standard model predictions for CP violation in B^0 meson decay*, Phys. Rev. **D41** (1990) 1522. 17

[33] LHCb collaboration, I. Bediaga *et al.*, *Implications of LHCb measurements and future prospects*, arXiv:1208.3355. 17

[34] L. Evans and P. Bryant, *LHC Machine*, JINST **3** (2008) S08001. 20

[35] ALICE collaboration, K. Aamodt *et al.*, *The ALICE experiment at the CERN LHC*, JINST **3** (2008) S08002. 21

[36] LHCb collaboration, A. Augusto Alves Jr *et al.*, *The LHCb Detector at the LHC*, JINST **3** (2008). 25

[37] G. Wilkinson and N. Zaitsev, *Choice of running luminosity for LHCb, and performance of pile-up tag*, LHCb-97-014. 26

[38] P. R. Barbosa-Marinho *et al.*, *LHCb VELO: technical design report*, Tech. Rep. CERN-LHCC-2001-011, CERN, 2001. 27

[39] LHCb collaboration, R. Antunes-Nobrega *et al.*, *LHCb reoptimized detector design and performance*, Tech. Rep. CERN/LHCC/2003-030, CERN, 2003. 27, 30, 36, 41, 64

[40] J. Gassner, M. Needham, and O. Steinkamp, *Layout and expected performance of the LHCb TT station*, Tech. Rep. LHCb-2003-140, CERN, 2003. 27

[41] S. Amato *et al.*, *LHCb magnet: technical design report*, Technical Design Report LHCb, CERN, Geneva, 2000. 27

[42] J. André *et al.*, *Status of the LHCb magnet system*, IEEE Trans. Appl. Supercond. **12** (2001) 366. 27

[43] J. André *et al.*, *Status of the LHCb dipole magnet*, IEEE Trans. Appl. Supercond. **14** (2004), no. 2 509. 27

[44] LHCb collaboration, P. R. Barbosa-Marinho *et al.*, *LHCb inner tracker: technical design report*, Tech. Rep. CERN-LHCC-2002-029, CERN, 2002. 27, 65

[45] P. R. Barbosa-Marinho *et al.*, *LHCb outer tracker: technical design report*, Tech. Rep. CERN-LHCC-2001-024, CERN, 2001. 27, 65

[46] M. G. Van Beuzekom, W. Vink, L. W. Wiggers, and M. Zupan, *Pile-up veto L0 trigger system for LHCb using large FPGA's*, . 27

[47] N. Brook *et al.*, *LHCb RICH1 engineering design review report*, Tech. Rep. LHCb-2004-121. CERN-LHCb-2004-121, CERN, Geneva, Oct, 2005. 30

[48] S. Amato *et al.*, *LHCb RICH: technical design report*, Technical Design Report LHCb, CERN, Geneva, 2000. 31

[49] M. Adinolfi *et al.*, *LHCb RICH2 engineering design review report*, Tech. Rep. LHCb-2002-009, CERN, Geneva, Mar, 2002. 31

[50] LHCb collaboration, S. Amato *et al.*, *LHCb calorimeters*, Tech. Rep. CERN/LHCC/2000-0036, CERN, 2000. 31

[51] S. Bota *et al.*, *Scintillator pad detector front end electronics design*, tech. rep., 2000. 32

[52] E. Aguiló-Chivite and L. Garrido-Beltran, *The SPD Physics Features within the LHCb Calorimetry system.*, PhD thesis, Barcelona Univ., Barcelona, 2004. 32

[53] R. Antunes-Nobrega *et al.*, *LHCb trigger system technical design report*, tech. rep., CERN, 2003. 33, 36

[54] LHCb collaboration, A. A. Alves Jr. *et al.*, *The LHCb detector at the LHC*, JINST **3** (2008) S08005. 33

[55] LHCb collaboration, *Roadmap for selected key measurements of LHCb*, arXiv:0912.4179. 33, 81

[56] M. Calvo and H. Ruiz, *Monitoring the relative instantaneous luminosity with detector multiplicities*, LHCb Public Note, 2009. 33

[57] S. Filippov *et al.*, *Experimental performance of SPD/PS detector prototypes*, Tech. Rep. LHCb-2000-031, CERN, Geneva, Oct, 2000. 33

[58] A. Arefev *et al.*, *Beam test results of the LHCb electromagnetic calorimeter*, Tech. Rep. LHCb-2007-149. CERN-LHCb-2007-149, CERN, Geneva, May, 2008. 33, 34

[59] LHCb collaboration, R. Dzhelyadin, *The LHCb hadron calorimeter*, Nucl. Instrum. Meth. **A494** (2002) 332. 34

[60] P. R. Barbosa-Marinho *et al.*, *LHCb muon system: technical design report*, Technical Design Report LHCb, CERN, Geneva, 2001. 35

[61] LHCb collaboration, *LHCb muon system: addendum to the technical design report*, tech. rep., Geneva, 2003. 35

[62] LHCb collaboration, *LHCb muon system: second addendum to the technical design report*, tech. rep., Geneva, 2005. 35

[63] P. R. Barbosa-Marinho *et al.*, *LHCb online system, data acquisition and experiment control: technical design report*, Technical Design Report LHCb, CERN, Geneva, 2001. 40

[64] N. Tatsuya, E. Aslanides, A. Smith, and W. Witzeling, *Addendum to the LHCb online system technical design report*, Tech. Rep. CERN-LHCC-2001-040-ADD-1. CERN-LHCC-2005-039, CERN, Geneva, Nov, 2005. 40

[65] R. Antunes-Nobrega *et al.*, *LHCb computing: technical design report*, Technical Design Report LHCb, CERN, Geneva, 2005. 41

[66] LHCb collaboration, R. Aaij *et al.*, *Measurement of the effective* $B^0_s \to K^+K^-$ *lifetime*, Phys. Lett. **B716** (2012) 393, arXiv:1207.5993. 43

[67] LHCb collaboration, R. Aaij *et al.*, *Measurement of b-hadron branching fractions for two-body decays into charmless charged hadrons*, arXiv:1206.2794. 43

[68] *https://lbtwiki.cern.ch/bin/view/VELO/VELOConferencePlots*, . 44

[69] *https://lbtwiki.cern.ch/bin/view/RICH/RichPIDPerformancePlots*, . 46

[70] D. Golubkov and V. Egorychev, *Electron particle identification with LHCb calorimeter system for 2011 data taking period*, Tech. Rep. LHCb-INT-2011-052. CERN-LHCb-INT-2011-052, CERN, Geneva, Dec, 2011. 46

[71] *https://lbtwiki.cern.ch/bin/view/CALO/LHCbCaloPropaganda*, . 46, 48

[72] O. Deschamps *et al.*, *Photon and neutral pion reconstruction*, Tech. Rep. LHCb-2003-091, CERN-LHCb-2003-091, 2003. 48, 85

[73] E. Polycarpo Macedo *et al.*, *Performance of the muon identification in LHCb with 2011 data*, Tech. Rep. LHCb-INT-2012-016. CERN-LHCb-INT-2012-016, CERN, Geneva, Jun, 2012. 48

[74] R. Aaij *et al.*, *Measurement of* Υ *production in pp collisions at* $\sqrt{s} =$ 7 TeV , Eur. Phys. J. C **72** (2012) 2025, arXiv:1202.6579. 49

[75] L. Landau, *On the energy loss of fast particles by ionization*, J. Phys. (USSR) **8** (1944) 201. 50

[76] M. Calvo, *Backsplash Effects on SPD and Flavour Tagging in LHCb*, PhD thesis, Barcelona Univ., 2006. 51

[77] S. Bota *et al.*, *Discriminator ASIC for the SPD VFE of the LHCb calorimeter*, Tech. Rep. LHCb-2004-042, CERN, Geneva, 2004. 53

[78] D. Gascon, *Microelectronic design of pulse discriminator circuits for the LHCb detector*, PhD thesis, Barcelona, 2008. 55, 56, 57

[79] E. Picatoste, *LHCb Preshower (PS) and Scintillating Pad Detector (SPD): Commissioning, calibration, and monitoring*, J. Phys. Conf. Ser. **160** (2009) 012046. 55

[80] S. Filippov, *Status of cosmic tests and schedule*, http://indico.cern.ch/conferencedisplay.py?confid=a06511, CERN, CERN, 2006. 55, 56

[81] E. Picatoste, *Characterization protocol and set-up development of Hamamatsu 64 channel PMTs for the Scintillator Pad Detector (SPD) of the LHCb Experiment.*, Master's thesis, Barcelona, 2010. 56

[82] M. Calvo *et al.*, *Time alignment of the SPD with cosmic rays and LHC injection events*, Tech. Rep. LHCb-PUB-2010-015, CERN-LHCb-PUB-2010-015, CERN, Geneva, 2010. 59

[83] *Orwell: The LHCb online calibration farm application*, . 59

[84] O. Deschamps, *Cosmics reconstruction tool & cosmic monitoring*, http://indico.cern.ch/conferencedisplay.py?confid=36254. 59

[85] J. Ahmis, *Time alignment of the electromagnetic and hadronic calorimeters, reconstruction of the $B \to D^- \rho(770)^+$, $B_s^0 \to D_s^- \rho(770)^+$ and $B_s^0 \to D_s^- K^{*+}(892)$ decay channels with the LHCb detector*, PhD thesis, Paris, 2009. 59

[86] R. Vazquez Gomez, *Commissioning of the scintillator pad detector of LHCb with cosmic rays and first LHC collisions*, J. Phys. Conf. Ser. **293** (2011) 012059. 63

[87] M. Calvo *et al.*, *Time alignment of the SPD with LHC proton-proton collisions*, Tech. Rep. LHCb-PUB-2011-005, CERN-LHCb-PUB-2011-005, CERN, Geneva, 2011. 63

[88] *https://twiki.cern.ch/twiki/bin/view/LHCb/LHCbOperations*, . 64

[89] S. Descotes-Genon, D. Ghosh, J. Matias, and M. Ramon, *Exploring new physics in the C_7-C_7' plane*, JHEP **06** (2011) 099, arXiv:1104.3342. 79

[90] Y. Y. Keum, M. Matsumori, and A. I. Sanda, *CP asymmetry, branching ratios and isospin breaking effects of $B^0 \to K^{*0}\gamma$ with perturbative QCD approach*, Phys. Rev. **D72** (2005) 014013, arXiv:hep-ph/0406055. 80, 119

[91] C. Dariescu and M.-A. Dariescu, *$B^0 \to K^{*0}\gamma$ decay within MSSM*, arXiv:0710.3819. 80

[92] M. Aoki, G.-C. Cho, and N. Oshimo, *Decay rate asymmetry in $B \to X(s)\gamma$ as a signature of supersymmetry*, Phys. Rev. **D60** (1999) 035004, arXiv:hep-ph/9811251. 80

[93] M. Aoki, G.-C. Cho, and N. Oshimo, *CP asymmetry for radiative B meson decay in the supersymmetric Standard Model*, Nucl. Phys. **B554** (1999) 50, arXiv:hep-ph/9903385. 80

[94] A. L. Kagan and M. Neubert, *Direct CP violation in $B \to X(s)\gamma$ decays as a signature of new physics*, Phys. Rev. **D58** (1998) 094012, arXiv:hep-ph/9803368. 80, 81

[95] CLEO collaboration, R. Ammar *et al.*, *Evidence for penguin-diagram decays: First observation of $B \to K^*(892)\gamma$*, Phys. Rev. Lett. **71** (1993) 674. 81

[96] CLEO collaboration, T. Coan *et al.*, *Study of exclusive radiative B meson decays*, Phys. Rev. Lett. **84** (2000) 5283, arXiv:hep-ex/9912057. 81, 82, 119

[97] BaBar collaboration, B. Aubert *et al.*, *Measurement of branching fractions and CP and isospin asymmetries in $B \to K^*(892)\gamma$ decays*, Phys. Rev. Lett. **103** (2009) 211802, arXiv:0906.2177. 81, 82, 119

[98] Belle collaboration, J. Wicht *et al.*, *Observation of $B_s^0 \to \phi\gamma$ and search for $B_s^0 \to \gamma\gamma$ decays at Belle*, Phys. Rev. Lett. **100** (2008) 121801, arXiv:0712.2659. 82

[99] A. Puig Navarro and R. Graciani Diaz, *First measurements of radiative B decays in LHCb*, PhD thesis, Barcelona Univ., 2012, Presented 09 Mar 2012. 81, 84

[100] F. Soomro, B. Cameron, and A. Golutvin, *Radiative decays of B mesons at LHCb*, PhD thesis, Imperial Coll., London, 2011, Presented 03 Jun 2011. 81

[101] LHCb collaboration, R. Aaij *et al.*, *Measurement of $\sigma(pp \to b\bar{b}X)$ at $\sqrt{s} = 7$ TeV in the forward region*, Phys. Lett. **B694** (2010) 209. 82

[102] L. Shchutska, A. Golutvin, and I. Belyaev, *Study of radiative penguin decays $B^0 \to K^{*0}\gamma$ and $B_s^0 \to \phi\gamma$ at LHCb*, Tech. Rep. LHCb-2007-030. CERN-LHCb-2007-030, CERN, Geneva, May, 2007. 85

[103] M. Calvo, *π^0/γ separation tool.*, Talk at the Radiative Decays Meeting on Nov. 17th, CERN, CERN, November, 2011. 85

[104] M. Calvo, *π^0/γ separation tool.*, Talk at the Calorimeter Objects Meeting on Feb. 10th, CERN, CERN, February, 2011. 85

[105] A. Puig, D. Savrina, R. Graciani, and I. Belyaev, *Kali: The framework for fine calibration of LHCb Electromagnetic Calorimeter*, Tech. Rep. LHCB-PROC-2011-027, CERN-LHCb-PROC-2011-027, CERN, Geneva, May, 2011. 95

[106] G. Breit and E. Wigner, *Capture of slow neutrons*, Phys. Rev. **49** (1936) 519. 95

[107] HERA-B collaboration, I. Abt *et al.*, K^{*0} *and* ϕ *meson production in proton-nucleus interactions at* $\sqrt{s}$ *=41.6* GeV, Eur. Phys. J. **C50** (2007) 315, arXiv:hep-ex/0606049. 95

[108] S. Baker and R. D. Cousins, *Clarification of the use of chi-square and likelihood functions in fits to histograms*, Nucl. Instrum. Meth. **A221** (1984) 437. 96, 98, 100, 101, 103, 105, 108, 109, 111

[109] P. Ball, G. W. Jones, and R. Zwicky, $B \to V\gamma$ *beyond QCD factorisation*, Phys. Rev. **D75** (2007) 054004, arXiv:hep-ph/0612081. 99, 102

[110] Heavy Flavor Averaging Group, D. Asner *et al.*, *Averages of b-hadron, c-hadron, and* τ*-lepton Properties*, arXiv:1010.1589. 99, 102, 106, 107, 114

[111] LHCb collaboration, R. Aaij *et al.*, *Measurement of b hadron production fractions in 7 TeV ppcollisions*, Phys. Rev. **D85** (2012) 032008, arXiv:1111.2357. 98

[112] LHCb collaboration, R. Aaij *et al.*, *Measurement of b-hadron masses*, Phys. Lett. **B708** (2012) 241, arXiv:1112.4896. 102

[113] M. Beneke and M. Neuber, *QCD factorization for B→PP and B→PV decays*, arXiv:0308039. 107, 110

[114] A. Ali and G. Kramer, *Charmless non-leptonic* B_s *decays to PP, PV and VV final states in the pQCD approach*, arXiv:0703162v2. 107, 110

[115] M. Williams, *How good are your fits? Unbinned multivariate goodness-of-fit tests in high energy physics*, JINST **5** (2010) P09004, arXiv:1006.3019. 111

[116] L. Demortier and L. Lyons, *Everything you always wanted to know about pulls*, Tech. Rep. CDF/ANAL/PUBLIC/5776, CDF, 2002. 113

[117] R. Aaij *et al.*, *First evidence of direct CP violation in charmless two-body decays of B_s^0 mesons*, Phys. Rev. Lett. **108** (2012) 201601. 8 p. 115, 116, 117

[118] Belle collaboration, M. Nakao *et al.*, *Measurement of the $B \to K^*\gamma$ branching fractions and asymmetries*, Phys. Rev. **D69** (2004) 112001, arXiv:hep-ex/0402042. 119